RECEIVED
LAWRENCE
RADIATION LABORATORY

LIBRARY AND
DOCUMENTS SECTION

LBL-432
c.1

BEHAVIOR OF INELASTIC ELECTRONS

Teh Yu Tan

(Ph. D. Thesis)

January 1972

AEC Contract No. W-7405-eng-48

For Reference

Not to be taken from this room

LBL-432
c.1

DISCLAIMER

This document was prepared as an account of work sponsored by the United States Government. While this document is believed to contain correct information, neither the United States Government nor any agency thereof, nor the Regents of the University of California, nor any of their employees, makes any warranty, express or implied, or assumes any legal responsibility for the accuracy, completeness, or usefulness of any information, apparatus, product, or process disclosed, or represents that its use would not infringe privately owned rights. Reference herein to any specific commercial product, process, or service by its trade name, trademark, manufacturer, or otherwise, does not necessarily constitute or imply its endorsement, recommendation, or favoring by the United States Government or any agency thereof, or the Regents of the University of California. The views and opinions of authors expressed herein do not necessarily state or reflect those of the United States Government or any agency thereof or the Regents of the University of California.

0 0 0 0 3 7 0 0 0 2 8

Table of Contents

Abstract v

I. Introduction 1

II. A Theory of Kikuchi Patterns 4

A. Origin of the Kikuchi Pattern 4

B. Some Intricacies in the Kikuchi Pattern 8

C. A Review of the Existing Theories 10

D. Formulation of the Theory 13

E. Special Cases of the Kikuchi Pattern 33

1. Asymmetric One-beam Case -- Formation of the Kikuchi Line Pair 35

2. Symmetrical One-beam Case -- Formation and Behavior of Kikuchi Bands 37

3. Dynamical Two-beam Case -- Kikuchi Line Contrast Reversal and Spacing Variations 44

4. A Many-beam Problem 54

F. Images Due to Kikuchi Electrons and Other Inelastic Electrons 64

III. An Energy Analyzing Microscope 69

A. Introduction 69

B. Energy Analyzing Device -- The Mollenstedt Lens System . 71

C. Instrumentation 84

D. Operations 90

E. Possible Applications 92

IV. Summary and Discussion 99

Appendix: Fundamentals of the Dynamical Theory 107

A.1. Solution of the Many-beam Problem -- The Dispersion Matrix 107

A.2. Methods for Calculating the Dispersion Matrix . . 114

A.2.1. Method of Series Expansion 114

A.2.2. Method of Laplace Transforms 115

A.2.3. Method of Eigen-Solutions 119

A.2.4. Comparison of the Methods for Calculating the Dispersion Matrix 123

A.3. The Two-beam Theory 124

A.4. Dynamical Multiple Rescattering Process of Electron Diffractions -- An Interpretation from the Dispersion Matrix 134

A.5. Image Problems 136

Acknowledgement 151

References 152

BEHAVIOR OF INELASTIC ELECTRONS

Teh Yu Tan

Inorganic Materials Research Division, Lawrence Berkeley Laboratory and
Department of Materials Science and Engineering, College of Engineering;
University of California, Berkeley, California

ABSTRACT

This study is an investigation into certain aspects of the behavior of electrons after they become inelastic in a crystal. Except for brief discussions in places where circumstances require, it is not our intention to treat the various inelastic scattering mechanisms.

Inelastic electrons carry information such as image and characteristic loss spectrum of the specimen. In a diffraction pattern, they also form line and band intensity distributions known as Kikuchi patterns. A theory, which is applicable to calculations of both Kikuchi profiles and images formed by inelastic electrons, is formulated in terms of Bloch waves for which absorptions of both elastic and inelastic electrons are considered. Analytical solutions of the problem of Kikuchi intensity distributions for a four-beam case (two elastic and two inelastic beams) is obtained. It is shown that the following aspects of the behavior of the Kikuchi pattern are explained: (1) the formation of the Kikuchi line pair, (2) the formation of the Kikuchi band and its changes in intensity from excess to deficient, (3) the Kikuchi line contrast reversal, and (4) the variations of the Kikuchi line spacing with specimen thickness. Consideration of a systematic many-beam case for a thick crystal shows that for this case the Kikuchi pattern may be simply calculated from sums of rocking curve intensities.

The design and operational schematics of an energy analyzing microscope constructed at Berkeley is given in the second part of this thesis. It is thought that the applicability of this technique to microanalysis of local chemical constitutions of a crystal specimen by analyzing variations in plasmon loss spectrum is limited to Al basis alloys. This is so, because other materials do not possess a well defined sharp plasmon loss spectrum. However, experiments could be performed by applying this technique to measurements of other characteristic losses of the crystal, such as the energy band gap of a semiconductor.

A review of the dynamical theory of (elastic) electron diffraction in crystals, which forms the necessary background knowledge of this study, is given in the appendix. Since many similar or equivalent developments can be found in most texts and literatures on the subject, mathematical details are avoided when possible. Solutions of the many beam and image problems are formulated in terms of the dispersion matrix. Methods for calculating this matrix are given. The dispersion matrix is of physical importance because it reveals the multiple scattering nature of the Bloch waves formed in the crystal.

I. INTRODUCTION

During the course of a diffraction experiment in the electron microscope, a certain fraction of the high energy electrons will suffer from inelastic scatterings, thereby losing a small amount of energy. These electrons are called inelastic electrons. Inelastic scattering of electrons may take place by excitations of a number of elementary particle-waves in the crystal, e.g., a phonon, a plasmon, or the ionization of an inner shell electron. It is not the purpose of this study to investigate the various kinds of inelastic scattering mechanisms, but rather, the behavior of the electrons after they become inelastic.

Just like the elastic electrons, the inelastic electrons will also be Bragg reflected and form Bloch waves which are subject to further inelastic scatterings in the crystal. Before impinging upon the crystal, elastic electron beams can be manipulated to behave much as a plane wave and are only limited by the performance of the microscope. Inelastic electrons are, however, generated inside the crystal with a large angular spread. Elastic beams are allowed along definite directions and hence form spot patterns, on the other hand, the large angular spread of inelastic electrons allows the formation of continuous intensity variations guided by pairs of cones, which, when intersected by the recording plane, approximate to line patterns: the Kikuchi pattern. Through the depth of a thin specimen, elastic electrons may be regarded as fully coherent. Inelastic electrons generated at a definite depth of the crystal, however, lose coherency with elastic electrons as well as with other inelastic electrons of the same energy state which were not generated within the distance of a coherence length for the inelastic electrons.

Depending upon the inelastic scattering mechanism, the coherence length of inelastic electrons may range from a few angstroms (due to excitation of a phonon) to a few hundred angstroms (due to excitation of a plasmon). Both elastic and inelastic electrons form images. However, images produced by the noncoherent inelastic electrons may be sufficiently different from that produced by elastic electrons that cause obscuring of images to occur. The desirability of the removal of images produced by inelastic electrons leads to the construction of energy selecting microscopes. Nevertheless, inelastic electrons should not be simply regarded as a total nuisance, because they carry information in the form of an energy loss spectrum which is characteristic of the material. When properly displayed, information concerning the electronic structures of the crystal may be obtained from these energy loss spectra. To this end, energy analyzing microscopes can be built. The schematics of the design, fabrication, and possible applications of such a microscope constructed at Berkeley will be discussed in the second part of this thesis.

Beside the various experimental techniques for treating inelastic electrons, it is also desirable that their behavior be studied and understood theoretically. As should be expected, there are many such theories around. However, to varying degrees of approximations, these theories are all concerned with certain types of particular inelastic scattering mechanisms with the result that they are in general too complicated to use. The mathematical complexity of these theories also necessitates ignoring the absorptions of both elastic and inelastic electrons. It will be made clear in Chapter II that this ignorance is a rather drastic mistake. With these facts in mind, a theory, which is applicable to

calculations of Kikuchi profiles as well as images produced by inelastic electrons, can be formulated in terms of Bloch waves for which absorptions or both elastic and inelastic electrons are considered. In this theory, the initially generated inelastic electrons are regarded as having spherical wave fronts and during subsequent Bragg diffractions through the rest of the crystal they are treated as forming Bloch waves throughout the section of the reciprocal space in which Bragg diffractions of inelastic electrons take place. This theory is not restricted to any particular inelastic scattering mechanisms, because in the formulation the various scattering amplitudes are treated as parameters. The success of this theory is demonstrated by calculations on some special cases of Kikuchi patterns.

The study of the ordinary dynamical theory of electron diffraction, given in the Appendix, was initiated as a necessary background knowledge in carrying out this work. The solutions of the many beam problem are derived from the dispersion matrix. The use of this matrix allows solutions of problems with multiple excitations easily obtainable, such as the Bragg rescattering of inelastic electrons. The properties of the dispersion matrix and methods for calculating this matrix are discussed in detail. The inter-beam and inter-branch (of the dispersion surface) multiple scattering nature of the Bloch waves in the crystal is made clear through the use, and only through the use, of the dispersion matrix. A more accurate and faster method for computing image problems is developed also by use of this matrix.

II. A THEORY OF KIKUCHI PATTERNS

A. Origin of the Kikuchi Pattern

In addition to the presence of the Bragg spot pattern due to elastic scattering of the incident electron beam, single crystal diffraction patterns often contain a diffuse background intensity distribution and a complex pattern of lines and bands known as Kikuchi pattern. These patterns are formed by inelastically scattered electrons. Inelastic electrons contribute to the diffuse background in general, however, a certain portion of these electrons, for which the Bragg law of reflection is satisfied, forms the Kikuchi pattern. Associated with each (hkℓ) reflection, there is a pair of Kikuchi lines. Between these two lines, an excess or deficiency in electrons may be present. The (hkℓ) pair of the Kikuchi lines is usually observed to be perpendicular to a line joining the (000) and the (hkℓ) spots, as shown in Fig. II.1.

An elementary geometric theory explaining the formation and constrast of the Kikuchi lines may be attained by following Kikuchi.[1] When only a kinematical diffraction condition is satisfied by the incident elastic electron beam, the "diffracted" line of the pair, i.e., the line nearer to the (hkℓ) spot but further away from the (000) spot, always contains an excess number of electrons, while the "transmitted" line always suffers from a deficiency of electrons. In this simple theory the inelastic electrons are regarded as rigid particles, thereby the interactions due to their wave properties are ignored. A further

assumption is that, on traveling through the rest of the crystal after the inelastic electrons are generated, they are Bragg reflected only once.

Now consider the subsequent Bragg reflection of inelastic electrons which suffered only a small energy loss. Referring to Fig. II.2, let the inelastic scattering occurs at p, which, after the inelastic scattering, becomes the origin of a spherical wavelet. The angular distribution of the inelastically scattered electrons is peaked in the direction of the incident beam, $\overline{op}$, and the intensity of these electrons decreases monotonically with increasing scattering angle. Variations in this intensity distribution occur because in certain directions, $\overline{pq}$ and $\overline{pr}$, the Bragg law of reflection is satisfied. The ray $\overline{pq}$ will then be reflected into direction $\overline{qq}'$, and $\overline{pr}$ into $\overline{rr}'$. Since $\overline{op}$ is making a smaller angle with $\overline{pq}$ than $\overline{pr}$, the intensity of the inelastic electrons is greater along $\overline{pq}$ than $\overline{pr}$. Consequently, the intensity along $\overline{qq}'$ becomes greater than that along $\overline{rr}'$. When all possible directions for relections from a given set of crystal planes are considered, it is immediately seen that the directions along which gains or losses of inelastic electrons occur are given by two cones of rays with a semi-vertex angle of $90° - \theta_B$, as shown in Fig. II.3. These cones of rays of inelastic electrons intersect the viewing screen or photo plate some distance away from the crystal to form two branches of a hyperbola which can be closely approximated to straight lines, due to the small value of θ_B. It is seen from this simple theory that the angular separation between the two lines of the Kikuchi pair

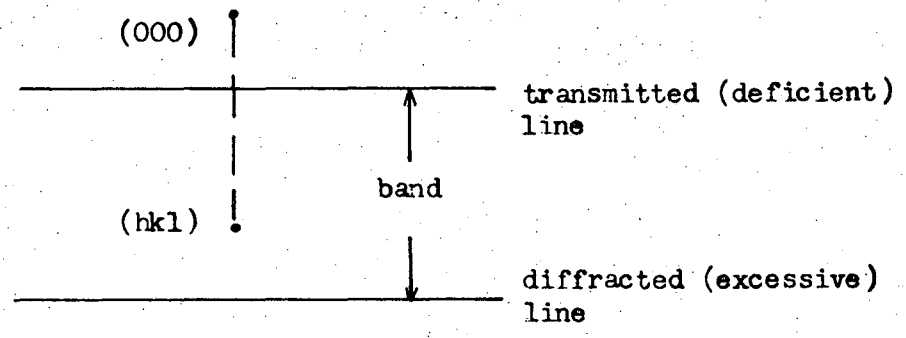

Fig. II.1 Geometry of Kikuchi pattern upon observation.

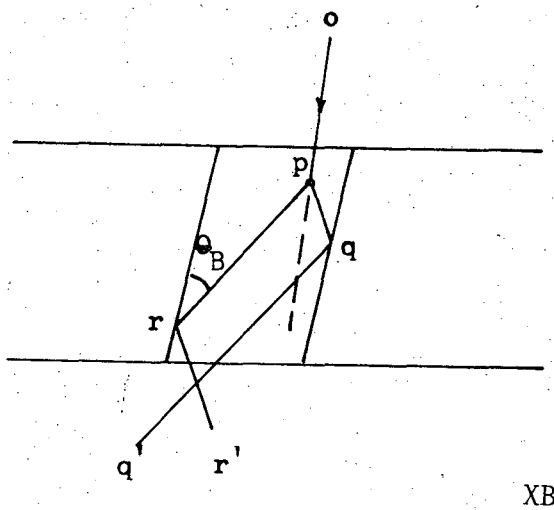

XBL 7111-7676

Fig. II.2 Geometrical explanation of the black-and-white nature of the Kikuchi line pair.

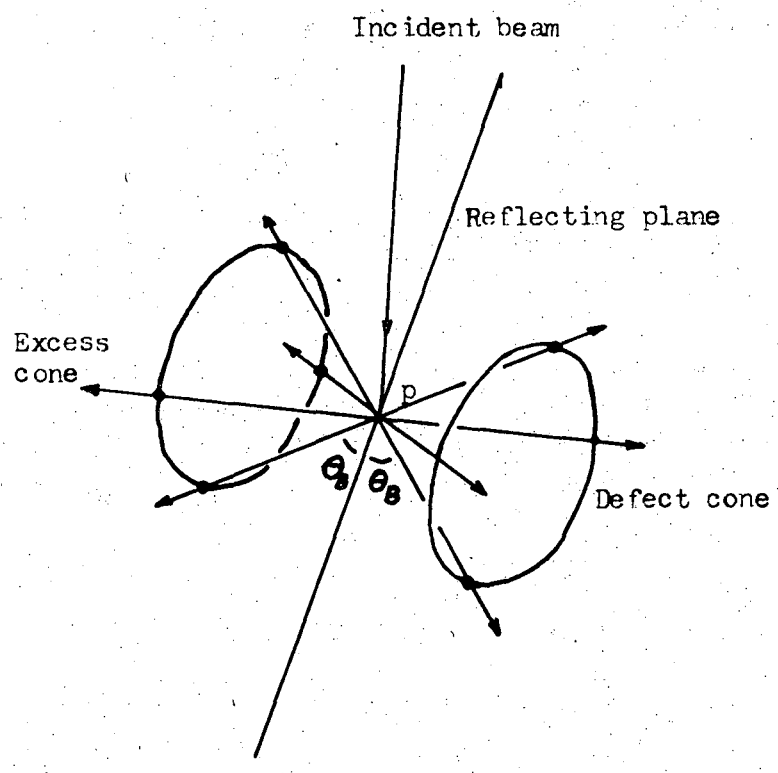

XBL 7111-7677

Fig. II.3 Inelastic electrons generated at an inelastic scattering center p have spherical wave front, but only along directions in two cones separated by a Semi-Vertex angle θ_B the Bragg condition is exactly satisfied.

is $2\theta_B$, an invariant, and that the two lines are placed symmetrically on both sides of the (hkℓ) planes. When specimen is tilted, the Bragg spots do not move, but the individual spot changes intensity. On the other hand, the Kikuchi lines move with the specimen as if they are fixed to the (hkℓ) lattice planes, so that their direction and magnitude of movement reveal the orientation change of the crystal. Notice that in the crystal, many different sets of Bragg conditions may be satisfied by the inelastic electrons, hence even in the two-elastic-beam case, the diffraction pattern contains many pairs of Kikuchi lines.

B. Some Intricacies in the Kikuchi Pattern

Although Kikuchi's simple theory is capable of explaining the origin and contrast of the Kikuchi lines, it suffers from its own over-simplified assumptions. Notice in this theory not only that the wave properties of all electrons are ignored as well as only one source is considered, but also that this argument is strictly geometrical and thus makes its applicability restricted to only the two cones of rays of inelastic electrons separated by an angle $2\theta_B$.

More intricacies of the Kikuchi patterns arise because of the the following reasons: (1). there is always more than one elastic electron beam to serve as a source of inelastic electrons, (2). because of their wave property, electrons are always interacting dynamically, (3). interactions between Kikuchi electrons due to different sets of diffracting planes occur.

Unlike the elastic electrons which can be manipulated to enter the crystal in well collimated beams and hence may possess a well defined planar wave front to start with, inelastic electrons that are generated have spherical wave fronts. One immediate consequence of this property is that for inelastic electrons traveling in directions adjacent to the two Kikuchi cones, Bragg law of reflection is nearly satisfied, thus electron intensity distributions adjacent to the two lines of the Kikuchi pair has to be properly considered. In the region between the two lines of the Kikuchi pair, there exists a non-negligible electron intensity distribution, known as a Kikuchi band. The intensity of a Kikuchi band is observed to change from an excess to a deficiency of electrons with an increase of specimen thickness or a decrease of incident electron beam energy.[2,3] Similar to the subsidiary maxima of Kossel patterns in x-rays, the subsidiary maxima of Kikuchi patterns have also been observed for years, as described by Uyeda et al.[4]

When dynamical diffraction condition for the incident elastic beam is satisfied, situations become even more complicated. Thomas and Bell[5] observed that, when Bragg condition is exactly satisfied, the two lines of the Kikuchi pair may change their contrast. This phenomenon is specimen thickness dependent. New experimental evidences currently reported by Tan, Bell and Thomas[6] also show, contrary to the prediction of Kikuchi's simple theory, which has become almost a common belief, that the Kikuchi angle (Bragg angles for Kikuchi electrons) should always be $2\theta_B$, that the apparent Kikuchi angles can be quite different

from the corresponding Bragg angles. This result is also specimen thickness dependent.

C. A Review of the Existing Theories

Since Kikuchi's explanation of the origin of Kikuchi lines in 1928,[1] the Kikuchi patterns received no adequate attention until 1935 when Laue[7] proposed a theory of Kossel patterns in X-ray diffractions in which a spherical wave is treated dynamically. In this theory Laue used the reciprocity theorem of optics to simplify the necessary mathematics. He also proved the reciprocity theorem for electrons and tried to explain the Kikuchi patterns by extending the Schrodinger equation to the case that a sorce of electrons is present inside the crystal. Laue's theory is superior in the sense that it treated the spherical wave and adopted the dynamical treatment. Later, Laue's theory was extended by Lamla,[8] Artmann,[9] and Fues and Riedel[10] for the explanation of Kikuchi envelopes and bands. Theories based on Laue's original work suffer from one common shortcoming: that in Laue's theory only a point source, or, a source of size smaller than the wave-length of the electron is considered. As a result , the intensity of the Kikuchi pattern is perfectly determined by the orientation of the crystal relative to the viewing screen and is independent of the incident direction of the elastic electron beam.

Although in 1948 Laue presented his theory in revised form in which the source was regarded as the result of inelastic scattering and was extended through out the crystal, the theory was not further developed to draw any conclusive results.[11] However, in 1955 Kainuma arrived at the same conclusion Laue did and applied the theory to a tight binding model

of a crystal to calculate the Kikuchi intensity profiles. He succeeded in correcting Laue's result to bring out the contrast of the Kikuchi line intensity as discussed in association with that of Fig. II.1. A Kikuchi band structure was also evident from Kainuma's theory. However, the intensity in the band is restricted to always having an excess of electrons.[12] Since then Kikuchi patterns have received extensive studies in association with different mechanisms of generating inelastic electrons. The physical processes that are responsible for the production of inelastic electrons involve the generation of many different types of elementary excitations in the crystal. Of these different excitations three types have usually been considered to be the major factors in the production of inelastic electrons. They are the thermal diffuse scattering (phonon excitations), inner shell electron excitations and plasmon excitations. Due to the extremely small amount of energy loss involved with the phonon excitations, aside from the fact that they do give rise to Kikuchi patterns, inelastic electrons generated by this mechanism are usually not separable from the elastic electrons in ordinary electron microscopic work. On the other hand, inner shell electron excitations and plasmon excitations involve relatively large energy losses (e.g., greater than several ev as compared to less than 0.02 ev for phonon excitations), these energy losses can be measured by an energy analyzer.[13-15] In ordinary image work the inelastic electrons thus generated can be filtered out by the use of an energy selecting microscope.[16-19]

The inner shell electron excitons were studied by Kainuma in his theory of Kikuchi patterns.[12] In this theory a Thomas-Fermi model of atoms is used. In 1957, Yoshioka's work on justifying the imaginary part

of the lattice potential by Fourier analysis of the matrix elements of the interaction Hamiltonian of inelastic scattering, in which a tight binding model of crystal was used to produce the inner shell electron excitations, was a major achievement in electron microscopy.[20] Plasmon excitation, or the collective excitation of conduction band electrons, was first studied by Bohm and Pines,[21] and later by Ferrell.[22] The plasmon excitations have a coherence length of typically several hundred angstroms, coupled with the small energy loss and momentum transfer involved, this long coherence length accounts for the similarity in images produced from plasmon scattered electrons and from Bragg beams.[23]

To varying degrees of approximations, thermal diffuse scattering (phonon scattering) is a more extensively studied area. Hall and Hirsch treated the Bragg beams as Bloch waves of the two beam dynamical theory and the inelastic electron beams resulting from phonon excitations as plane waves.[24] This approach was useful in explaining anomalous absorption, but could not give the detailed intensity distributions of the thermally scattered electrons. This work was extended from an Einstein model to a one phonon and to an approximate many phonon Debye model by Hall.[25] Yoshioka and Kainuma[26] used the fundamental equations for dynamical diffuse scattering developed by Yosioka[20] to study thermal absorption from elastic waves, in which, when considering specific cases, the interactions between the diffuse waves were ignored. Other theories, using a weak beam approach or time-independent perturbation methods, have been formulated by several workers, e.g., Kainuma and Yoshioka,[27] Fukuhara,[28] and Kainuma.[29]

Takagi included dynamical interaction of diffuse waves, and, in the

case of two beams in thick crystals, showed that the thermal diffuse scattering can form Kikuchi pattern.[30] Later, his work was extended by Fujimoto and Kainuma to thin crystals.[31] Gjønnes considered diffuse waves as n-beam dynamic. Assuming incoherent diffuse scattering from each region of the crystal,[32] he achieved a qualitative description of the profiles of Kikuchi lines and bands. Based on the theory of Cowley and Pogany,[33] Doyle numerically computed the intensity distributions of the thermal diffuse scattering along a systematic row of excitations in which the n-beam interaction and partial coherence were considered.[34] Most recently, Hall discussed the crystal thickness dependence of Kikuchi bands due to thermal diffuse scattering.[35]

D. Formulation of the Theory

Consider the interaction of high energy electrons with a crystal. The Schrödinger equation of the system is

$$\left\{ -\frac{\hbar^2}{2m} \nabla_r^2 + H_c(q) + H(r,q) - E \right\} |\Psi(r,q)\rangle = 0, \qquad \text{(II.1)}$$

where q is the crystal coordinate, $H_c(q)$ is the Hamiltonian (energy) of the crystal, r is the electron coordinate and H(r,q) is the interaction Hamiltonian between the electron and the crystal. We will not specify the explicit form of the interaction Hamilton in this theory, but rather, a phenomenological description will be introduced later. Physically this corresponds to ignoring the detailed interaction (inelastic scattering) mechanism, and describing the result phenomenologically. The total wave function $|\Psi(r,q)\rangle$ may be expressed as the products of the crystal states $|\phi_j(q)\rangle$ and the corresponding electronic states $|\psi_j(r)\rangle$:

$$|\Psi(r,q)\rangle = \sum_j |\psi_j(r)\rangle |\phi_j(q)\rangle , \qquad \text{(II.2)}$$

where the crystal energy states are given by

$$H_c(q)|\phi_j(q)\rangle = E_j|\phi_j(q)\rangle. \tag{II.3}$$

The substitution of Eq. (II.2) into Eq. (II.1) and then the multiplication of the Hermitian conjugate of the crystal states, i.e., $\sum_j \langle\phi_j(q)|$, yield

$$\left\{-\frac{\hbar^2}{2m}\nabla_r^2 + H_0^0(\bar{r}) - (E-E_0)\right\}|\psi_0(r)\rangle = -\sum_{j\neq 0} H_j^0|\psi_j(r)\rangle, \tag{II.4}$$

$$\left\{-\frac{\hbar^2}{2m}\nabla_r^2 + H_i^i(\bar{r}) - (E-E_i)\right\}|\psi_i(\bar{r})\rangle = -\sum_{j\neq i} H_j^i|\psi_j(\bar{r})\rangle, \tag{II.5}$$

where

$$H_j^i(\bar{r}) = \langle\phi_i(q)|H(r,q)|\phi_j(q)\rangle. \tag{II.6}$$

Using a tight bonding model for the crystal and neglecting the influence of Bragg reflections on the inelastic electrons, i.e., assuming the interaction between the electron and the crystal is purely electrostatic and the inelastic electrons are approximated by their asymptotic form, Yoshioka[20] was able to show that the influence of the inelastic electrons, i.e., the term $-\sum_{j\neq 0} H_0^j|\psi_j(r)\rangle$ on the right hand side of Eq. (II.4), is to effectively introduce an imaginary part into the lattice potential for the elastic electrons (the Fourier series form of the quantity $H_0^0(r)$). Thus, by dropping the ket notation, Eq. (II.4) reduces to the wave equation of elastic electrons

$$\left\{\nabla^2 + 4\pi^2\left[k_{cr}^2 + \sum_{\bar{g}\neq 0} U_g^0 e^{2\pi i\bar{g}\cdot\bar{r}}\right]\right\}\psi_c(\bar{r}) = 0, \tag{II.7}$$

where U_g^o is complex. The meaning of the various quantities and the solution of $\psi_o(\vec{r})$ is described in detail in the appendix, however, with the script "o" now used to denote the ground state of the crystal and correspondingly the elastic electrons.

On the right hand side of Eq. (II.5) the terms $\sum_{j \neq i} H_j^i \psi_j >$ represent the electrons scattered inelastically into or out of the ith state: for j < i, electrons in state j are inelastically scattered into state i and these terms are the source terms for the state i; for j > i, electrons in the state i are scattered into states j and these terms are thus representing the absorption of electrons in state i. Upon casting the absorption terms as the imaginary part of the lattice potential, and noticing that among the source terms only the term $H_i^c \psi_o$ is large enough to be kept, Eq. (II.5) is readily reduced to

$$\left\{ \nabla^2 + 4\pi^2 \left[k_{i\gamma}^2 + \sum_{g \neq 0} U_g^i e^{2\pi i \vec{g} \cdot \vec{r}} \right] \right\} \psi_i = \frac{2m}{\hbar^2} H_o^i \psi_o . \qquad \text{(II.8)}$$

Notice that in Eqs. (II.7) and (II.8) the total electron intensity is automatically conserved. For high energy electrons, the energy difference between the elastic and inelastic electrons is very small compared to the energies of the electrons. The crystal potentials for the elastic and inelastic electrons are then virtually the same for a fairly thick crystal. In a crystal the relation $\phi_c(q) \approx \phi_i(q)$ is always true and hence the quantity $H_o^o(r)$ is practically equal to $H_i^i(r)$. It follows that the real parts of the crystal potentials of both the elastic and the inelastic electrons are the same. This is necessarily so, since the real parts of the lattice potentials give rise only to elastic scatterings.

Because the imaginary parts of the lattice potentials are effectively due to multiple inelastic scatterings, the difference between that of the elastic and inelastic electrons may now be neglected only if the crystal is thick enough to allow many multiple inelastic scatterings to occur.

The solution of Eq. (II.7) is given by the usual Bloch wave solutions of the dynamical theory (with absorption):

$$\psi_o(\bar{r}) = \sum_{\ell} C_{o\ell}\, e^{2\pi i \bar{k}_{o\ell}\cdot\bar{r}} . \tag{II.9}$$

Correspondingly, a Bloch wave type of solution may also be assumed for the inelastic electrosn, i.e.,

$$\psi_i(\bar{r}) = \sum_{h} C_{ih}\, e^{2\pi i \bar{k}_{ih}\cdot\bar{r}} . \tag{II.10}$$

It should be noticed at this point that the inelastic scattering process is to scatter elastic electrons in each Bloch wave $C_{o\ell}\exp(2\pi\, i\bar{k}_{o\ell}\cdot\bar{r})$ into every inelastic beam $C_{ih}\exp(2\pi i\bar{k}_{ih}\cdot\bar{r})$, hence the interaction Hamiltonian H_o^i describing the inelastic scattering process is actually a matrix composed of elements $H_{o\ell}^{ih}$ for all ℓ and h. Accompanying the small energy loss due to the inelastic scattering process, a small momentum transfer must also occur. This momentum transfer can only be furnished by the matrix element $H_{o\ell}^{ih}$, and we may hence write

$$H_{o\ell}^{ih\,\prime} = H_{o\ell}^{ih}\, e^{-2\pi i\, \Delta\bar{k}_{o\ell}^{ih}\cdot\bar{r}} , \tag{II.11}$$

where

$$\Delta\bar{k}_{o\ell}^{ih} = \bar{k}_{o\ell} - \bar{k}_{ih} . \tag{II.12}$$

Along the directions the elastic electrons propagate, i.e., directions for which $\bar{k}_{i\parallel} = \bar{k}_{o\parallel}$ (where $\parallel$ denotes the coordinates parallel to the crystal surface), this momentum transfer is completely specified by the quantity $\Delta\bar{k}_r = \bar{k}_{or} - \bar{k}_{ir}$, the difference of the z-components of the wave vectors referred to the symmetrical orientation of the elastic beam. This procedure corresponds to a lowering of the dispersion surface of the elastic electrons to obtain part of the dispersion surface of the inelastic electrons. Generally, however, since the initial inelastic electron waves generated have spherical wave fronts, therefore a continuous distribution of tie-points on a number of branches of the dispersion surface of various potential energies, i.e., a range of $\bar{k}_{i\parallel}$, must be considered. The quantity $H_{o\ell}^{ih'}$ may then be obtained by adding to $\Delta\bar{k}_r$ another incremental momentum $\Delta\bar{k}$, this situation is shown in Fig. II.4. The quantity $\Delta\bar{k}$ does not further introduce any total energy difference between the elastic and inelastic electrons besides that specified by $\Delta\bar{k}_r$. It does imply, however, that for inelastic electrons on the same branch of the dispersion surface but having different values of $\Delta\bar{k}$, although their total energies are the same, due to the potential differences represented by each different tie-point, their kinetic energies are different.

The substitution of Eqs. (II.9), (II.10), (II.11) and (II.12) into Eq. (II.8) yields

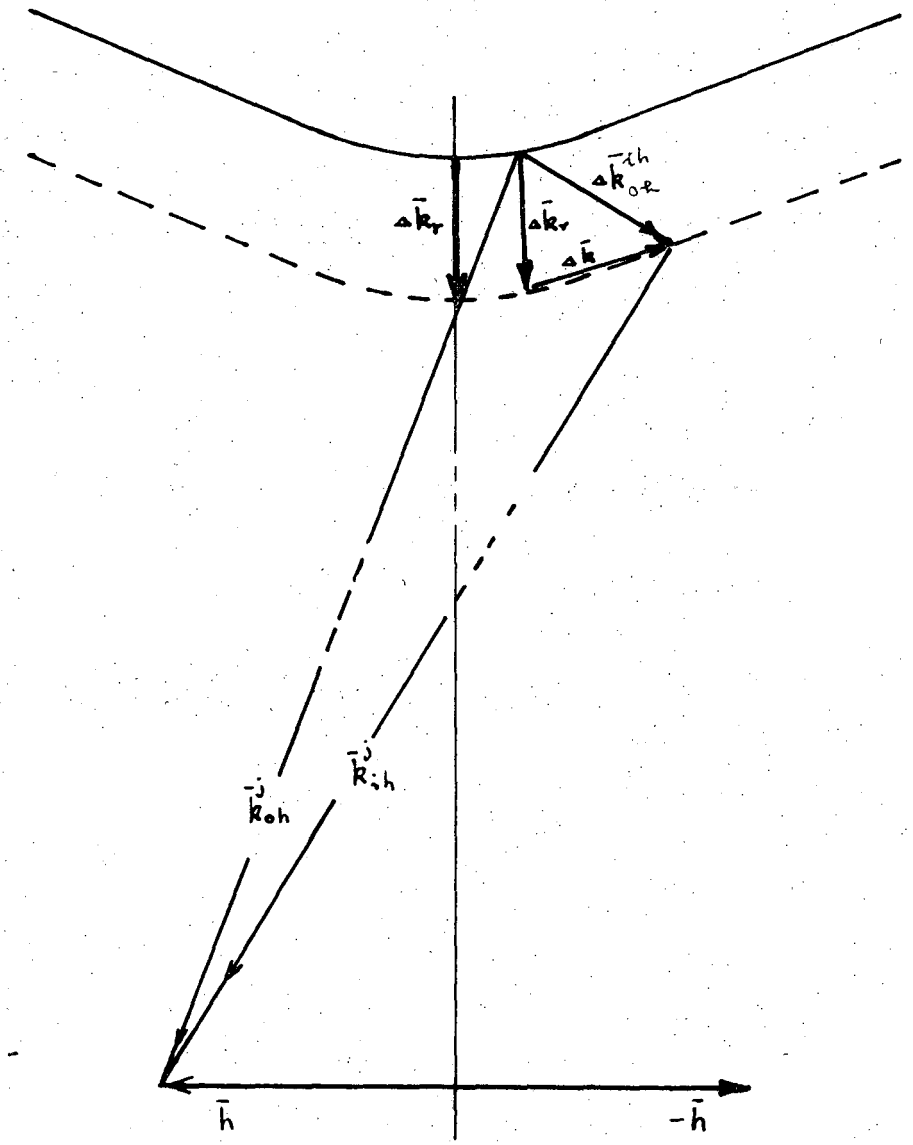

XBL 7111-7678

Fig. II.4. The dispersion surface of elastic beams (solid line) is lowered to obtain part of the dispersion surface of the inelastic electrons (broken line). The quantity $\Delta\bar{k}_r$ specifies the total energy difference between the elastic and inelastic electrons whereas $\Delta\bar{k}$ specifies only the potential (and hence the kinetic) energy differences between inelastic electrons propagating in different directions.

$$\sum_{h} \left\{ C_{ih} \left(k_{ir}^{2} - |\bar{k}_{ih}|^{2} \right) + \sum_{\bar{g} \neq \bar{h}} C_{i\bar{g}} \, U_{\bar{h}-\bar{g}} \right\} e^{2\pi i \bar{k}_{ih} \cdot \bar{r}}$$

$$= \frac{2m}{\hbar^{2}} \sum_{\ell} \sum_{h} H_{o\ell}^{ih'} \, C_{c\ell} \, e^{2\pi i \bar{k}_{ih} \cdot \bar{r}} . \qquad \text{(II.13)}$$

Upon letting the coefficients of each linearly independent term $\exp(2\pi i \bar{k}_{ih} \cdot \bar{r})$ to zero, we get a set of secular equations in the wave vectors $\bar{k}_{ih}$ and the Bloch coefficients C_{ih}:

$$C_{ih} \left(k_{ir}^{2} - |\bar{k}_{ih}|^{2} \right) + \sum_{\bar{g} \neq \bar{h}} C_{i\bar{g}} \, U_{\bar{h}-\bar{g}} = \frac{2m}{\hbar^{2}} \sum_{\ell} H_{o\ell}^{ih'} \, C_{c\ell} . \qquad \text{(II.14)}$$

Equation (II.14) may be written out in explicit form for the (m+1) beams of the inelastic electrons:

$$\begin{bmatrix} k_{ir}^{2} - |\bar{k}_{ic}|^{2} & U_{-\bar{g}_1} & \cdots & U_{-\bar{g}_m} \\ U_{\bar{g}_1} & k_{ir}^{2} - |\bar{k}_{ig_1}|^{2} & \cdots & U_{\bar{g}_1 - \bar{g}_m} \\ \vdots & \vdots & \ddots & \vdots \\ U_{\bar{g}_m} & U_{\bar{g}_m - \bar{g}_1} & \cdots & k_{ir}^{2} - |\bar{k}_{ig_m}|^{2} \end{bmatrix} \begin{bmatrix} C_{ic} \\ C_{ig_1} \\ \vdots \\ C_{ig_m} \end{bmatrix} = \frac{2m}{\hbar^{2}} \underset{\approx}{H_{o}^{2'}} \begin{bmatrix} C_{oo} \\ C_{og_1} \\ \vdots \\ C_{og_n} \\ 0 \\ \vdots \\ 0 \end{bmatrix} . \qquad \text{(II.15)}$$

In writing down Eq. (II.15) it is assumed that there are (n+1) beams for the elastic electrons, where m > n. Equation (II.15) is a set of inhomogeneous algebraic equations of the Bloch amplitudes C_{ih}. The wave vectors can be obtained by solving the homogeneous part of Eq. (II.15)

and (m+1) allowed values of the wave vectors k_{ih} will be obtained. With each value of the allowed wave vectors, Eq. (II.15) can then be used to uniquely determine the Bloch amplitudes. However, it should be desirable to formulate the problem into a set of linear differential equations of z-coordinate only (which is just the equivalent of that of the elastic electrons). For this purpose, use the approximation that $k_{ir}^2 - |\bar{k}_{ih}|^2 \approx 2\,Re(k_{ir})\{k_{ir} - k_{iz}^j + S_{ih}\}$ where $S_{ih} \equiv -(\bar{k}_{i\parallel} + \bar{h})^2 / 2\,Re(k_{ir})$, Equation (II.14) may be written as

$$C_{ih}^j (k_{ir} - k_{iz}^j + S_{ih}) + \sum_{\bar{g} \neq \bar{h}} C_{i\bar{g}}^j \frac{1}{2\xi_{\bar{h}-\bar{g}}} = \frac{2m}{\hbar^2} (H_{0k}^{ih'}) \alpha_j C_{0k}^j , \tag{II.16}$$

where $j = 1, \cdots, n+1$; $C_{0h}^j = 0$, if $j > n+1$, and $\frac{1}{\xi_g} = \frac{U_g}{Re(k_{ir})}$.

In Eq. (II.16), the factor α_j is a phenomenologically introduced parameter to specify the fact that, due to the presence of anomalous absorption, not all types of waves contribute to the generation of inelastic electrons equally. When multiplied by $2\pi i \exp(2\pi\, i\, k_{iz}^j\, z)$, Eq. (II.16) becomes

$$2\pi i\, k_{iz}^j C_{ih}^j \exp(2\pi \cdot k_{iz}^j z) = 2\pi i \Big\{ (k_{ir} + S_{ih}) C_{ih}^j + \sum_{\bar{g} \neq \bar{h}} C_{ig}^j \frac{1}{2\xi_{\bar{h}-\bar{g}}} \Big\} \exp[2\pi i\, k_{iz}^j z] - \frac{4\pi i m}{\hbar^2} \sum_k H_{0k}^{ih'} \alpha_j C_{0k}^j \exp[2\pi i\, k_{iz}^j z]. \tag{II.17}$$

Upon summing all j types of waves, Eq. (II.17) yields

$$\frac{d\psi_{ih}(z)}{dz} = 2\pi i \left\{ (k_{ir} + S_{ih})\,\psi_{ih}(z) + \sum_{\bar{g}\neq\bar{h}} \frac{1}{2\xi_{\bar{h}-\bar{g}}}\,\psi_{ig}(z) \right\}$$

$$+ \sum_{k} f_{ok}^{ih'}\,\psi_{ok}'(z), \qquad \text{(II.18)}$$

where $f_{ok}^{ih} = -\frac{4mi}{\hbar^2} H_{ok}^{ih}$ are the scattering factors for inelastic electrons, and will be treated as parameters in the calculation of Kikuchi patterns; and $\psi_{ok}' = \sum_j \alpha_j C_{ok}^{j} e^{2\pi i \bar{k}_{ik}^{j}\bar{r}}$ is a set of modified Bloch waves in which the Bloch amplitudes are those of the elastic beams (weighted) but their wave vectors are those of the corresponding inelastic beams. On writing out explicitly in a matrix form for the (m+1) beam case, Eq. (II.18) yields

$$\frac{d}{dz}\begin{bmatrix} \psi_{io} \\ \psi_{ig_1} \\ \vdots \\ \psi_{ig_m} \end{bmatrix} = 2\pi i \begin{bmatrix} k_{ir} + S_{io} & \frac{1}{2\xi_{-g_1}} & \cdots & \frac{1}{2\xi_{-g_m}} \\ \frac{1}{2\xi_{g_1}} & k_{ir} + S_{ig_1} & \cdots & \frac{1}{2\xi_{g_1-g_m}} \\ \vdots & & \ddots & \\ \frac{1}{2\xi_{g_m}} & \cdots & & k_{ir} + S_{ig_m} \end{bmatrix} \begin{bmatrix} \psi_{io} \\ \psi_{ig_1} \\ \vdots \\ \psi_{ig_m} \end{bmatrix}$$

$$+ \begin{bmatrix} f_{oo}^{io'} & f_{og_1}^{io'} & \cdots & f_{og_m}^{io'} & 0 & \cdots & 0 \\ f_{oo}^{ig_1'} & f_{og_1}^{ig_1'} & & f_{og_m}^{ig_1'} & 0 & & 0 \\ \vdots & \vdots & & \vdots & & \ddots & \vdots \\ f_{oo}^{ig_m'} & f_{og_1}^{ig_m'} & \cdots & f_{og_m}^{ig_m'} & 0 & \cdots & 0 \end{bmatrix} \begin{bmatrix} \psi_{oo}' \\ \psi_{og_1}' \\ \vdots \\ \psi_{og_m}' \\ 0 \\ \vdots \\ 0 \end{bmatrix}, \qquad \text{(II.19a)}$$

or, in vectorial form,

$$\frac{d}{dz}\underset{\sim}{\psi_i}(z) = 2\pi i\, \underset{\approx}{A}_{\psi}\, \underset{\sim}{\psi_i}(z) + \underset{\approx}{F}'\, \underset{\sim}{\psi_o}'(z). \qquad \text{(II.19b)}$$

It should be noticed that except for the driving term $\underset{\approx}{F}' \underset{\sim}{\psi}_0'(z)$, Eq. (II.19) is identical to the set of linear differential equations for elastic electrons. Because of the inelastic electrons, all elastic beams serve as sources, and the initially generated inelastic waves have spherical wave fronts, the designation of $\psi_{i0}(z)$ is completely arbitrary and hence may just be conveniently chosen to be the beam which is nearest to the transmitted elastic beam ψ_{00}. In the derivation of the above equations it is assumed that if an elastic beam is excited in the crystal then a corresponding inelastic beam must also be excited, however, an inelastic beam may be excited without the excitation of a correspondingly labeled elastic beam. Therefore, the numbers of beams and allowed wave vectors of the elastic electrons are less than that of the inelastic electrons. Nevertheless, the elastic electrons may also be viewed as composed of (m+1) beams but those beams for which $\bar{h} \neq 0$, $\bar{g}_1, \cdots, \bar{g}_n$ are having zero excitation strength. Moreover, for the excited (n+1) beams each beam may also be regarded as having (m+1) types of waves for which if $j > n + 1$, then the Bloch amplitude C^j_{oh} for that type of wave is zero. The matrix element $f^{ih'}_{o\ell}$ in Eq. (II.19) specifies the relative amount of electrons scattered from each elastic beam ℓ into the inelastic beam labeled h, and is a function of the scattering angle between the two beams considered. It is also evident from Eq. (II.15) that in this formulation the initial inelastic waves due only to the so-called intra-band transitions are allowed.

For purpose of simplifying the computations, with the transformations

$$\phi_{ih}(z) = \psi_{ih}(z)\, e^{-2\pi i\, Re(k_{ir})z}, \tag{II.20a}$$

$$\phi'_{o\ell}(z) = \psi'_{o\ell}(z)\, e^{-2\pi i\, Re(k_{ir})z}, \tag{II.20b}$$

$$\tau = \pi i t / Re(\xi_{g_1}), \tag{II.20c}$$

$$\omega_{ih} = Re(\xi_{g_1})\left[\delta_{ih} + i\, Im(k_{ir})\right], \tag{II.20d}$$

$$\xi'_{1(\ell-m)} = \frac{\dfrac{1}{\xi_{g_\ell - g_m}}}{Re\left(\dfrac{1}{\xi_{g_1}}\right)}, \tag{II.20e}$$

Equation (II.19) may be written as

$$\frac{d}{d\tau}\begin{bmatrix}\phi_{io}(\tau)\\ \phi_{ig_1}(\tau)\\ \vdots\\ \phi_{ig_m}(\tau)\end{bmatrix} = \begin{bmatrix} 2\omega_0 & \xi'_{1(-1)} & \cdots & \xi'_{1(-m)}\\ \xi'_{11} & 2\omega_1 & \cdots & \xi'_{1(1-m)}\\ \vdots & \vdots & \ddots & \vdots\\ \xi'_{1m} & \xi'_{1(m-1)} & \cdots & 2\omega_m\end{bmatrix}\begin{bmatrix}\phi_{io}(\tau)\\ \phi_{ig_1}(\tau)\\ \vdots\\ \phi_{ig_m}(\tau)\end{bmatrix}$$

$$+\begin{bmatrix} f_{oo}^{io} & f_{og_1}^{io} & \cdots & f_{og_m}^{io} & 0 & \cdots & 0\\ f_{oo}^{ig_1} & f_{og_1}^{ig_1} & \cdots & f_{og_m}^{ig_1} & 0 & \cdots & 0\\ \vdots & \vdots & & \vdots & \vdots & & \vdots\\ f_{oo}^{ig_m} & f_{og_1}^{ig_m} & \cdots & f_{og_m}^{ig_m} & 0 & \cdots & 0\end{bmatrix}\begin{bmatrix}\phi'_{oo}(\tau)\\ \phi'_{og_1}(\tau)\\ \vdots\\ \phi'_{og_m}(\tau)\\ 0\\ \vdots\\ 0\end{bmatrix}, \tag{II.21a}$$

or

$$\frac{d}{dt}\underset{\sim}{\phi}_i(t) = \underset{\approx}{A}\,\underset{\sim}{\phi}_i(t) + \underset{\approx}{F}\,\underset{\sim}{\phi}_o'(t) \tag{II.21b}$$

where $f_{ch}^{ih} = -\dfrac{4m\xi_{g_1}}{\hbar^2} H_{ch}^{ih\,\prime}$.

The solution of Eq. (II.21) is given by

$$\underset{\sim}{\phi}_i(t) = \underset{\approx}{\Phi}(t-t_0)\,\underset{\sim}{\phi}_i(t_0) + \int_{t_0}^{t} \underset{\approx}{\Phi}(t-\lambda)\,\underset{\approx}{F}\,\underset{\sim}{\phi}_o'(\lambda)\,d\lambda\,. \tag{II.22}$$

where $\underset{\approx}{\Phi}(t-\lambda)$ is the dispersion matrix of the homogeneous system and is equal to $\exp[\underset{\approx}{A}(t-\lambda)]$.

Careful examinations of Eq. (II.22) reveal another important characteristic of the dispersion matrix, that is, the dispersion matrix is the Green's function of the system. In general, the Green's function of any system can nev-er be simply equal to the solution of its associated homogeneous system. In our formulation of the problem, the Green's function is easily obtained, i.e., it is just the dispersion matrix of the associated homogeneous system. In the paper of Kainuma,[12] however, the Green's function of the system is not so readily obtainable, and Kainuma simply used the solution of the corresponding homogeneous system for the Green's function of his so-called reciprocal waves. In this sense, the theory of Kainuma and other related works are in error.

Since the inelastic electron waves generated have a spherical wave front, it appears that in order to solve the problem, all values of $\bar{k}_{ix}$ must be considered for all beams. However, we shall see, from the following theorem for the case of an infinite number of systematically excited

beams, that this needs only to be done through the first Brillouin zone for all beams; or for a single beam, say, ψ_{io}, for all values of $\bar{k}_{ix}$.

<u>THEOREM</u>: Consider a systematic row of excitations of inifinite number of beams for which the elastic beams are fixed, then the set of linear differential equations given by Eqs. (II.19) and (II.21) are redundant with respect to the systematic row of reciprocal lattice vectors considered, i.e., for integers ℓ, m

$$\psi_{\ell\bar{g}}(\bar{k}_{ix}+m\bar{g}) = \psi_{(\ell+m)\bar{g}}(\bar{k}_{ix}). \qquad \text{(II.23)}$$

<u>Proof</u>: For purpose of proving this theorem, we replace the last term on the right hand side of Eq. (II.19) by a single excitation column matrix $\underset{\sim}{f}(\bar{k}_{ix})$. Equation (II.19) may now be written as

$$\frac{d}{dz}\begin{bmatrix} \vdots \\ \psi_{-g}(\bar{k}_{ix}) \\ \psi_0(\bar{k}_{ix}) \\ \psi_g(\bar{k}_{ix}) \\ \vdots \end{bmatrix} = 2\pi i \begin{bmatrix} \cdots & k_{iz}+S_{-g} & \frac{1}{2\xi_g} & \frac{1}{2\xi_{2g}} & \cdots \\ \cdots & \frac{1}{2\xi_g} & k_{iz}+S_0 & \frac{1}{2\xi_g} & \cdots \\ \cdots & \frac{1}{2\xi_{2g}} & \frac{1}{2\xi_g} & k_{iz}+S_g & \cdots \\ & \vdots & \vdots & \vdots & \end{bmatrix} \begin{bmatrix} \vdots \\ \psi_{-g}(\bar{k}_{ix}) \\ \psi_0(\bar{k}_{ix}) \\ \psi_g(\bar{k}_{ix}) \\ \vdots \end{bmatrix}$$

$$+ \begin{bmatrix} \vdots \\ f(\bar{k}_{ix}-\bar{g}) \\ f(\bar{k}_{ix}) \\ f(\bar{k}_{ix}+\bar{g}) \\ \vdots \end{bmatrix} . \qquad \text{(A)}$$

Consider $\frac{d}{dz}\,\underset{\sim}{\psi}(\bar{k}_{ix}+\bar{g})$, Eq. (A) then becomes

$$\frac{d}{dz}\begin{bmatrix} \vdots \\ \psi_{-g}(\bar{k}_{ix}+\bar{g}) \\ \psi_0(\bar{k}_{ix}+\bar{g}) \\ \psi_g(\bar{k}_{ix}+\bar{g}) \\ \vdots \end{bmatrix} = 2\pi i \begin{bmatrix} \cdots & \vdots & \vdots & \vdots & \\ \cdots & k_{ir}+S_0 & \frac{1}{2\xi_g} & \frac{1}{2\xi_{2g}} & \cdots \\ \cdots & \frac{1}{2\xi_g} & k_{ir}+S_g & \frac{1}{2\xi_g} & \cdots \\ \cdots & \frac{1}{2\xi_{2g}} & \frac{1}{2\xi_g} & k_{ir}+S_{2g} & \cdots \\ & \vdots & \vdots & \vdots & \end{bmatrix} \begin{bmatrix} \vdots \\ \psi_g(\bar{k}_{ix}+\bar{g}) \\ \psi_0(\bar{k}_{ix}+\bar{g}) \\ \psi_g(\bar{k}_{ix}+\bar{g}) \\ \vdots \end{bmatrix}$$

$$+ \begin{bmatrix} \vdots \\ f(\bar{k}_{ix}) \\ f(\bar{k}_{ix}+\bar{g}) \\ f(\bar{k}_{ix}+2\bar{g}) \\ \vdots \end{bmatrix} . \qquad \text{(B)}$$

A direct c omparison reveals that Eq. (A) is exactly like Eq. (B), if and only if

$$\psi_{-g}(\bar{k}_{ix}+\bar{g}) = \psi_0(\bar{k}_{ix}),$$

$$\psi_0(\bar{k}_{ix}+\bar{g}) = \psi_g(\bar{k}_{ix}),$$

$$\vdots$$

and in general

$$\psi_{\ell\bar{g}}(\bar{k}_{ix}+m\bar{g}) = \psi_{(\ell+m)g}(\bar{k}_{ix}). \tag{C}$$

QED

It is evident from this theorem that for the many-beam case, the range of $\bar{k}_{ix}$ need only to be considered inside the first Brillouin zone, or consider only one of the Bloch waves, e.g., $\psi_{i0}(\bar{k}_{ix})$ for all of $\bar{k}_{ix}$. For finite number of beams considered, this theorem, i.e., Eq. (II.23), is of course not exactly satisfied. The accuracy of the results then depends on the value of $\bar{k}_{ix}$ as well as the number of beams considered.

One of the factors that must be considered before going on further into the details of the calculation of the Kikuchi pattern, is the coherence property of the electrons. We have so far regarded the electrons generated by the source, i.e., the electron gun, as monoenergetic with a constant rate of emission, i.e., the electron wave generated is monochromatic. Nevertheless, electron waves generated from a real physical source can never be strictly monochromatic, and should be described by a spectral line with a definite width. The produced electrons may be expressed, according to Fourier's theorem, as the sum of strictly monochromatic and hence infinitely long wave trains. The theory presented so far is essentially concerned with a single component of

this Fourier representation. With a monochromatic source, the electron waves propagating through any point p in space is of constant amplitude while the phase varies linearly with time. This is no longer the case with any real source: the amplitude and phase undergo irregular fluctuations, the rapidity of which depends essentially on the spectral width $\Delta\nu$. The amplitude remains substantially constant only during a time interval $\Delta t \ll \frac{1}{\Delta\nu}$, in such a time interval the change of the relative phase of any two Fourier components is much less than 2π and the addition of such components represents a wave which in this time interval behaves like a monochromatic wave with the mean frequency of the two. This is not true for any much longer time intervals. The characteristic time interval $\Delta t = \frac{1}{\Delta\nu}$ is called the coherence time.

Equivalently, at a fixed time t_o, along the path the electron travels, any two points p_1 and p_2 separated by a distance d will see a monochromatic wave as having a constant amplitude at both points with a phase difference $2\pi \frac{d}{\lambda}$, where λ is the wave length. This is not true for any electron waves produced by a real source. The difference of the phases between the points due to two Fourier components is much less than 2π only if $d \ll \frac{\lambda^2}{\Delta\lambda}$, and the addition of this two components yields essentially a constant amplitude at the two points considered. In this small space interval the wave may be regarded as monochromatic with the mean wave length of the two. The characteristic distance interval is called the coherence length.

The recorded experimental results of a diffraction experiment may be viewed as the interference pattern from all the waves involved, i.e., the result may be interpreted as that produced by secondary waves emitted

by all scatterers along the path the wave propagated. The physical significance of the coherence length is then the measure of the distance over which two equivalent polychromatic sources would produce a perfect interference pattern. This means we must expect strong interference between the waves generated at the two points if their separation is very much smaller than the coherence length of the waves, and no interference at all if the two points are separated by a distance much longer than the coherence length. In the latter case only the sum of the intensities produced by individual Fourier components of the waves would be recorded.

Despite the polychromatic nature of the electron waves produced by a real source, in diffraction experiments the incident (elastic) electron waves are always considered as fully coherent, i.e., as if the electron waves are truly monochromatic. This is so because in diffraction experiments the crystals studied usually are of thicknesses much smaller than the coherence length of electron waves used, e.g., at 100 kv, $\frac{\lambda}{\Delta\lambda} = \frac{E}{\Delta E} \approx 10^5$, if ΔE is taken as 1 ev, the coherence length of the electrons is approximately 3700 Å. For much thicker crystals the above conclusion is not true, however, in practice this is a case of seldom interest since then the electrons will be practically all absorbed, an experimental condition certainly can be avoided. In an alternative way, this conclusion may also be arrived at quantum mechanically. By the time the electron beam reaches the specimen, the wave packet of one electron has spread over a region large in dimensions compared to the crystal thickness. Taking the probability amplitude of finding the electron at any point in the crystal at a given time as a constant is therefore a good approximation; elastic scattering of this wave packet can then be localized within the crystal, so it is coherent.

For inelastic electrons generated within the crystal, however, as a result of the random phase shift due to the inelastic scattering, the electrons will not possess as long a coherence length as the elastic electrons. It is then only necessary to consider the interference of the waves generated within a coherence length, i.e., wave amplitudes should be added only over the range of a coherence length within which the waves generated from each part is closely correlated. The resultant intensity of the inelastic electrons will be the sum of intensities produced of slices, each has a thickness equal to the coherence length of the electrons.

The collective excitation of conduction band electrons (a plasmon) is coherent typically over a few hundred angstroms. Coupled with the small amount of energy and momentum transfers involved, this long coherence length accounts for both the high directionality[22] (in the direction of the elastic beams) of the plasmon scattering and the remarkable similarity in the images produced from the plasmon scattered inelastic electrons and the elastic Bragg beams.[23] For phonon excitations, the range of coherent interaction between the diffusely scattered waves is the length of the phonon in the direction of the incident beam and is very short. For inner shell electron excitations, the random ionization process usually leaves the generated inelastic electrons with no appreciable coherence length whatsoever.

Because of the relatively large scattering angles involved, for Kikuchi patterns to form at all, only the inelastic electrons produced by phonon and electronic scattering contribute significantly. It is thus only necessary to treat the inelastic electrons as fully incoherent. On solving Eq. (II.21) for specific cases, a thin slice

approach may be adopted: within the slice an incremental inelastic wave is generated, as given by the last column matrix of Eq. (II.21), and upon traveling through the rest of the crystal, Bragg diffractions occur, as described by the rest of Eq. (II.21). Finally the intensities from each slice may be summed up to find the total intensity. This procedure is equivalent to taking the initial wave $\phi_i(t_o) = 0$ for all t_o, but there exists a delta function type of source at each slice of the crystal which gives the incremental amplitude of the wave. Thus, for the final intensity, Eq. (II.21) new yields

$$\underset{\sim}{I}_i(t) = \int_0^t \int_0^t \left\{ d\,\underset{\sim}{\psi}_i(t-\lambda) \right\} \left[d\,\underset{\sim}{\psi}_i^*(t-\eta) \right] \delta(\lambda-\eta)$$

$$= \int_0^t \int_0^t \left\{ \underset{\approx}{\Phi}(t-\lambda)\, \underset{\approx}{F}\, \underset{\sim}{\phi}_o'(\lambda) \right\} \left[\underset{\approx}{\Phi}(t-\eta)\, \underset{\approx}{F}\, \underset{\sim}{\phi}_o'(\eta) \right]^* \delta(\eta-\lambda)\, d\lambda\, d\eta \,, \tag{II.24}$$

where $\left\{ d\,\underset{\sim}{\psi}_i(t-\lambda) \right\}$ is a diagonal square matrix

$$\begin{bmatrix} d\psi_{i0}(t-\lambda) & 0 & \cdots & 0 \\ 0 & d\psi_{ig_1}(t-\lambda) & \cdots & 0 \\ \vdots & \vdots & \ddots & \vdots \\ 0 & 0 & \cdots & d\psi_{ig_n}(t-\lambda) \end{bmatrix}$$

and * denotes the complex conjugate. Finally, the intensity distributions of the inelastic electrons is given by

$$\underset{\sim}{I}(\underset{\sim}{x}) = \sum_{i=1}^{\infty} \underset{\sim}{I}_i(\underset{\sim}{x}). \tag{II.25}$$

E. Special Cases of the Kikuchi Pattern

It is clear that many beam considerations will be required for calculating the Kikuchi patterns for a general case. Such a case will be discussed later. However, because of the fact that in this formulation absorptions of both the elastic and inelastic electrons are considered, it will soon be clear that for the purpose of explaining a majority aspects of the behavior of the Kikuchi pattern, a two-beam (for inelastic electrons) approximation will be sufficient. One advantage of using this approximation is that the solutions of the intensity equations are readily obtainable in analytical forms. For inelastic electrons held at two beams, then with reference to the diffraction conditions of the incident elastic beam, the results may be categorized in three cases: (1) The asymmetric one beam case. In this case the elastic electron beam is incident at an angle to the diffracting planes greater than the corresponding Bragg angle, the result is the formation of the black-and-white (deficient and excess in the number of electrons) Kikuchi line pair; (2) The symmetrical one beam case. In this case the elastic electron beam is incident in a direction parallel to the diffracting planes and results in the formation of a symmetrical Kikuchi band. The Kikuchi band is observed to change from an excess (white band) to a deficiency (black band) of electrons with an increase of specimen thickness or a decrease of the incident electron beam accelerating voltage; and (3) The dynamical two-beam case. In this case the elastic electron

beam is incident at an angle equal to or nearly equal to the Bragg angle and hence satisfying the dynamical diffraction conditions. As may be expected, this is the most complicated and interesting case. Dependent on the length of the operating reciprocal lattice vector, the Kikuchi pattern in this case may exhibit a pair of lines whose contrast may reverse as the specimen thickness changes, or a pair of lines whose spacing varies with specimen thickness.

For all cases considered, the two-beam dispersion matrix for the inelastic electrons must be used. This matrix is given by (see Appendix)

$$\underset{\approx}{\bar{\Psi}}_i(t-z) = \begin{bmatrix} \psi_{io}(t-z) & \psi_{ig}(t-z) \\ \psi_{ig}(t-z) & \psi^{+}_{io}(t-z) \end{bmatrix}, \tag{II.26}$$

where t is the crystal thickness. The quantities $\psi_{io}(t-z)$ and $\psi_{ig}(t-z)$ are just the wave functions of the transmitted and the diffracted beams in the ordinary two-beam dynamical theory:

$$\psi_{io}(t-z) = C^1_{io}\,\psi^1_i(t-z) + C^2_{io}\,\psi^2_i(t-z), \tag{II.26a}$$

$$\psi_{ig}(t-z) = C^1_{ig}\,\psi^1_i(t-z) + C^2_{ig}\,\psi^2_i(t-z); \tag{II.26b}$$

and

$$\psi^{+}_{io}(t-z) = C^2_{io}\,\psi^1_i(t-z) + C^1_{io}\,\psi^2_i(t-z), \tag{II.26c}$$

where

$$C^1_{io} = \frac{1}{2}\left(1+\frac{w_i}{\sqrt{1+w_i^2}}\right), \quad C^2_{io} = \frac{1}{2}\left(1-\frac{w_i}{\sqrt{1+w_i^2}}\right),$$

$$-C^1_{ig} = C^2_{ig} = \frac{1}{2}\,\frac{1}{\sqrt{1+w_i^2}}; \tag{II.26d}$$

$$\psi^1_i(t-z) = \exp\left\{\left[-\pi i\,\mu^1_i + 2\pi i\left(k^i_{rz} - \frac{\sqrt{1+w_i^2}}{2\xi_g}\right)\right](t-z)\right\}, \tag{II.26e}$$

$$\psi_i^2(z-z) = \exp\left\{\left[-\pi\mu_i^2 + 2\pi i\left(k_{rz}^i + \frac{\sqrt{1+w_i^2}}{2\xi_g}\right)\right](z-z)\right\}, \qquad \text{(II.26f)}$$

with $$\mu_i^1 = \frac{1}{\xi_{ic}'} - \frac{1}{\xi_{ig}'\sqrt{1+w_i^2}}, \quad \mu_i^2 = \frac{1}{\xi_{ic}'} + \frac{1}{\xi_{ig}'\sqrt{1+w_i^2}}, \qquad \text{(II.26g)}$$

being the absorption parameters of the type I and type II waves respectively, and

$$k_{rz}^i = Re\,(k_r^i)\cos\theta_B \,. \qquad \text{(II.26h)}$$

In writing down Eq. (II.26) we have adopted the conventional use of the quantities that $s_i = g\Delta\theta_i$, $w_i = s_i Re(\xi_g)$ (See Appendix for details).

In the following we present the results in the order given above. It is further assumed that only inelastic electrons in the first excited state, i.e., i = 1, contributes most significantly in the formation of the Kikuchi pattern. A many-beam case shall also be considered.

1. <u>Asymmetric One-Beam Case--Formation of the Kikuchi Line Pair</u>

In this case the incident elastic electron beam makes an angle with the operating diffraction planes greater than the Bragg angle and hence the rel-point lies well inside the Ewald sphere. We have now, ω_o, the deviation parameter for the elastic beams, approaching infinity, C_{oo}^1, the Bloch coefficient of the type I wave of the elastic beam, closely equals unity and all other Bloch coefficients are approximately zero. The absorption parameter of this excited beam is $\mu_o^1 = \frac{1}{\xi_{oo}'}$. Under such circumstances, the intensity of the inelastic transmitted beam at the vicinity of the Bragg position is given by

(from Eq. II.24)

$$I_{io}(w_i) = \frac{1}{2\pi}\left(\frac{\alpha_1}{\xi'_{oc}}\right)^2 \Bigg\{ \frac{1}{\frac{1}{\xi'_{oc}} - \frac{1}{\xi'_{io}} + \frac{1}{\xi'_{ig}\sqrt{1+w_i^2}}} \left(f_{oo}^{io} C_{io}^1 + f_{oo}^{ig} C_{ig}^1 \right)^2$$

$$\times \left[e^{-2\pi\left(\frac{1}{\xi'_{io}} - \frac{1}{\xi'_{ig}\sqrt{1+w_i^2}}\right)t} - e^{-2\pi t/\xi'_{oc}} \right]$$

$$+ \frac{\left(f_{oo}^{io} C_{io}^2 + f_{oo}^{ig} C_{ig}^2 \right)^2}{\frac{1}{\xi'_{io}} - \frac{1}{\xi'_{oo}} - \frac{1}{\xi'_{ig}\sqrt{1+w_i^2}}} \left[e^{-\frac{2\pi t}{\xi'_{oc}}} - e^{-2\pi\left(\frac{1}{\xi'_{io}} + \frac{1}{\xi'_{ig}\sqrt{1+w_i^2}}\right)t} \right]$$

$$+ 2\,\mathrm{Re}\left[\frac{\left(f_{oo}^{io} C_{io}^1 + f_{oo}^{ig} C_{ig}^1 \right)\left(f_{oo}^{io} C_{io}^2 + f_{oo}^{ig} C_{ig}^2 \right)}{\frac{1}{\xi'_{io}} - \frac{1}{\xi'_{oo}} - \frac{i\sqrt{1+w_i^2}}{\xi_g}} \right]$$

$$\times \left[e^{-2\pi t/\xi'_{oc}} - e^{-2\pi t/\xi'_{io} + 2\pi i\sqrt{1+w_i^2}\, t/\xi_g} \right] \Bigg\},$$

(II.27a)

and an identical expression for the diffracted beam is obtained if the substitutions $C_{io}^1 \to C_{ig}^1$, $C_{io}^2 \to C_{ig}^2$, $C_{ig}^1 \to C_{io}^2$, $C_{ig}^2 \to C_{io}^1$ are made in Eq. (II.27a) (where $\to$ means "change to"), i.e.,

$$I_{ig}(w_i;\, C_{ic}^1, C_{io}^2, C_{ig}^2, C_{ig}^1)$$

$$= I_{io}(w_i;\, C_{ig}^1, C_{ig}^2, C_{ic}^2, C_{io}^1). \qquad \text{(II.27b)}$$

By noticing the fact that in this case $f_{oo}^{io} >> f_{oo}^{ig}$, Eq. (II.27) readily yields a black-and-white pair of Kikuchi lines. The oscillating terms in Eq. (II.27) are not very important, unless the specimen is extremely thin. Figure II.5 shows this situation for various specimen thicknesses, where the values $\xi_{oo}' = \xi_{io}'$ and $f_{oo}^{ig}/f_{oo}^{io} = 0$ are used. It is clearly seen that $I_{io}(\omega_i)$ always has a minimum value in the vicinity of $\omega_i = 0$, while $I_{ig}(\omega_i)$ always has a maximum value at $\omega_i = 0$. However, for very thin crystals, the maximum value of $I_{ig}(\omega_i)$ may not always be larger than the minimum value of $I_{io}(\omega_i)$. When the value $f_{oo}^{ig}/f_{oo}^{io} = 0$ is used, $I_{ig}(\omega_i)$ is symmetric in ω_i, in fact, $I_{ig}(\omega_i)$ is then proportional to $1/(1+\omega_i^2)^{1/2}$. If the condition that $f_{oo}^{ig}/f_{oo}^{io} = 0$ is not satisfied, a certain amount of asymmetry is introduced into both $I_{io}(\omega_i)$ and $I_{ig}(\omega_i)$ and thereby broadening these intensity curves. The experimental fact that the Kikuchi line pair for a small rel-vector is a less pronounced line pair can be explained by the above discusion. (1) On moving away from the position $\omega_i = 0$ the function $1/(1+\omega_i^2)^{1/2}$ falls off more rapidly for long rel-vectors, and (2) the condition $f_{oo}^{ig}/f_{oo}^{io} = 0$ is not well satisfied by short rel-vector diffractions. When points on the pair of lines are far away from the central porition of the pattern, the black-white nature of the lines at these points will also tend to be diminished, since then $f_{oo}^{ig}/f_{oo}^{io} = 0$ is again not satisfied.

2. <u>The Symmetrical One-beam case--Formation and Behavior of Kikuchi Bands</u>

In this case the elastic electron beam is parallel to the set of diffracting planes by which Bragg diffraction of the inelastic electrons occurs. No appreciable elastic waves other than the type II wave of the transmitted beam is excited, i.e., $C_{oo}^2 = 1$, $C_{oo}^1 = C_{og}^1 = C_{og}^2 = 0$.

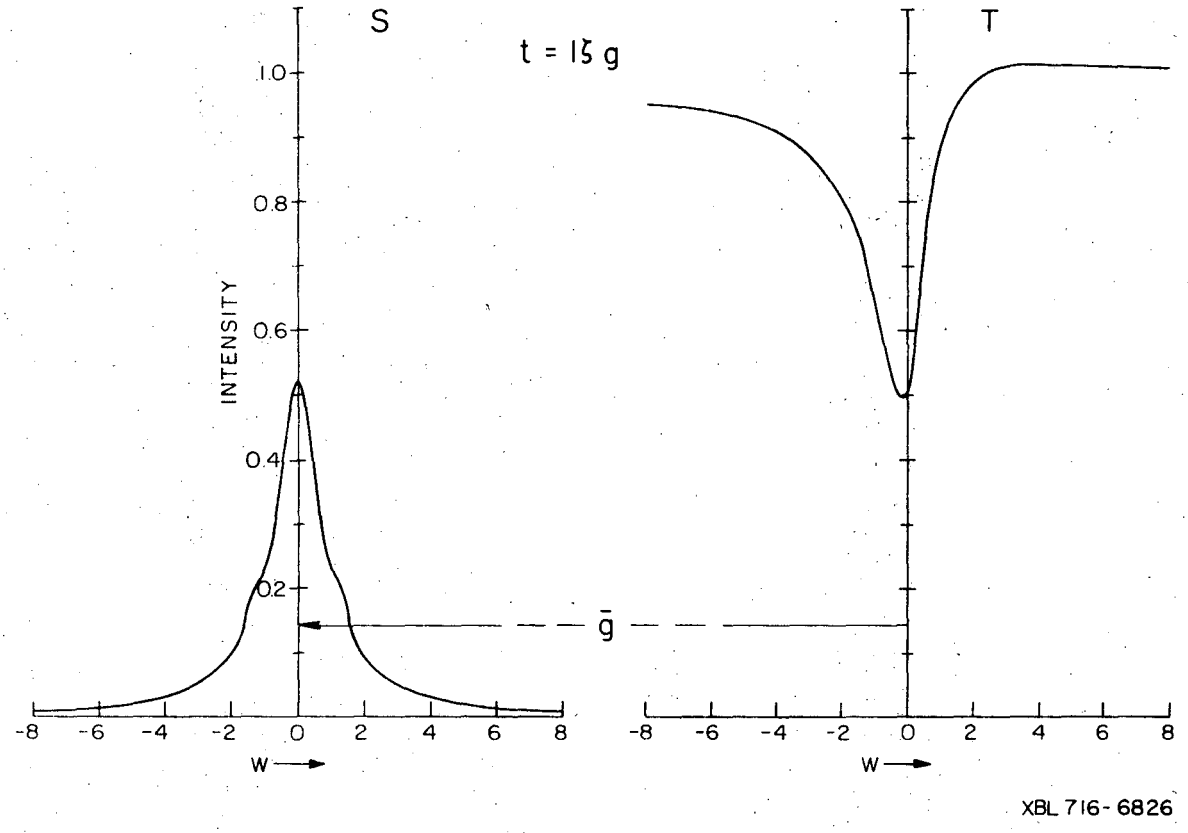
S
T
t = 15 g
1.0
0.8
0.6
0.4
0.2
INTENSITY
ḡ
-8 -6 -4 -2 0 2 4 6 8
W
-8 -6 -4 -2 0 2 4 6 8
W
XBL 716-6826

Fig.II. 5a

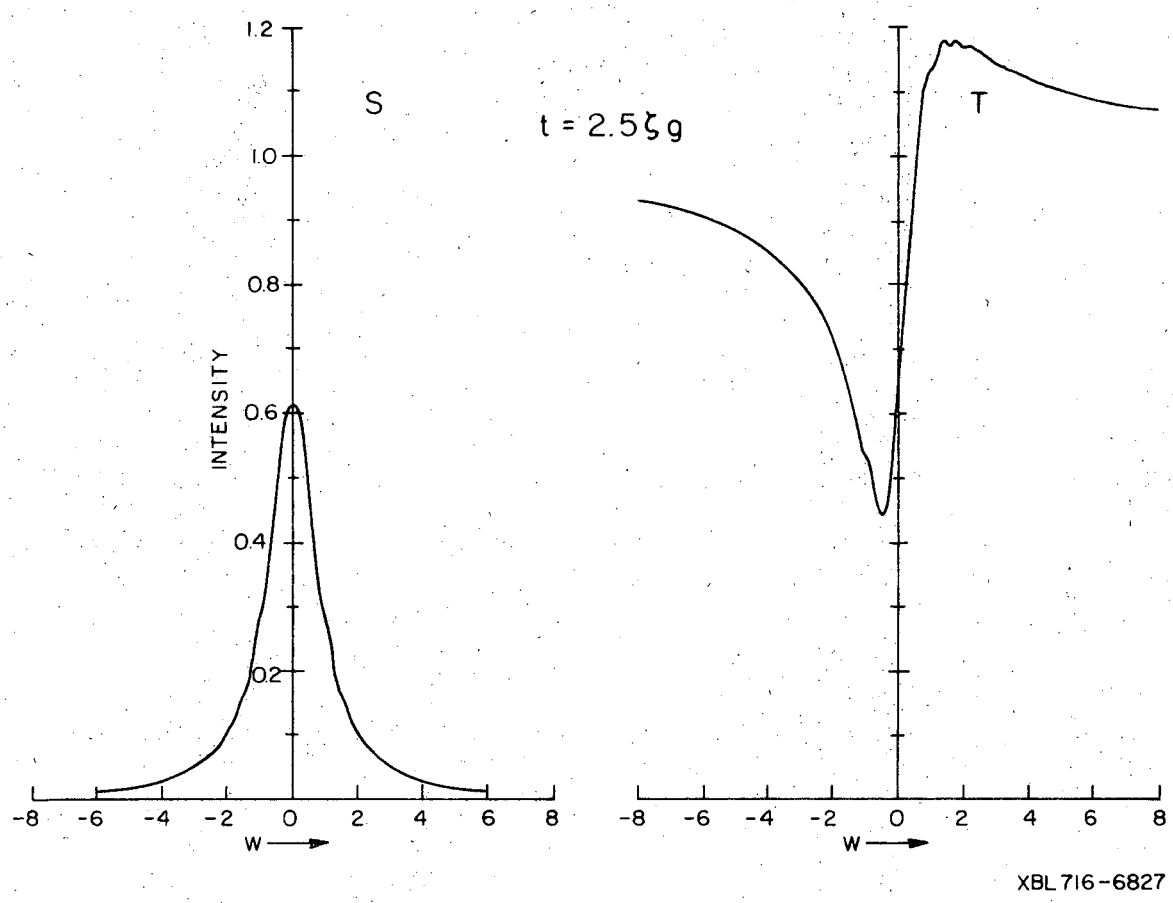
S
t = 2.5ζg
T
INTENSITY
1.2
1.0
0.8
0.6
0.4
0.2
-8 -6 -4 -2 0 2 4 6 8
W
-8 -6 -4 -2 0 2 4 6 8
W
XBL 716-6827

Fig.II. 5b

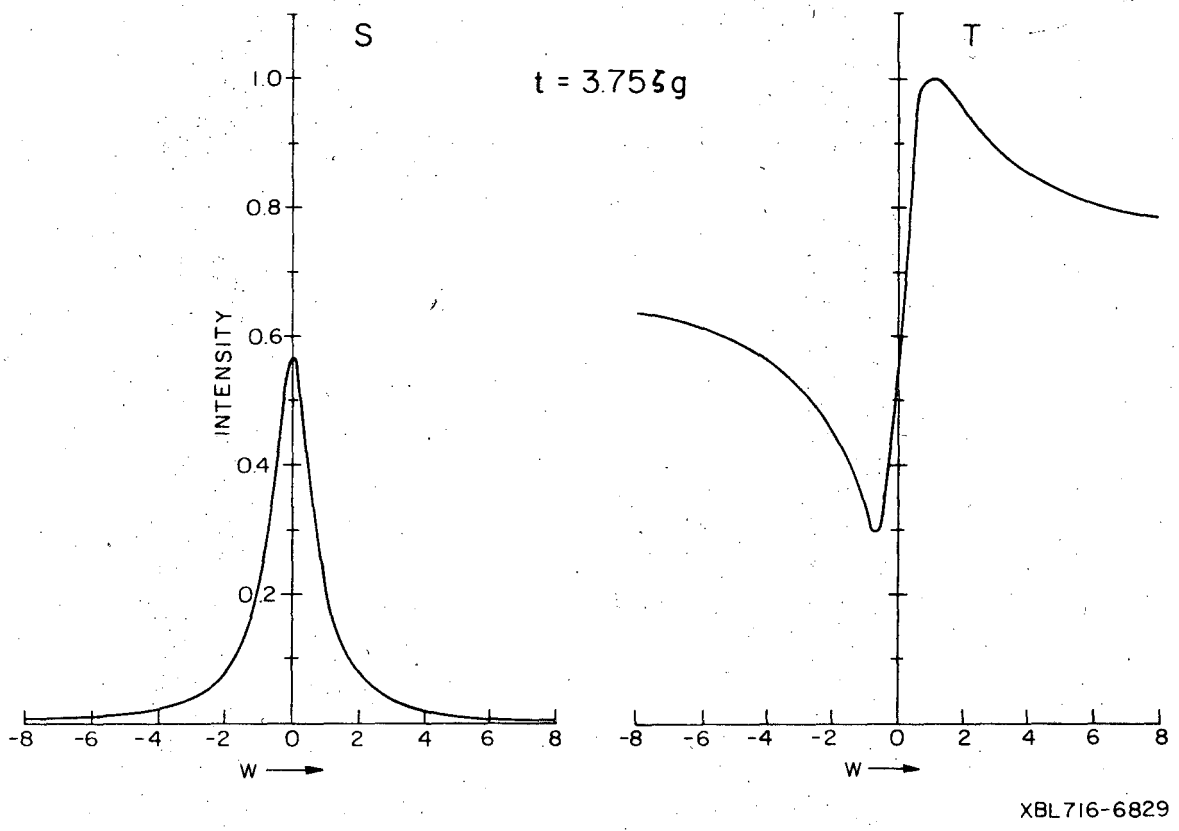

Fig.II. 5c

0 0 0 0 3 7 0 0 0 4 3

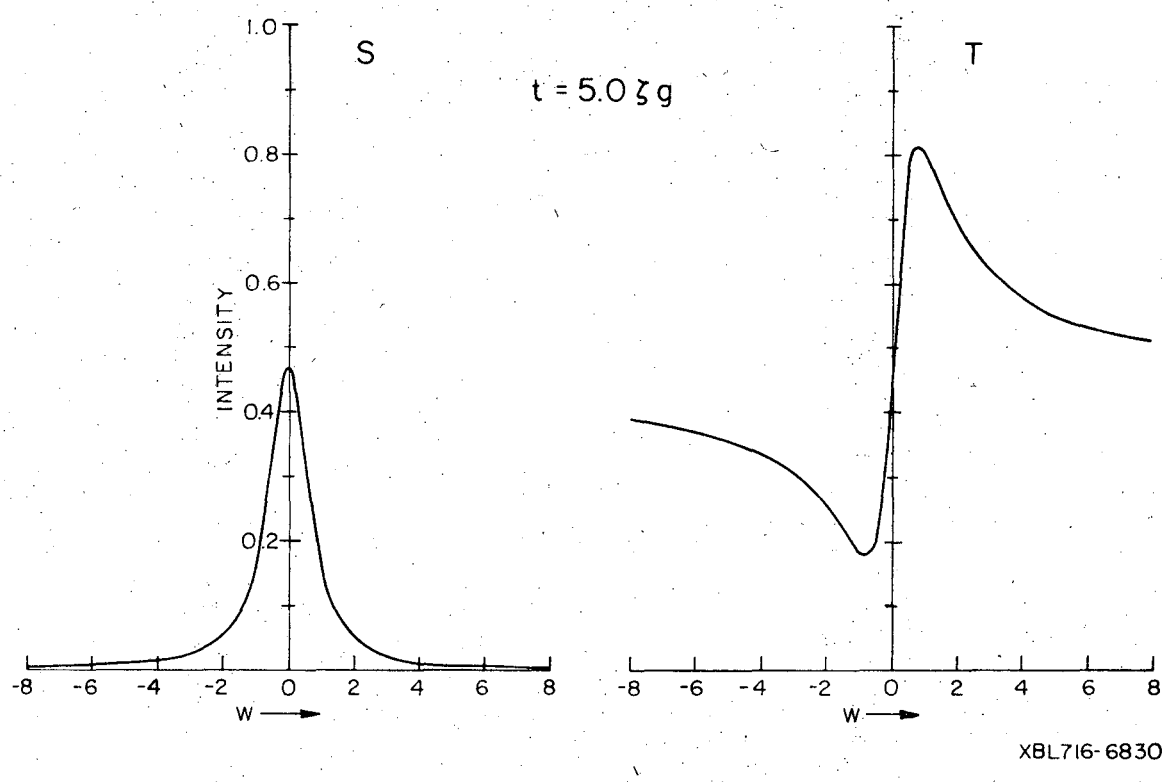

Fig.II. 5d

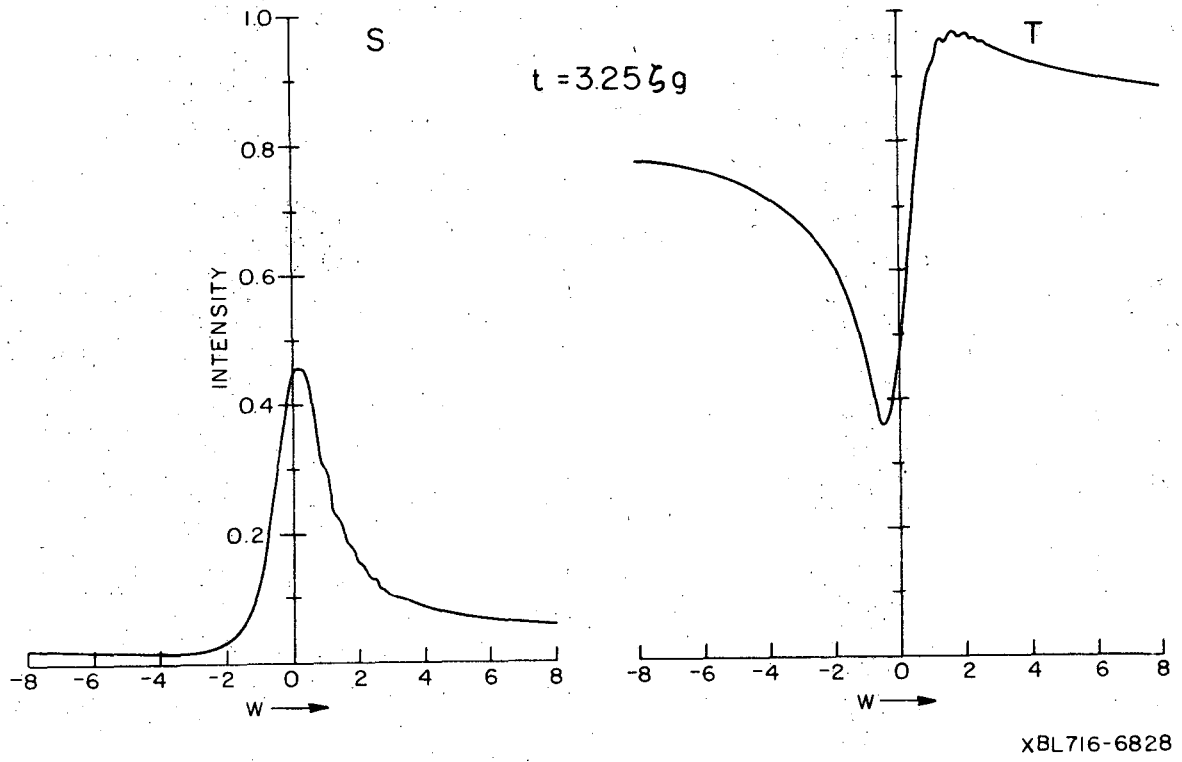

Fig.II. 5e

Kikuchi line pairs computed for various specimen thicknesses, (a) - (d). Considerable amount of asymmetry is introduced into the pattern if $f^{ig}_{oo}/f^{io}_{oo} \neq 0$, as in (e). Parameters used ($\frac{\pi \xi_g}{\xi'_{io}} = \frac{\pi \xi_g}{\xi'_{io}} = 0.3$ and $\frac{\pi \xi_g}{\xi'_{og}} = \frac{\pi \xi_g}{\xi'_{ig}} = 0.225$) corresponds approximately to that of a (111) Si diffraction. The Kikuchi line pairs are observed in any diffraction pattern.

The only participating absorption parameter is $\mu_{oo}^2 = \frac{1}{\xi'_{oo}}$. The geometry of this case is that a transmitted Bragg spot lies where the trace of the operating planes should be, and parallel to the diffracting planes, the Kikuchi pattern occurs in a symmetrical intensity distribution about the only Bragg spot. Because of this symmetry, the scattering factors in this case, f_{oo}^{io} and f_{oo}^{ig}, for the small region in the reciprocal space considered, may be taken as being equal to each other.

The equation of $I_{io}(\omega_i)$ in this case is identical to Eq. (II.27a). However, the condition that $f_{oo}^{io} = f_{oo}^{ig}$ now yields from Eq. (II.27b) that $I_{ig}(\omega_i) = I_{io}(-\omega_i)$, indicating that the Kikuchi pattern is symmetric about the trace of the diffracting planes and is indeed a band structure. The experimental fact that the Kikuchi band changes from an excess in electrons to a deficiency in electrons with an increase in crystal thickness or a decrease in the incident electron beam voltage may be interpreted from the intensity equations in an elementary way. Consider $I_{io}(\omega_i)$, by letting $f_{oo}^{io} = f_{oo}^{ig} = f$, $\frac{1}{\xi'_{oo}} = \frac{1}{\xi'_{io}}$, $T = t/\xi_g$, Eq. (II.27a) is reduced to

$$
\begin{aligned}
I_{io}(\omega_i) = \left(\frac{\alpha}{\xi_g}\right)^2 \frac{\xi_g f}{2} e^{-2\pi \xi_g T/\xi'_{oo}} \Big\{ & \left(C_{io}^1 + C_{ig}^1\right)^2 \left(e^{2\pi \xi_g T/\xi'_{ig}\sqrt{1+\omega_i^2}} - 1\right)\sqrt{1+\omega_i^2} \\
& + \left(C_{io}^2 + C_{ig}^2\right)^2 \left(1 - e^{-2\pi \xi_g T/\xi'_{ig}\sqrt{1+\omega_i^2}}\right)\sqrt{1+\omega_i^2} \\
& + \frac{2\left(C_{io}^1 + C_{ig}^1\right)\left(C_{io}^2 + C_{ig}^2\right)}{\sqrt{1+\omega_i^2}} \frac{\xi_g}{\xi'_{ig}} \sin 2\pi\sqrt{1+\omega_i^2}\, T \Big\} .
\end{aligned}
\qquad \text{(II.28)}
$$

When the crystal is thin, the second term in the curly bracket on the right hand side of Eq. (II.28) dominates, and the band is an excessive one; for thick crystals, however, the first term donimates and the band is a deficient one. Intensity profiles calculated from Eq. (II.27) for several crystal thicknesses are shown in Fig. II.6. It can be clearly seen from this figure that the band may be very pronounced and that the change from a very high intensity on one side of the Bragg position to a very low intensity on the other side of the Bragg position occurs within a very small region of the reciprocal space. Furthermore, it is also worth mentioning that, regardless of whether the band is excessive or deficient, there exists, in the immediate vicinity of the Bragg position, an intensity maximum accompanied by an intensity minimum on the other side of the Bragg position. This is another well observed phenomenon which was not explained in the previous theories.

3. Dynamical Two-Beam Case--Kikuchi Line Contrast Reversal and Spacing Variations

Of all the two-beam (inelastic electrons) cases, this is by far the most complicated and interesting case. The Kikuchi pattern in this case exhibits several distinct behaviors, depending on the operating rel-vector and specimen thickness. Because in this case the two elastic beams satisfy or nearly satisfy the Bragg condition exactly, each of the four waves contribute to the generation of inelastic electrons significantly. Due to the presence of anomalous absorption, the two types of waves in each beam do not contribute equally to the generation of the inelastic electrons. Therefore, to a first approximation, α_j in Eq. (II.17) may be set proportional to the absorption parameter of the wave, i.e.,

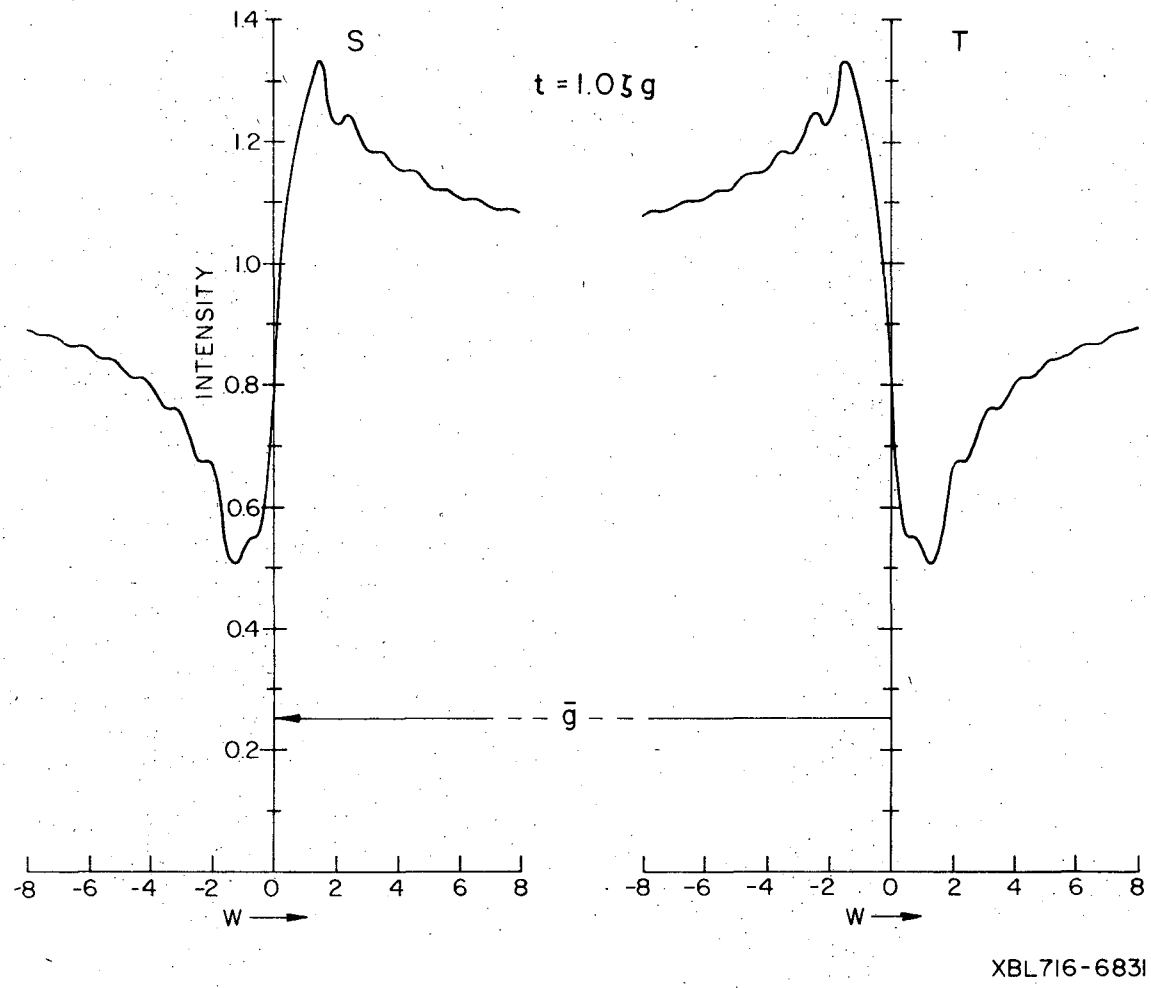
S
T
t = 1.05g
INTENSITY
1.4
1.2
1.0
0.8
0.6
0.4
0.2
ḡ
-8 -6 -4 -2 0 2 4 6 8
W
XBL716-6831

Fig.II. 6a

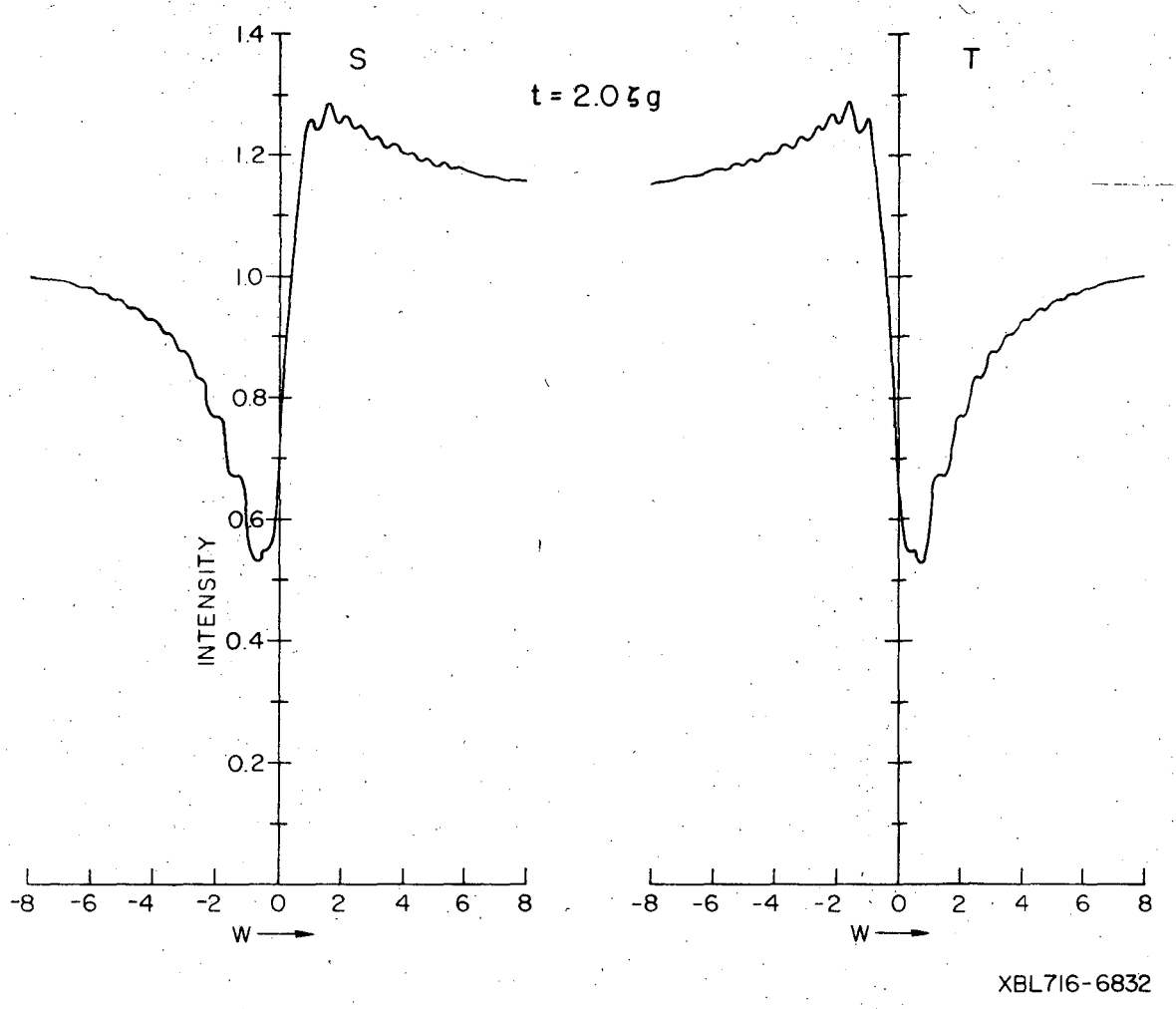
S
T
t = 2.0 ζg
INTENSITY
1.4
1.2
1.0
0.8
0.6
0.4
0.2
-8 -6 -4 -2 0 2 4 6 8
W
XBL716-6832

Fig.II. 6b

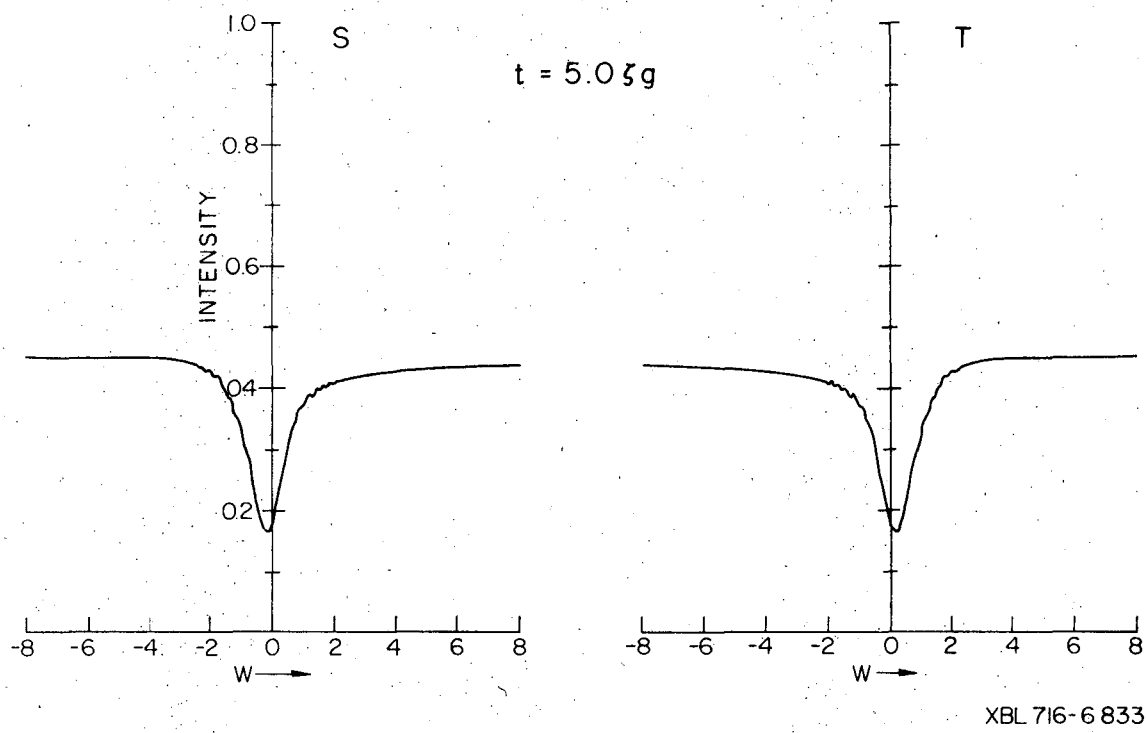

Fig.II. 6c

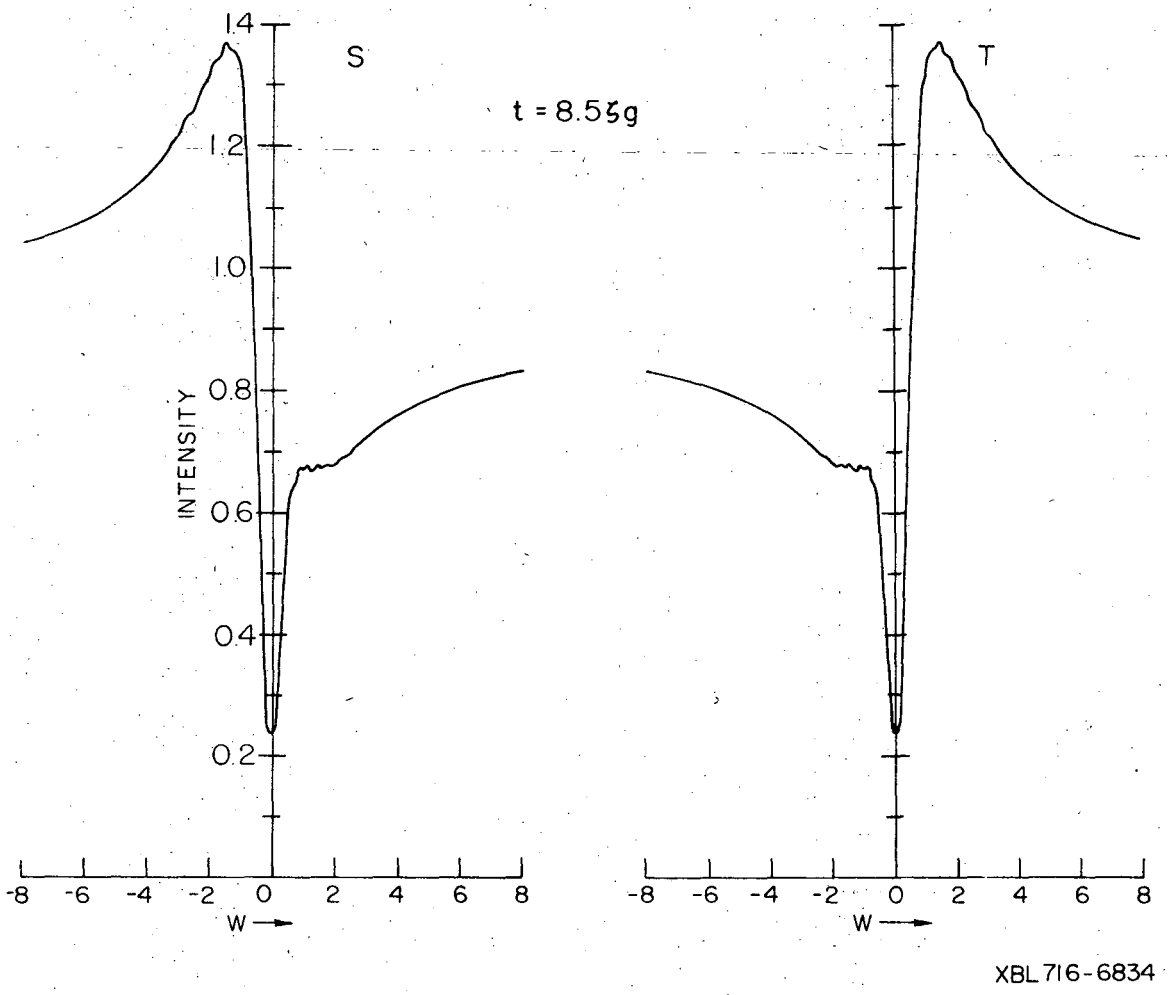
S
T
t = 8.5ζg
INTENSITY
1.4
1.2
1.0
0.8
0.6
0.4
0.2
-8 -6 -4 -2 0 2 4 6 8
W
XBL 716-6834

Fig.II. 6d

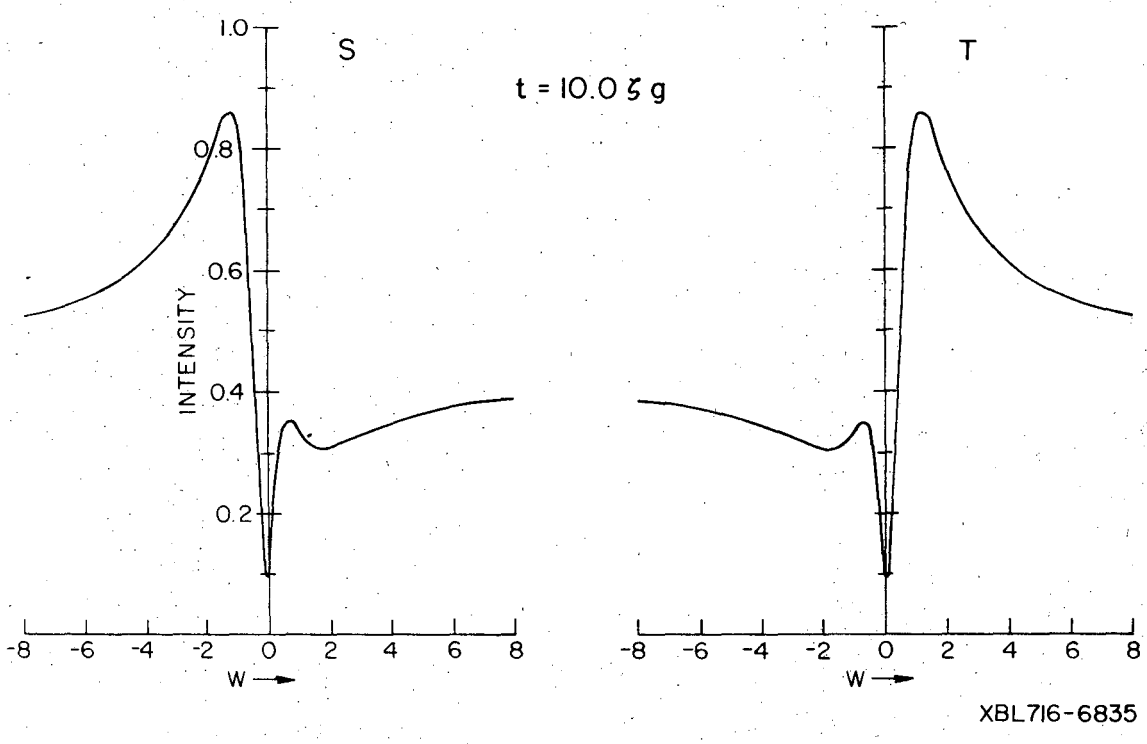

Fig.II. 6e

Behavior of Kikuchi band: the band changes from excessive to deficient with increasing specimen thickness. Parameters used for (111) Si.

$\alpha_1 = \alpha_c \mu_c' = \alpha_c \left(\frac{1}{\xi_{cc}'} - \frac{1}{\xi_{cg}' \sqrt{1+w_c^2}} \right)$ and $\alpha_2 = \alpha_c \mu_c^2$

$= \alpha_c \left(\frac{1}{\xi_{cc}'} + \frac{1}{\xi_{cg}' \sqrt{1+w_c^2}} \right)$. The intensities of the Kikuchi

Pattern is now given by

$$I_{ic}(T) = \frac{a^2}{2\pi(\mu_c' - \mu_i')} \left[e^{-2\pi \mu_i' \xi_g T} - e^{-2\pi \mu_c' \xi_g T} \right]$$

$$+ \frac{b^2}{2\pi(\mu_c^2 - \mu_i^2)} \left[e^{-2\pi \mu_i^2 \xi_g T} - e^{-2\pi \mu_c^2 \xi_g T} \right]$$

$$+ \frac{c^2}{2\pi(\mu_c' - \mu_i^2)} \left[e^{-2\pi \mu_i^2 \xi_g T} - e^{-2\pi \mu_c' \xi_g T} \right]$$

$$+ \frac{d^2}{2\pi(\mu_c^2 - \mu_i')} \left[e^{-2\pi \mu_i' \xi_g T} - e^{-2\pi \mu_c^2 \xi_g T} \right]$$

$$+ \frac{2ab}{\pi(\mu_c' + \mu_c^2 - \mu_i' - \mu_i^2)} \left[e^{-\pi(\mu_i' + \mu_i^2)\xi_g T} - e^{-\pi(\mu_c' + \mu_c^2)\xi_g T} \right] \cos 2\pi \Delta k \xi_g T$$

$$+ \frac{ac}{\pi\left[\frac{1}{2}(\mu_i' + \mu_i^2) - \mu_c\right]^2 + (\pi \Delta k T)^2}$$

$$\times \left\{ \pi \left[\mu_c' - \frac{1}{2}(\mu_i' + \mu_i^2) \right] \left[e^{-\pi(\mu_i' + \mu_i^2)\xi_g T} - e^{-2\pi \mu_c' \xi_g T} \right] \cos 2\pi \Delta k \xi_g T \right.$$

$$\left. + \pi \Delta k T \left[e^{-\pi(\mu_i' + \mu_i^2)\xi_g T} - e^{-2\pi \mu_c' \xi_g T} \right] \sin 2\pi \Delta k \xi_g T \right\}$$

$$+ \frac{a\,d}{\pi^2\left[\frac{1}{2}(\mu_o^1+\mu_o^2)-\mu_i^1\right]^2+(\pi\Delta kT)^2}$$

$$\times\left\{\pi\left[\tfrac{1}{2}(\mu_o^1+\mu_o^2)-\mu_i^1\right]\left[e^{-2\pi\mu_i^1\xi_g T}-e^{-\pi(\mu_o^1+\mu_o^2)\xi_g T}\cos 2\pi\Delta k\xi_g T\right]\right.$$

$$\left.+\pi\Delta kT\,e^{-\pi(\mu_o^1+\mu_o^2)\xi_g T}\sin 2\pi\Delta k\xi_g T\right\}$$

$$+ \frac{b\,c}{\pi^2\left[\frac{1}{2}(\mu_o^1+\mu_o^2)-\mu_i^2\right]^2+(\pi\Delta kT)^2}$$

$$\times\left\{\pi\left[\tfrac{1}{2}(\mu_o^1+\mu_o^2)-\mu_i^2\right]\left[e^{-2\pi\mu_i^2\xi_g T}-e^{-\pi(\mu_o^1+\mu_o^2)\xi_g T}\cos 2\pi\Delta k\xi_g T\right]\right.$$

$$\left.+\pi\Delta kT\,e^{-\pi(\mu_o^1+\mu_o^2)\xi_g T}\sin 2\pi\Delta k\xi_g T\right\}$$

$$+ \frac{b\,d}{\pi^2\left[\mu_o^2-\frac{1}{2}(\mu_i^1+\mu_i^2)\right]^2+(\pi\Delta kT)^2}$$

$$\times\left\{\pi\left[\mu_o^2-\tfrac{1}{2}(\mu_i^1+\mu_i^2)\right]\left[e^{-2\pi\mu_o^2\xi_g T}-e^{-\pi(\mu_i^1+\mu_i^2)\xi_g T}\cos 2\pi\Delta k\xi_g T\right]\right.$$

$$\left.+\pi\Delta kT\,e^{-\pi(\mu_i^1+\mu_i^2)\xi_g T}\sin 2\pi\Delta k\xi_g T\right\}$$

$$+ \frac{c\,d}{\pi^2\left[\frac{1}{2}(\mu_o^1+\mu_o^2)-\frac{1}{2}(\mu_i^1+\mu_i^2)\right]^2+(2\pi\Delta kT)^2}$$

$$\times\left\{\tfrac{\pi}{2}(\mu_o^1+\mu_o^2-\mu_i^1-\mu_i^2)\left[e^{-\pi(\mu_i^1+\mu_i^2)\xi_g T}-e^{-\pi(\mu_o^1+\mu_o^2)\xi_g T}\right]\cos 2\pi\Delta k\xi_g T\right.$$

$$\left.+2\pi\Delta kT\left[e^{-\pi(\mu_i^1+\mu_i^2)\xi_g T}+e^{-\pi(\mu_o^1+\mu_o^2)\xi_g T}\right]\sin 2\pi\Delta k\xi_g T\right\},$$

(II.29a)

where $T = t/\xi_g$,

$\Delta k = -\sqrt{1+w_i^2}/\xi_g$

and

$$a = \pi \alpha_0 \xi_g \mu_0^1 \left\{ \left(f_{00}^{i0} c_{00}^1 + f_{0g}^{i0} c_{0g}^1 \right) c_{i0}^1 + \left(f_{00}^{ig} c_{00}^1 + f_{0g}^{ig} c_{0g}^1 \right) c_{ig}^1 \right\} ,$$

$$b = \pi \alpha_0 \xi_g \mu_0^2 \left\{ \left(f_{00}^{i0} c_{00}^2 + f_{0g}^{i0} c_{0g}^2 \right) c_{i0}^2 + \left(f_{00}^{ig} c_{00}^2 + f_{0g}^{ig} c_{0g}^2 \right) c_{ig}^2 \right\} ,$$

$$c = \pi \alpha_0 \xi_g \mu_0^1 \left\{ \left(f_{00}^{i0} c_{00}^1 + f_{0g}^{i0} c_{0g}^1 \right) c_{i0}^2 + \left(f_{00}^{ig} c_{00}^1 + f_{0g}^{ig} c_{0g}^1 \right) c_{ig}^2 \right\} ,$$

$$d = \pi \alpha_0 \xi_g \mu_0^2 \left\{ \left(f_{00}^{i0} c_{00}^2 + f_{0g}^{i0} c_{0g}^2 \right) c_{i0}^1 + \left(f_{00}^{ig} c_{00}^2 + f_{0g}^{ig} c_{0g}^2 \right) c_{ig}^1 \right\} ,$$

and an identical expression for $I_{ig}(T)$, provided the substitutions given in Eq. (II.27) is again used. Contrary to cases (II.E.1) and (II.E.2), the various oscillating terms in Eq. (II.29) may now contribute significantly. In all cases the presence of a band type structure and sub-fringes is unavoidable.

The Kikuchi line pair contrast reversal occurs for small rel-vector diffractions for which accurate allocation of exact Bragg condition may be easily achieved. This situation may be seen most easily by letting only the mean absorption parameter of the elastic beams be present in Eq. (II.29). In such circumstances $I_{io}(t)$ has a minimum and $I_{ig}(t)$ has a maximum at $W_i = 0$ for t equal to any odd multiples of $\xi_g/2$ and the situation reverses for t equal to any integer multiples of ξ_g (except when t is equal to 0), i.e., the Kikuchi line pair reverses its contrast at intervals of $\xi_g/2$. When all absorption parameters are considered, the above discussions remain approximately true. However, it should be mentioned that this reversal is primarily due to the oscillating terms in Eq. (II.29), which are functions of the specimen thickness, thus it can be expected that this phenomenon may also be observed at thicknesses other than the extreme situations mentioned above. In practice, non-uniformity in specimen thickness, local bending of specimen, etc., will also effect the experimental results. The computed profiles demonstrating this effect are shown in Fig. II.7.

In the case of large rel-vectors, notice the fact that the length of the operating reciprocal lattice vector is large and accurate allocation of the exact Bragg conditions become very improbable, thus the incident elastic electron beam could be considered to satisfy the Bragg conditions

not exactly. For such a case, using the value $W_o = 1$, the Kikuchi pattern intensity distributions computed from Eq. (II.20) is given in Fig. II.8. It is seen from these computed intensity curves that the Kikuchi line spacing in this case varies as a function of specimen thickness, i.e., the Kikuchi line spacing varies from larger to smaller than that of the Bragg angle. To some extent, this effect also depends on the various oscillating terms in Eq. (II.29). This effect may be compared to the so-called size effect of the many beam problem of elastic electrons.

4. A Many-Beam Problem

To study the behavior of the Kikuchi pattern in a more general case, multiple elastic and inelastic beam interactions must be considered, particularly if the incident electron energy is high. Without going into such calculations in this study, we will now use the special property given by Eq. (II.23) to show that the method of summing up the rocking curve intensities to calculate the Kikuchi patterns in the systematic many beam cases may be derived from our theory. In order to avoid the complexity of calculations, Thomas and Humphreys[36] proposed, without proof, that along a systematic row of excitations, the intensity distributions of the Kikuchi pattern may be computed by simply summing up all rocking curve intensities of each participating reflection at every deviation, $\bar{k}_{ix}$. In their computations absorption of the inelastic electrons are considered and the results obtained are generally in good agreements with experimental observations.

Consider a systematic many beam case, by virtue of Eq. (II.23), we need only to calculate $\psi_{io}(\bar{k}_{ix})$ for all values of $\bar{k}_{ix}$. Assume now that the crystal is very thick, and all excited elastic beams attenuate

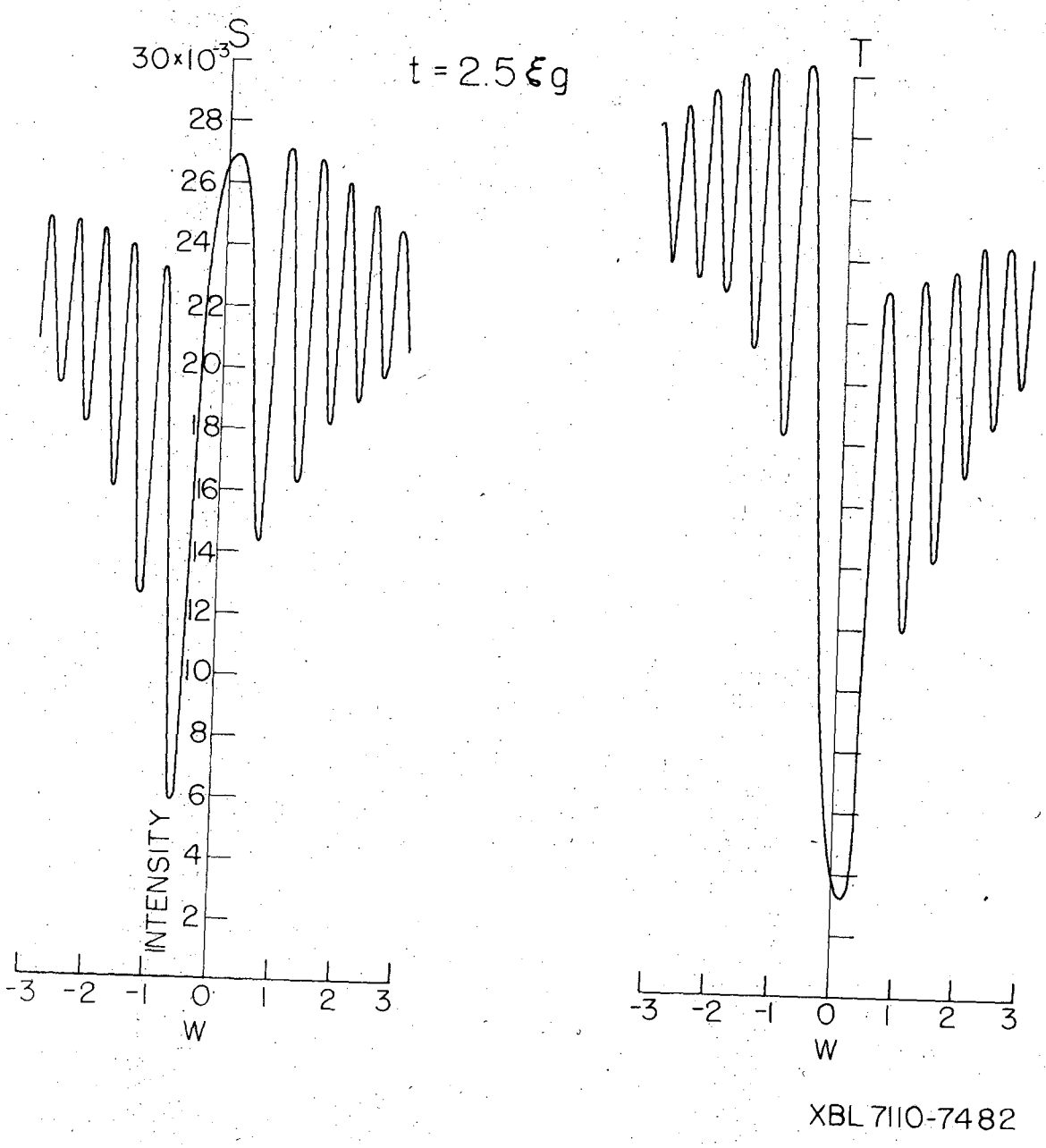

XBL 7110-7482

Fig.II. 7a

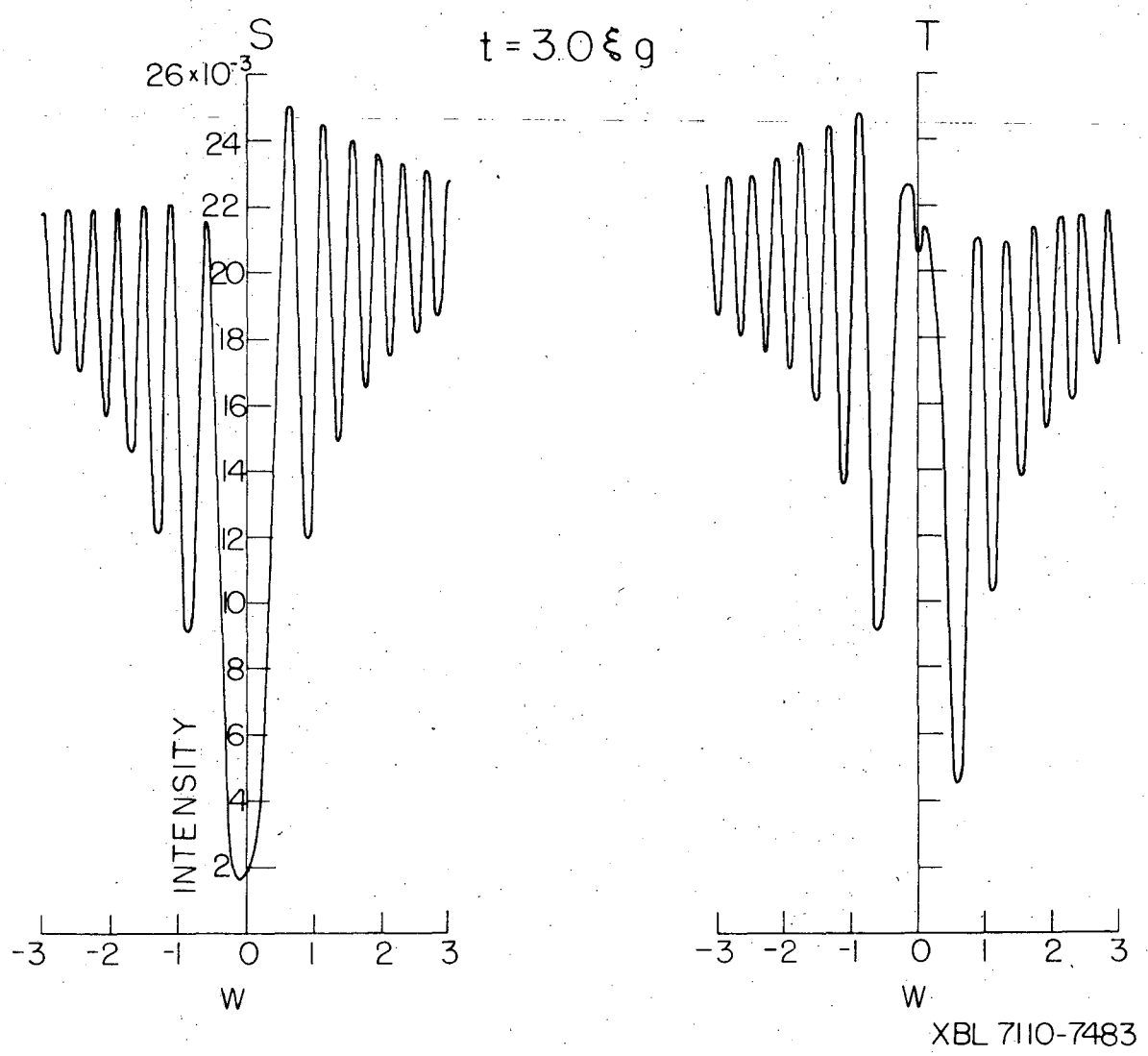

Fig.II. 7b

Kikuchi line contrast reversal at the vicinity of $W_i = 0$. (a). Normal contrast (black-and-white) for t equal to odd multiples of $\xi_g/2$. (b). Reversed contrast for t equal to multiples of ξ_g. If $W_o \cong 0$ is not satisfied, contrast reversal may occur at other specimen thicknesses.

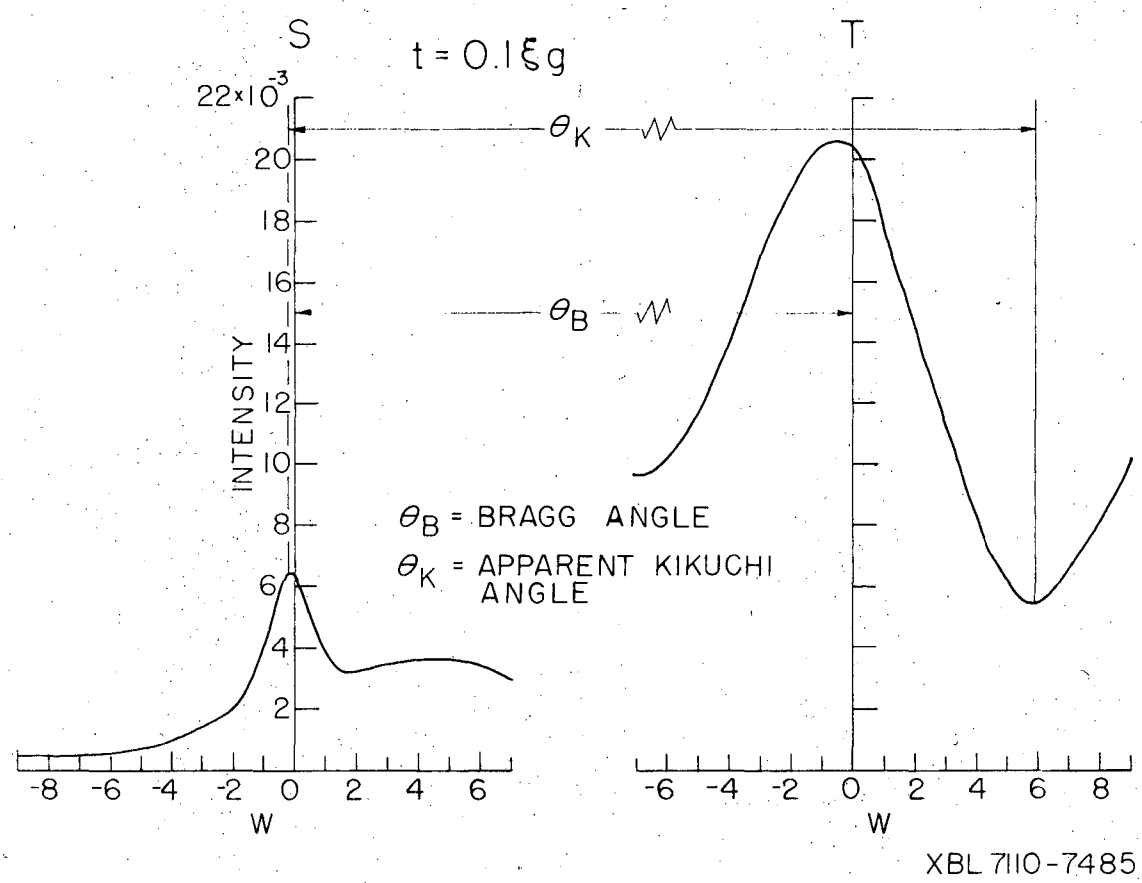
S
t = 0.1ξg
T
22×10⁻³
20
18
16
14
12
10
8
6
4
2
INTENSITY
θK
θB
θB = BRAGG ANGLE
θK = APPARENT KIKUCHI ANGLE
-8 -6 -4 -2 0 2 4 6
W
-6 -4 -2 0 2 4 6 8
W
XBL 7110-7485

Fig.II. 8a

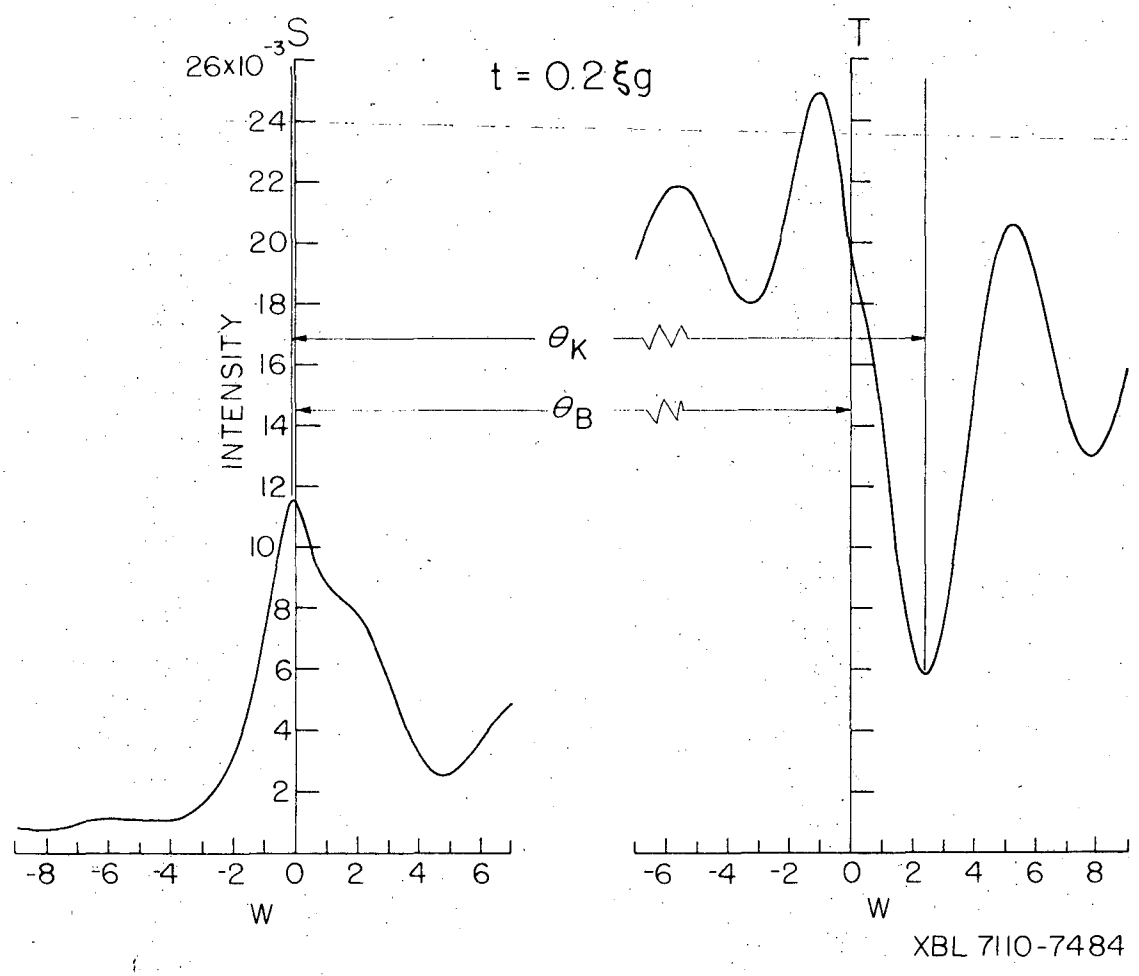
S
T
26x10^-3
t = 0.2 ξg
INTENSITY
24
22
20
18
16
14
12
10
8
6
4
2
θK
θB
-8 -6 -4 -2 0 2 4 6
W
-6 -4 -2 0 2 4 6 8
W
XBL 7110-7484

Fig.II. 8b

0 0 0 0 3 7 0 0 0 5 5

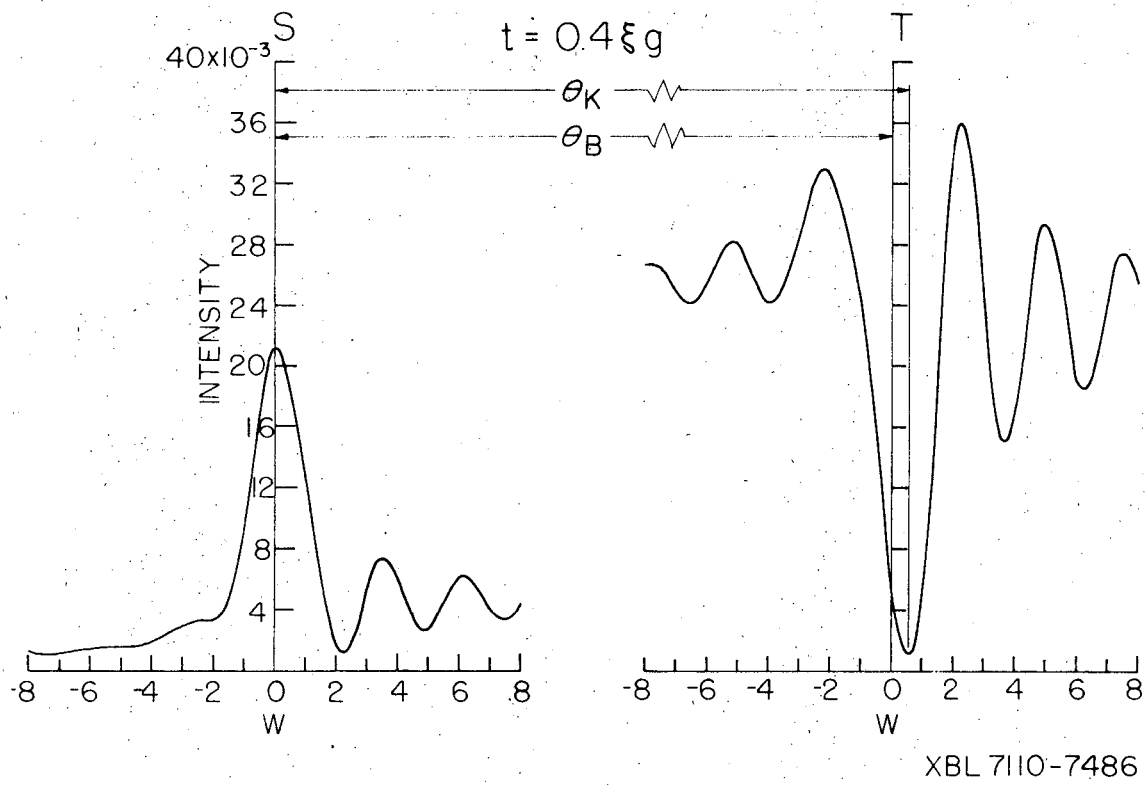

Fig.II. 8c

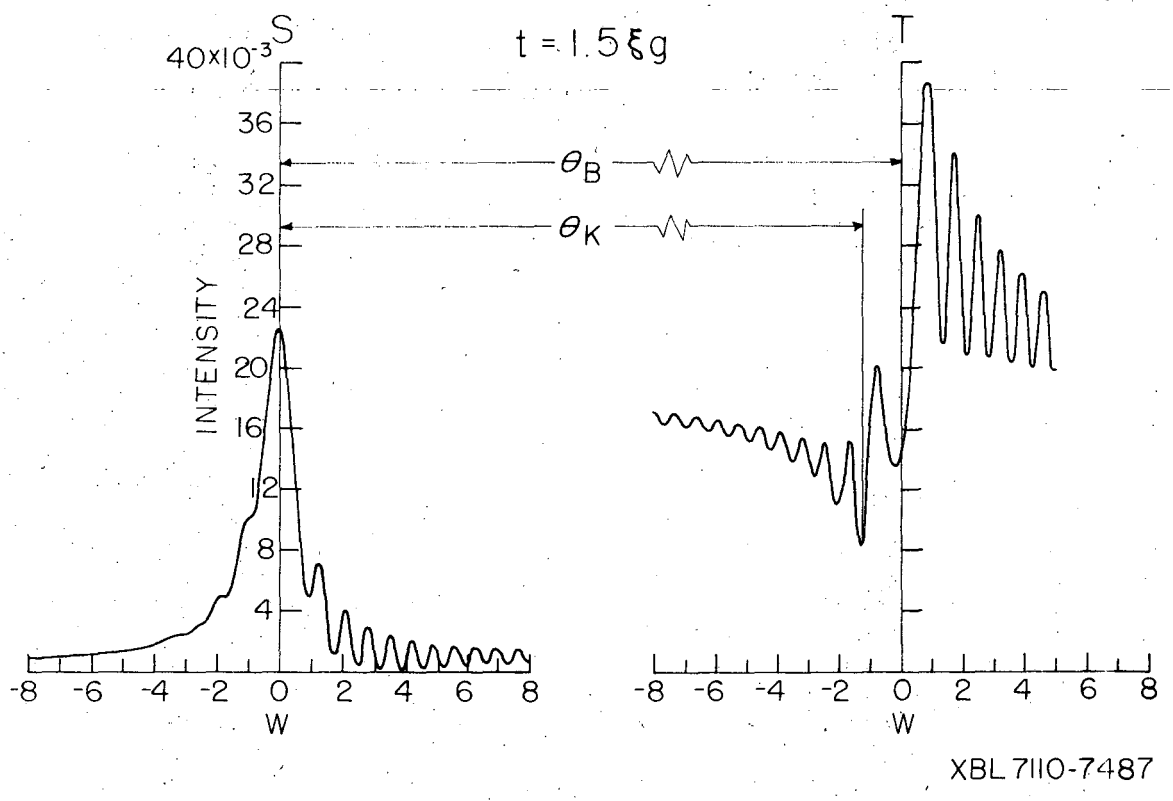
S
T
t = 1.5 ξg
40×10⁻³
36
32
28
24
20
16
12
8
4
INTENSITY
θB
θK
-8 -6 -4 -2 0 2 4 6 8
W
-8 -6 -4 -2 0 2 4 6 8
W
XBL 7110-7487

Fig.II. 8d

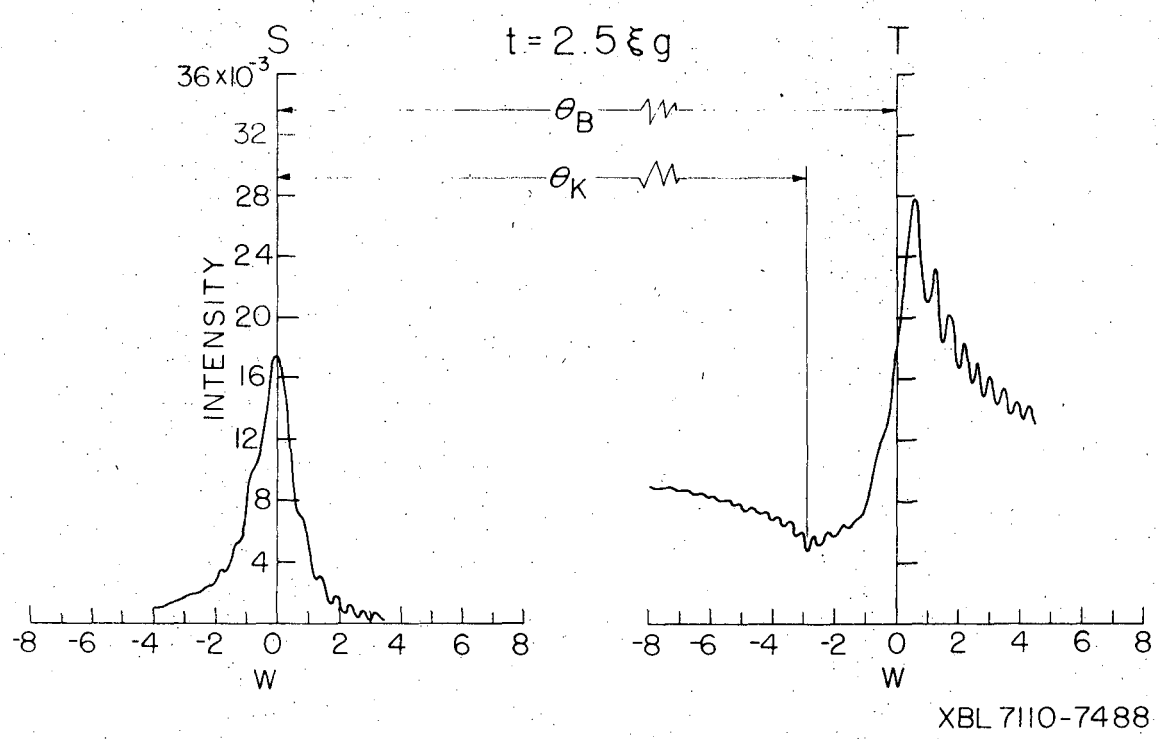
S
t = 2.5 ξg
T
36x10^-3
32
28
24
20
16
12
8
4
INTENSITY
θB
θK
-8 -6 -4 -2 0 2 4 6 8
W
-8 -6 -4 -2 0 2 4 6 8
W
XBL 7110-7488

Fig.II. 8e

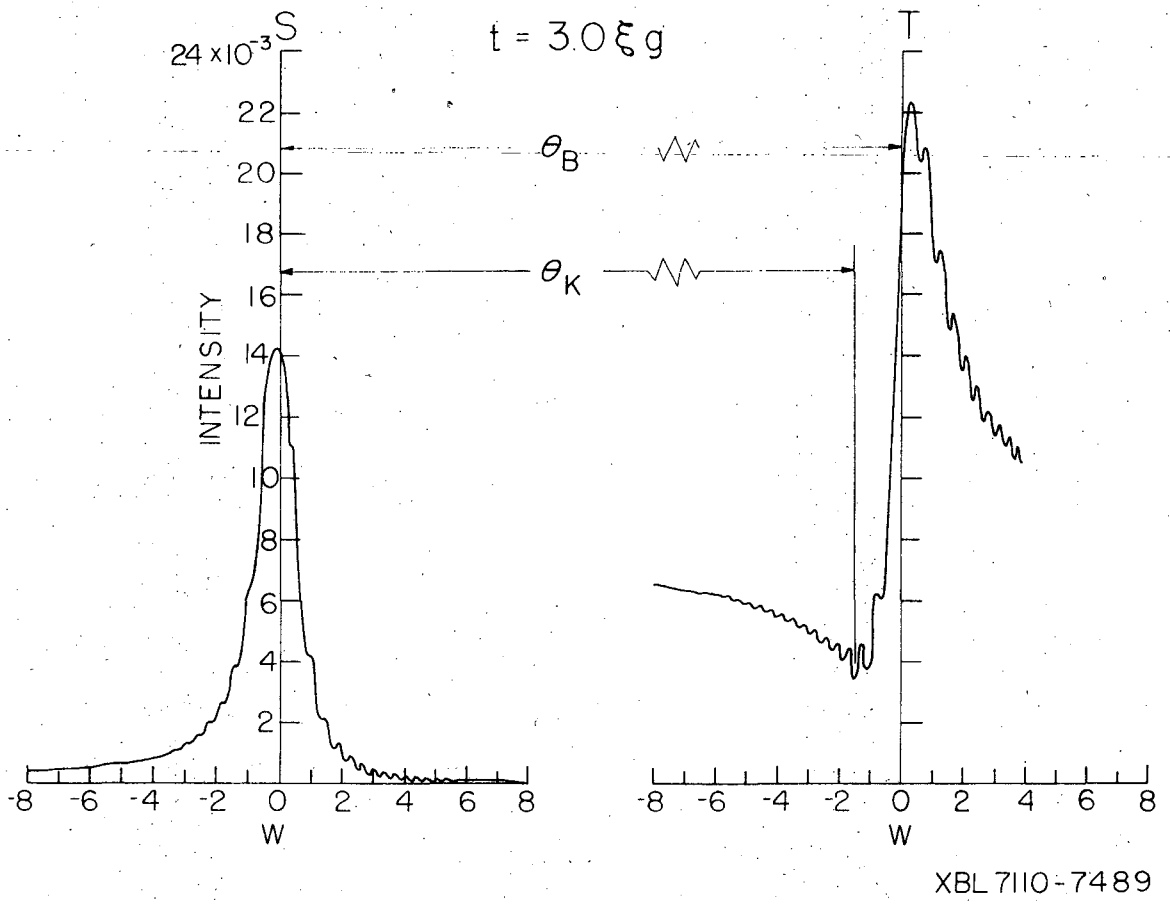

Fig.II. 8f

Kikuchi line spacing variations with specimen thickness.

Parameters used ($\frac{\pi \xi_g}{\xi'_{oi}} = \frac{\pi \xi_g}{\xi'_{io}} = 1.0$ and $\frac{\pi \xi_g}{\xi'_{og}} = \frac{\pi \xi_g}{\xi'_{ig}}$ = 0.7) corresponds to approximately that for (511) Si. $W_o = 1.0$.

rapidly in the crystal, hence all inelastic electrons may be viewed as generated at the top surface of the crystal. Under this approximation, we may write

$$\psi_{ic}(\bar{k}_{ix}) = \int_0^t \left[\cdots \quad \psi_{-g}(\bar{k}_{ix}, t-z) \quad \psi_c(\bar{k}_{ix}, t-z) \quad \psi_g(\bar{k}_{ix}, t-z) \cdots \right]$$

$$\times \begin{bmatrix} \vdots & \vdots & \vdots & \\ \cdots f^{i(-g)}_{c(-g)} & f^{i(-g)}_{cc} & f^{i(-g)}_{cg} & \cdots \\ \cdots f^{ic}_{c(-g)} & f^{ic}_{cc} & f^{ic}_{cg} & \cdots \\ \cdots f^{ig}_{c(-g)} & f^{ig}_{cc} & f^{ig}_{cg} & \cdots \\ \vdots & \vdots & \vdots & \end{bmatrix} \begin{bmatrix} \vdots \\ \psi'_{c(-g)} = \delta(c)\alpha_{-g} \\ \psi'_{cc} = \delta(c)\alpha_0 \\ \psi'_{cg} = \delta(c)\alpha_g \\ \vdots \end{bmatrix}$$

$$= \sum_g F_g \psi_g(\bar{k}_{ix}, t),$$

(II.30)

where $\psi_g(\bar{k}_{ix},t)$ is just the wave function of the gth beam in the ordinary dynamical calculations (see Eq. (A.13d)). The total intensity at a deviation $\bar{k}_{ix}$ is then

$$I_{ic}(\bar{k}_{ix}, t) = \left| \sum_g F_g \psi_g(\bar{k}_{ix}, t) \right|^2.$$

If we further neglect the interaction terms between each $\psi_g(\bar{k}_{ix},t)$, we have

$$I_{ic}(\bar{k}_{ix}, t) = \sum_g |F_g \psi_g(\bar{k}_{ix}, t)|^2, \qquad \text{(II.31)}$$

where F_g is a function of $|\bar{k}_{ix}|$. Eq. (II.31) reveals that the Kikuchi intensity is simply given by the weighted sum of the rocking curve intensities. The last assumption, i.e., the ignorance of any interaction terms between the wave functions $\psi_g(\bar{k}_{ix},t)$, is justified only if the result obtained from Eq. (II.31) is considered to be the averaged intensity over a range of crystal thickness variations which is larger than the periods of all the neglected interaction terms.

F. Images Due to Kikuchi Electrons and Other Inelastic Electrons

In recent years a considerable amount of interest has been paid to high resolution microscopy aimed at improving the resolving power of microscopes to the atomic limit. During the course of such works for crystals containing defects, image enhancement techniques become important. There are many methods to accomplish such tasks, for example, the digital computer with its associated video scanning equipment can be used in conjunction with the microscope's best performance to give improved resolution.[37] This type of technique originated from the necessity of image enhancement of space photography, and a result of working on mainly television images. The technique involves operations of, geometric correction, photometric correction, random noise removal, periodic noise removal, and modulation transfer function corrections (compensation for attenuation of spatial high frequency components).

In electron micrographs for images of a periodic nature (e.g., Moiré fringes), the signal to noise ratio can be improved by translating and superimposing the image upon itself. In the case of images of defects (e.g., dislocations, stacking faults, and small particulate defects), however, situations can be quite different. The random noise in any

typical micrograph due to mishandling of the microscope, i.e., poor alignment,improper focusing and exposure of the plates, etc., may be largely avoided by improving operational techniques of the microscope. In this case, the random noise removal technique may also be applied to improve the quality of the micrograph. A more important and predominant class of noise is, however, the images produced by inelastic electrons. Since inelastic scattering must occur in any electron diffraction experiment of crystals, the images produced by inelastic electrons are an unavoidable characteristic noise of both the crystal and the defects. In comparison to images produced by elastic electrons, these images are of somewhat weaker but nevertheless not negligible intensities. These images generally differ from images produced by elastic electrons in the following aspects: (1) Image positions are shifted; (2) More spatial frequency components may be present; (3) Image width is much broader. It should be noticed that although the inelastic electrons generated by plasmon excitations and inner shell electron excitations may be removed by an energy selecting microscope, a majority of these electrons, which suffered an energy loss of typically less than a few hundredth of one ev, due to phonon excitations, are nevertheless out of the scope of any energy selecting scheme. Thus, when recorded on the photoplate, these characteristic noise images superimpose with the images produced by elastic electrons and could lead to erroneous interpretation of the micrograph. For example, they may smear the images of closely spaced defects, e.g., those of a dislocation dipole, a super dislocation, dissociated partial dislocations, closely spaced small particles. If these noise images are intense enough, i.e., for the case of a crystal which is not

too thin, they may also lead to wrong estimations of defect densities since these images may appear to be spatially separated enough from images of elastic electrons and may also introduce more spatial frequency components to the image of a single defect.

The desirability of removing this kind of characteristic noise is obvious. Experimentally this could be accomplished by essentially two micrographs; one consisting of images from both elastic and inelastic electrons, the other consisting of images from inelastic electrons only, and is done by moving the aparture to enclose a portion of the Kikuchi line or just the diffuse backgrounds surrounding the Bragg spot. These two micrographs could then be digitalized and subtracted to allow a new micrograph free from these noise images to be constructed. It should be noticed, however, that due either to translation of the aparture or gun tilting, the latter micrograph of inelastic electrons are taken from a slightly different diffraction condition. A first correction could be made by using the averaged data from more than one micrographs of this kind taken from mutually compensating orientations relative to the elastic beam.

Theoretical calculations of the image profiles due to Kikuchi electrons and other inelastic electrons are readily obtainable for the general n-beam case by using Eq. (II.24). The two-beam results obtained for Kikuchi electron intensity distributions in Section II.6 readily yield the extinction contour due to these electrons for a wedge shaped foil. This result is shown in Fig. II.9.

Careful examinations of Eq. (II.24) when applied to image problems show that there are two kinds of mechanisms responsible for images being

produced by inelastic electrons: (1) Information about images produced by inelastic electrons, i.e., the responsible electrons become inelastic before reaching the displacement fields produced by the defect and then produce images upon traveling through or across these displacements. (2) Images formed by elastic electrons upon traveling through or across the displacement fields due to the defect, but these electrons subsequently suffered from inelastic scattering and the image information is thus carried over to the newly generated inelastic electrons. The above discussed image forming process for images due to inelastic electrons can be best visualized with a discrete boundary type of defect, e.g., a stacking fault. Of course, the total image due to inelastic electrons is none the less a superposition of images due to both of these mechanisms. Therefore, it is not surprising that the images produced by inelastic electrons is natually fuzzier than that due to elastic electrons, i.e., a broader width, more spatial frequency components, shifting of image positions, etc.

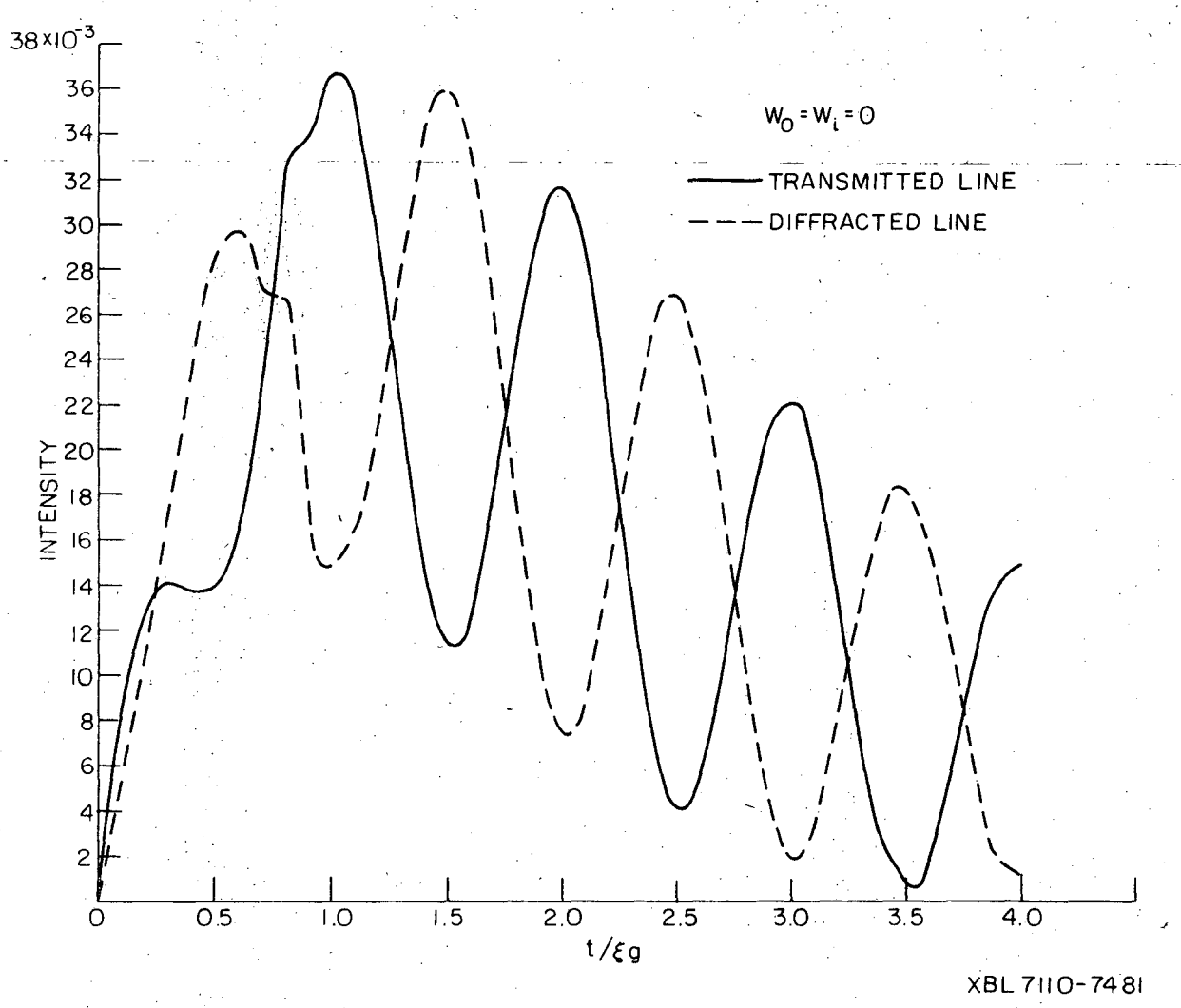

Fig.II. 9

Computed extinction contours due to Kikuchi electrons for the case $W_o = W_i = 0$. This curve also illustrates the contrast reversal of Kikuchi line pairs.

III. AN ENERGY ANALYZING MICROSCOPE

A. Introduction

Upon traveling through the crystal, certain types of characteristic excitations will unavoidably be generated by the electron beam; plasmons, inner shell electron excitations, phonons, etc. To generate these excitations, energy must be supplied by the electrons which then become inelastic. Appreciable amounts of momentum transfer usually accompany any inelastic scattering and therefore change the direction of propagation of the inelastic electrons. This momentum transfer, together with the fact that inelastic electrons lose coherency with the elastic electrons as well as with other inelastic electrons suffering the same amount of energy loss but being generated at different depths in the specimen, causes the obscuring of images and diffraction patterns, as well as the formation of Kikuchi patterns. From the view-point of obtaining better resolution, it is obviously desirable to remove these inelastic electrons. This leads to the development of the energy selecting microscope which uses a number of energy filters capable of producing an image or diffraction pattern free from certain kinds of inelastic electrons.[16-19] Inelastic electrons generated due to the excitation of a plasmon or the ionization of an inner shell electron have energy losses well over a few ev and can be successfully filtered out of the image and the diffraction pattern formed by the elastic beams. However, those inelastic electrons which are generated by excitations of phonons have energy losses typically under a fraction of one ev, and can not be filtered out.

Undesirable as they appear to be in image work, the inelastic electrons are not a total nuisance: they themselves carry information in the

form of energy distributions which are characteristic of the material under study. For this reason, energy analyzers can be fabricated. Upon passing through a narrow slit, the energy loss spectrum of the material may be displayed by the electrons. Both images and diffraction patterns may be examined in this manner and knowledge concerning the electronic structures of the materials studied can be obtained. This in turn can be used to measure the chemical constitution of microscopic regions of the specimen.[13,14] Therefore, measurements of the loss spectra of electrons in an electron microscope should provide a powerful method of microanalysis if reasonably high resolving power of the spectrometer could be achieved.

The resolving power of the electron spectrometer is defined as $E/\Delta E$, where E is electron beam voltage and ΔE is the voltage resolution. Several factors tend to limit the resolving power of a spectrometer. The first major limitation is imposed by the precision of electron optics and the stability of the high voltage supply. However, the stability of the high voltage supplies need not be critical if the electrons are slowed down before analysis. This can be done by electrodes connected to the high voltage source which supplies the microscope. The resolving power is also limited by the spread in energy of the electron beam from the thermionic gun and by thermal motion of electrons. The two latter factors are quantum statistical processes, and, if not counteracted by a monochrometer at the electron gun, would limit the resolution of the spectrometer to 1 to 1.5 ev.

B. Energy Analyzing Device--The Möllenstedt Lens System

A large number of devices suitable for energy analysis has been reported in the literature.[15] The main restrictions on the choice of devices are that the energy resolution should be of the order of 1 ev or less, and that they should be readily adaptable to the imaging system of the microscope. The devices commonly used which meet these requirements include the Möllenstedt lens (cylindrical electrostatic) system, the cylindrical magnetic lens and the electrostatic-mirror magnetic lens systems. The device we chose to use in our energy analyzing microscope is the Möllenstedt lens system. The reason for making this choice is twofold:

(1) The theoretical value of the energy resolution of this device, $\Delta E/E$, can reach (10^{-7}), it is doubtful that any other device can approach this value;

(2) Its design characteristics are well known.[39]

A cross-sectional view of this lens system is shown in Fig. III.1. A fine slit, a few microns wide and 1 cm long, serves as the electron entrance aperature. The slit is aligned with its long dimension parallel to the axes of the cylindrical electrodes. Electrons pass through the slit S into a box-shaped electrode system at the anode (ground) potential and then through regions of high chromatic aberrations near the two cylindrical electrodes biased at cathode potential. Figure III.2 shows schematically the potential distributions of the region near the two cylindrical electrodes. If the slit S is placed at a suitable off-axis position (Fig. III.3), electrons of different energies can be dispersed at the exit side of the lens system.

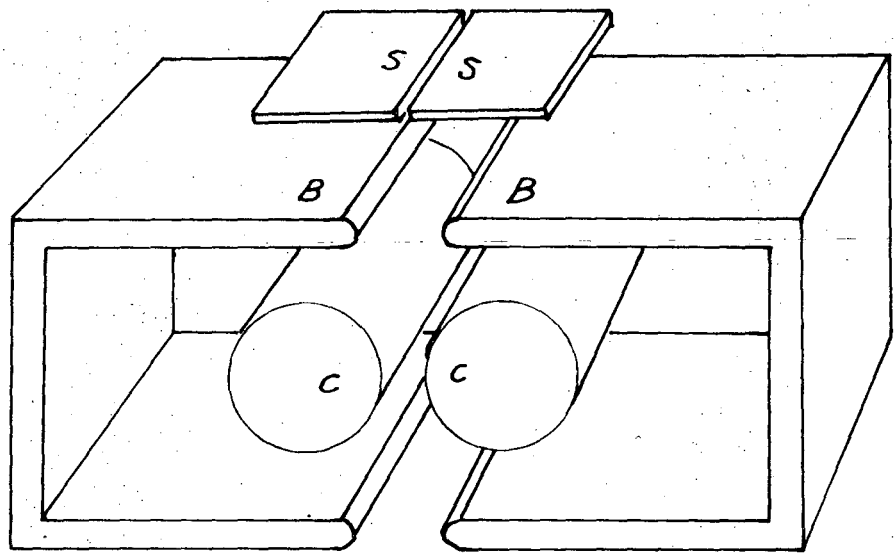

Fig. III.1 The cross-sectional view of the Möllenstedt lens system, where C is the cylindrical electrostatic lenses at cathode potnetial, B is the box-shaped electrodes at anode (ground) potential and S is the thin slit which serves as electron entrance aperature.

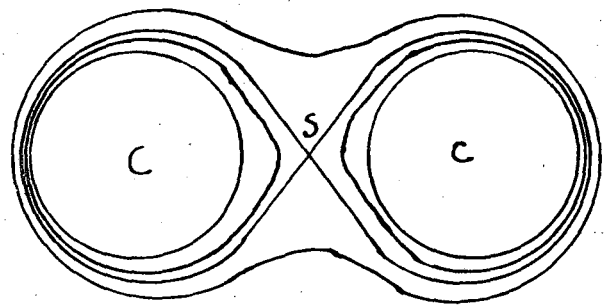

XBL 7111-7679

Fig. III.2 A cross-section of the cylindrical lenses showing the equal potnetial surfaces in the region of the saddle point S.

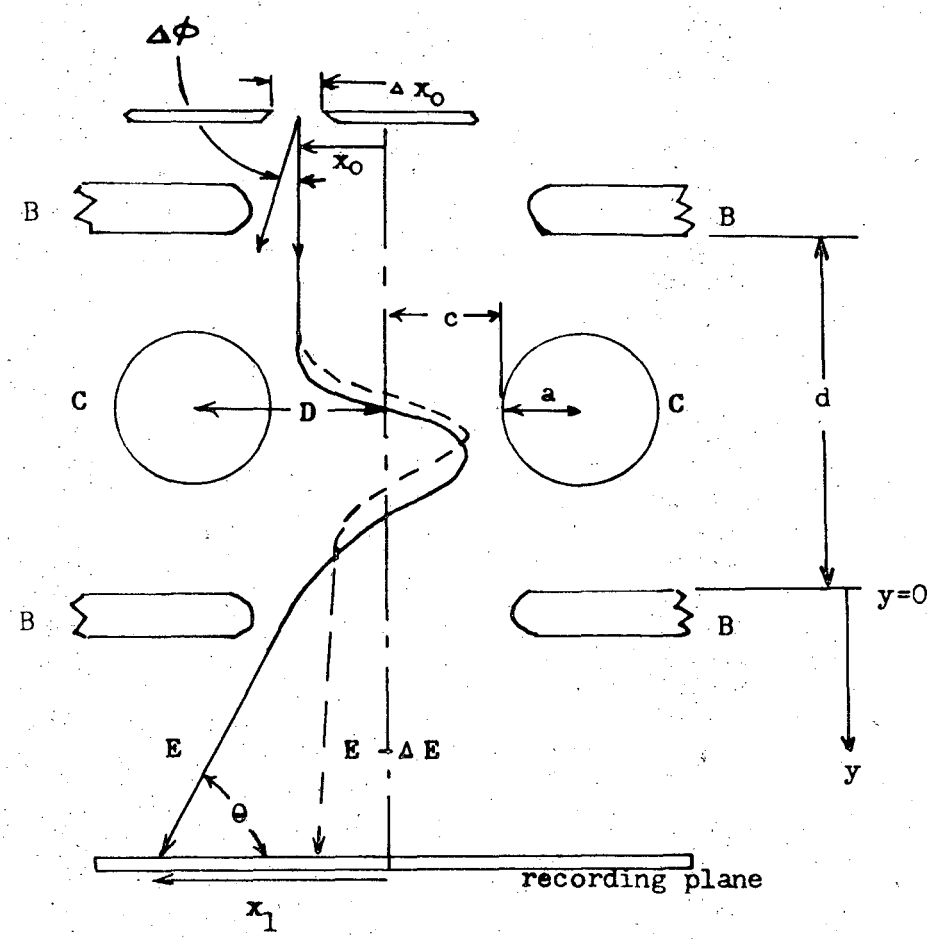

XBL 7111-7680

Fig. III.3 Electrons of two different energies E and E-ΔE are dispersed on passing through the Mollenstedt lens system, where x_o is the electron entrance coordinate, x_1 is the electron exit coordinate upon the recording plane, Δx_o is the slit width, $\Delta\phi$ is the angular spreading of the electron beam, d is the spacing between the two ground plates, a is the radius of the cylindrical electrodes, and c is half the spacing between the two cylindrical electrodes.

Many authors have derived expressions for the potential distributions in idealized electrode systems which approximate those of practical interest. A particular simple model, the line charge model, has been devised by Metherell and Whelan.[38] In this model the lens system is assumed to have two parallel and infinitely long line charges placed roughly at the center position of the cylinders. From the results thus obtained suitable equipotential surfaces may then be chosen to simulate the cylindrical electrodes of the analyzer. Although the line charge model does not possess equal potential surfaces of exactly circular shapes, Metherell and Whelan[38] and Metherell[39] have shown that it represents a good approximation of the practical circular electrodes of the system. The potential functions can be used to calculate the cardinal points, aberration coefficient, etc., of the system. The dispersion properties of the lens system can be best understood by examining the dispersion and resolution in a plot of the entrance and exit coordinates x_0 and x_1 of a monoenergetic electron beam passing through the lens (Fig. III.4a). The trajectories of electrons arriving at points x_1 corresponding to the extrema 1, 2, 3, 4 of Fig. III. 4a as well as an electron rejected by the system are shown in Fig. III.4b-f, respectively. In the absence of space charge effects, stray fields, etc., an infinite number of extrema occurs in the x_o-x_1 curve. The extremum $n=\infty$ corresponds to the case in which the electron enters the region between the electrodes and passes through the saddle point S in a direction perpendicular to the axes of the two cylindrical electrodes, and becomes trapped by the lens and oscillates through the saddle point. If x_o is increased beyond this point the system behaves like a mirror and the electron is reflected back.

0 0 0 0 3 7 0 0 0 0 3

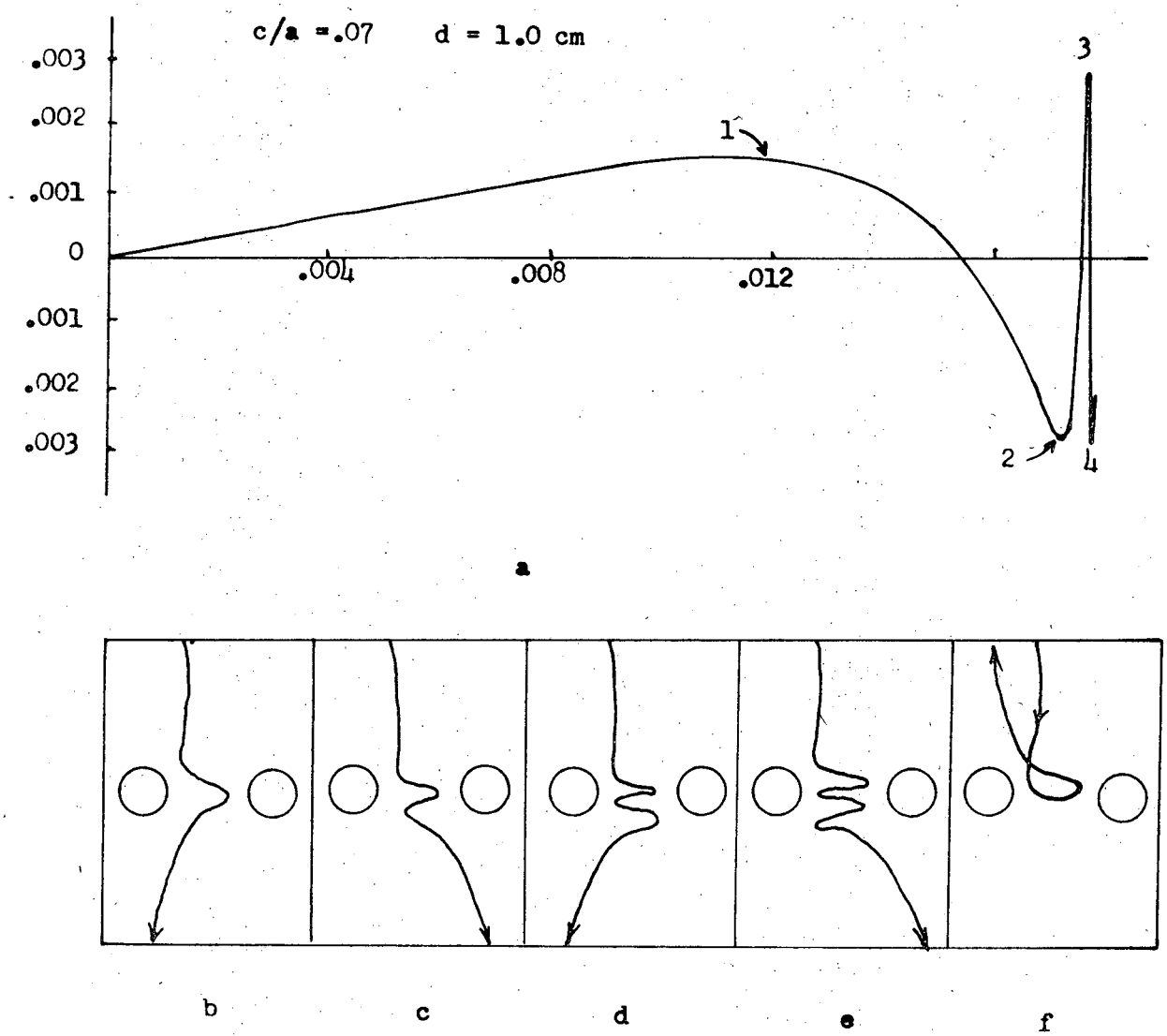

XBL 7111-7681

Fig. III.4 (a) The x_0--x_1 curve. (b) -- (e) Trajectories of electrons arriving at x_1 corresponding to extrema 1 to 4 in (a). (f) Trajectory of an electron reflected by the system.

The most important factor controlling the behavior of the lens is the value of the parameter c/a (Fig. III.3), upon which the general form of the x_o-x_1 curve depends. If the value of c/a is varied, four different types of x_o-x_1 curves can be produced. It is therefore convenient to divide the analyzer into four classes, depending upon the sign of x_1 and cosθ (Fig. III.3). The definitions of the four lens classes are given in Table III.1.

Table III.1. Definitions of the four lens classes and their approximate range of c/a.

Class	Sign of x_1	Sign of cos	Approx. range of c/a
I	-	-	∞ → 0.32
II	-	+	0.32 → 0.19
III	+	+	0.19 → 0.049
IV	+	-	0.049 → 0.034

The electron trajectories tangential to the first four pairs of caustic envelopes at y=0 in the different lens classes are shown in Fig. III.5. Examples of x_o-x_1 curves for the four lens classes are shown in Fig. III.6 for three sets of curves corresponding to different positions of recording plane on which x_1 is measured. Notice that for lens classes II and IV the effect of projection below the plane y=0 causes the first extremum of the x_o-x_1 curve to disappear. If the extreme values of x_1 in the x_o-x_1 curves are plotted as a function in y, the curves so obtained will give the caustic envelopes of the system

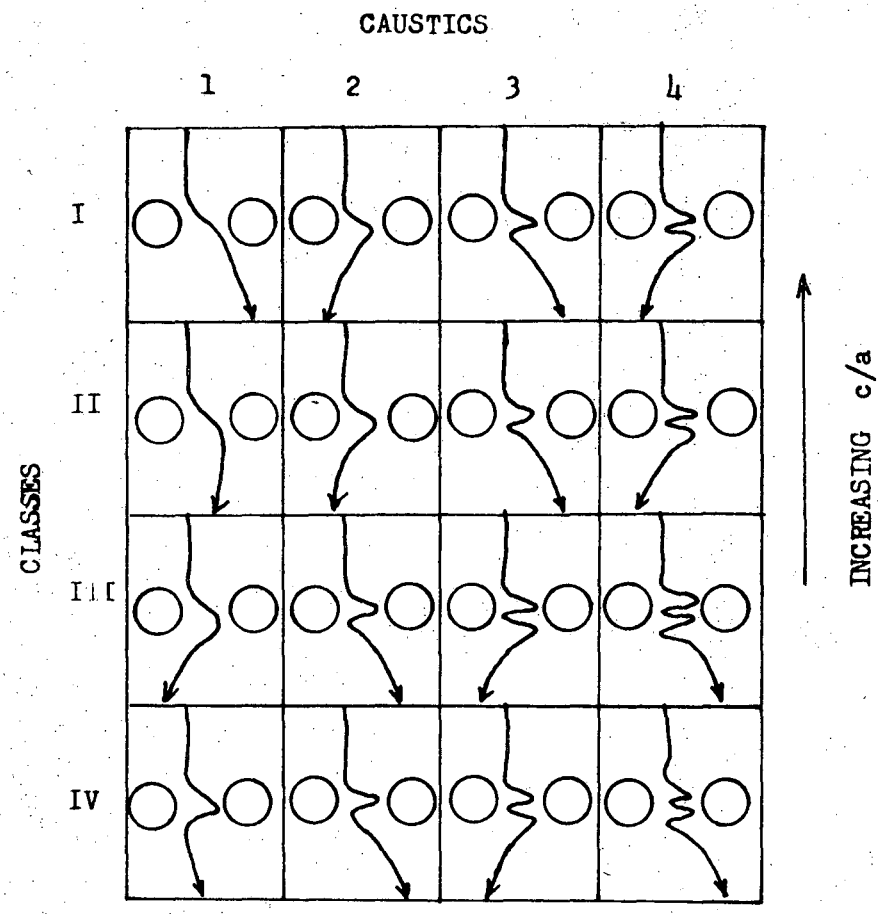

XBL 7111-7682

Fig. III.5 Schematic electron trajectories tangential to the first four pairs of caustic envelopes at y = 0 (Fig. III.3) in the first four different lens classes.

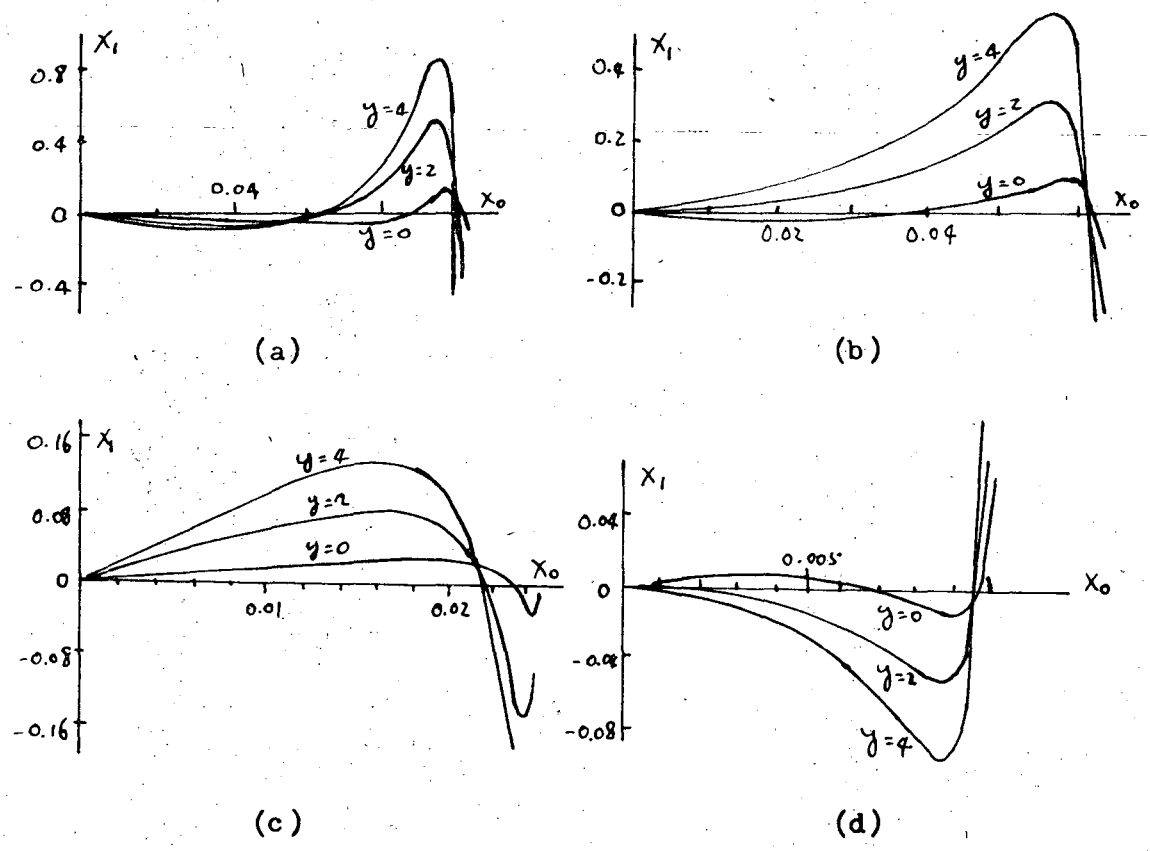

XBL 7111-7683

Fig. III.6 x_0---x_1 curves for lens of (a) class I, c/a = 0.4, d = 1, (b) class II, c/a = 0.25, (c) class III, c/a = 0.1, and (d) class IV, c/a = 0.04. Notice that the first extrema are vanished for cases (b) and (d) for y larger than zero.

(Fig. III.7a). The disappearance of the first extremum in the x_o-x_1 curves for lens classes II and IV corresponds to a disappearance of the first pair of caustic envelopes with projection in these classes (Fig. III.7b).

The lens system behavior passes from class I to II to III and to IV with decrease value of c/a. Still further reduction in c/a values causes the lens to repeat this cycling of classes in the above mentioned order. There is no theoretical limit to the number of ranges of c/a values corresponding to a particular lens class. The oscillations of electrons in the region of the saddle point responsible for the formation of high order caustics is also responsible for the cycling of lens classes.

The dispersion of the analyzer can be understood by reference to the x_o-x_1 curves for electrons of slightly different energies. Figure III.8 shows for electrons of energies E and E-ΔE in the region of the first and second extrema, electrons entering the analyzer at x_o will arrive at the recording plane separated by Δx_1. The dispersion of the analyzer $\partial x_1/\partial E$ is the quantity $\Delta x_1/\Delta E$ taken in the limit $\Delta E \to 0$. The dependence of $\partial x_1/\partial E$ on x_1 for various positions of the recording plane is given in Fig. III.9. It should be noticed that the dispersion has non-zero values at the first extremum of the x_o-x_1 curves for lens classes I and III, but is zero for the other successive extrema. This is also true for lens classes II and IV provided that the recording plane intersects the two caustic envelopes produced by these systems. If, however, the recording plane should lie below the points of intersection of the two innermost caustic envelopes of these classes of lens, then the dispersion

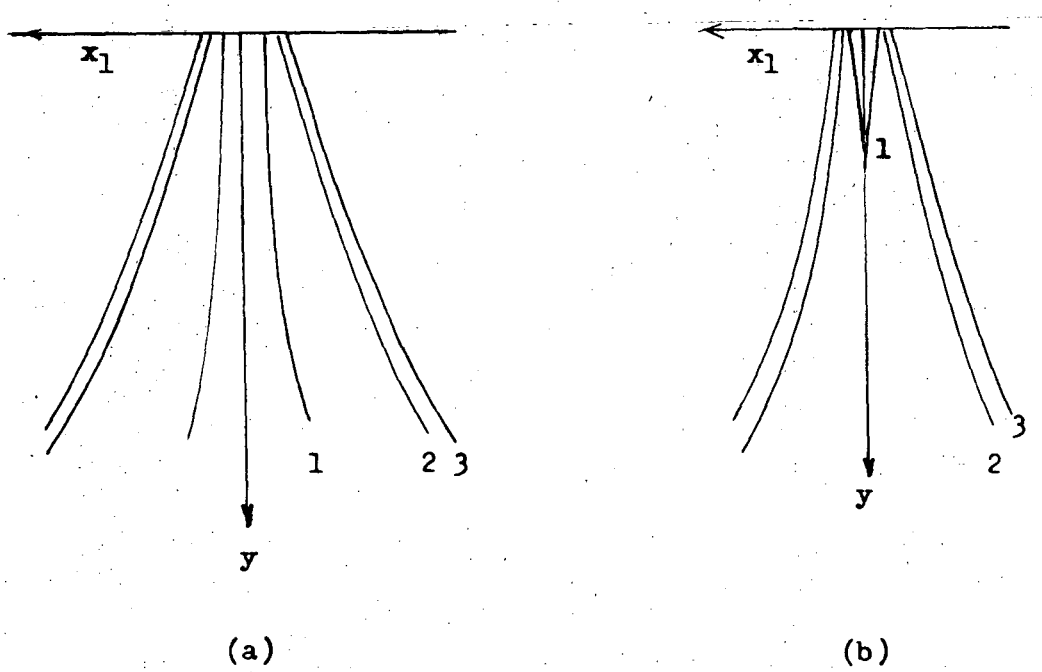

XBL 7111-7684

Fig. III.7 Behavior of caustic envelopes produced by the Mollenstedt lens system: (a) for lens classes I and III, and (b) for lens classes II and IV. The first caustic envelope vanishes for lens classes II and IV for positive values of y.

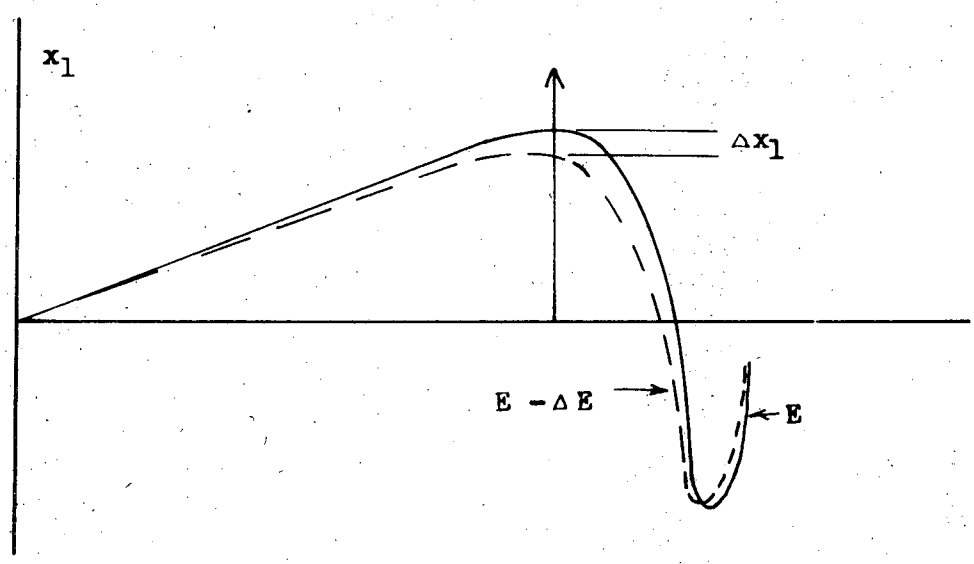

XBL 7111-7685

Fig. III.8 Schematic x_o---x_1 curves for electrons of two different energies E and E - Δ E. The dispersion of the system is defined as $\lim_{\Delta E \to 0} |\Delta x_1/\Delta E|$.

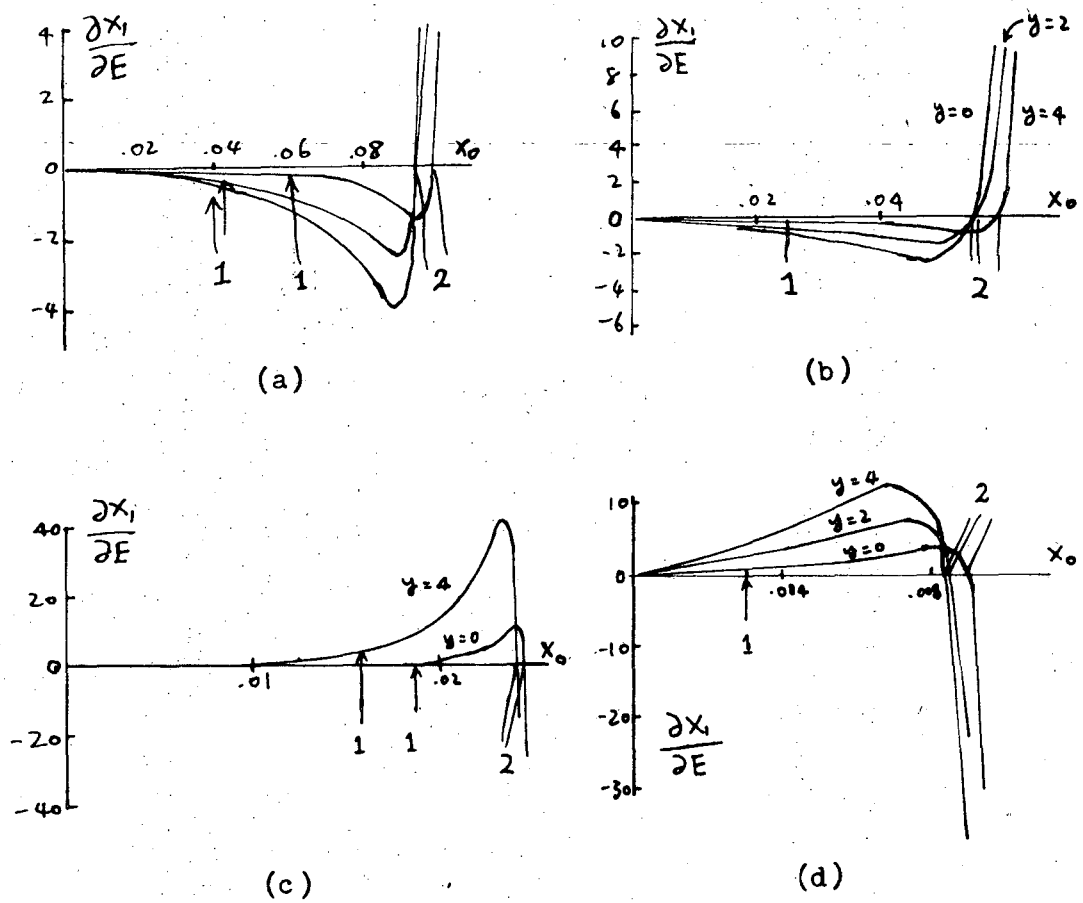

XBL 7111-7686

Fig. III.9 The behavior of the dispersion ($\partial x_1/\partial E$) as a function of x_o for different projection distances y, where d = 1cm, E = 100 keV, $\partial x_1/\partial E$ is in unit of microns/volt; and (a) lens class I, c/a = 0.4, (b) lens class II, c/a = 0.1, (d) lens class IV, c/a = 0.04.

at all extrema appearing on the recording plane is zero. Therefore, it can be concluded that the dispersion of an analyzer of any lens class is zero at all but the first caustic edges of the system.

The energy resolution is limited by two factors: (1) the size of the slit, Δx_o, which forms the entrance aperature for the electrons; and (2) the angular divergence of the beam, $\Delta\phi$ (Fig. III.3). It is obvious from the x_o-x_1 curves that a parallel monoenergetic beam passing through an entrance slit of width Δx_o will arrive at the recording plane in a strip of width $\delta x_1 = \frac{\partial x_1}{\partial x_o}\Delta x_o$ to the first order of small quantities. The variation of $\partial x_1/\partial x_o$ can be obtained directly from the x_o-x_1 curves. At the extrema of the x_o-x_1 curve, $\partial x_1/\partial x_o$ is zero and hence so is Δx_1 to the first order. In general, the energy spread is given by

$$(\Delta E)_s = \left(\frac{\partial E}{\partial x_1}\right)\left(\frac{\partial x_1}{\partial x_o}\right)\Delta x_o . \qquad \text{(III.1)}$$

Thus, a parallel beam containing electrons of two discrete energies E and E-ΔE can be resolved, if upon arriving at the recording plane their separation Δx_1 is greater than δx_1. A similar consideration shows that the resolution limited by the angular divergence of the beam, $\Delta\phi$, is given by

$$(\Delta E)_\phi = \left(\frac{\partial E}{\partial x_1}\right)\left(\frac{\partial x_1}{\partial \phi}\right)\Delta\phi . \qquad \text{(III.2)}$$

Metherell and Whelan[9] have shown that $(\Delta E)_\phi$ and $(\Delta E)_s$ are of the same order of magnitude if $\Delta\phi \sim 10^{-4}$ rad and $\Delta x_o \sim 1\mu m$. In practice a slit width of about 5 m is usually employed in the Möllentedt analyzer

for which the entrance slit lies in the final image plane of the electron microscope. At 100 keV for typical magnifications of 20,000× or less, the value of $\Delta\phi$ is in the range of 5×10^{-8} to 5×10^{-7} rad. In such cases the resolution limited by $\Delta\phi$ is therefore negligible in comparison to that limited by Δx_o. From Eq. (III.1) it is seen that high resolution $(E/\Delta E)$ is obtained when $(\partial x_1/\partial E)$ is large and $(\partial x_1/\partial x_o)$ is small. The operating position of the slit should therefore be that value of x_o at which the first extremum of the x_o-x_1 curve occurs. The classes II and IV lenses are not suitable for use as an energy analyzer because the recording plane does not in general intersect the innermost caustic envelope. Class I and III lenses usually will yield high resolution as well as good dispersion.

C. Instrumentation

Since the design details shall be given in a separate report, we will only describe the schematics of the Mollenstedt lens energy analyzing electron microscope constructed here at Berkeley. The Möllenstedt lens is mounted below the final image screen of a Siemens I electron microscope so that full advantage of the spatial resolution offered by the microscope could be taken. Since the final image screen of the microscope is untouched, normal microscopic work is undisturbed. A schematic outline of the instrument is shown in Fig. III.10. The analyzer section extends from the base of the camera chamber C_2 of the microscope to the floor. The control console of the microscope upon which C_2 usually rests is removed and mounted onto a separate trolley to allow extension of the microscope column. The entrance slit unit S of the analyzer is suspended from a trolley T which allows translation and rotation of the slit

0 0 0 0 3 7 0 0 0 6 8

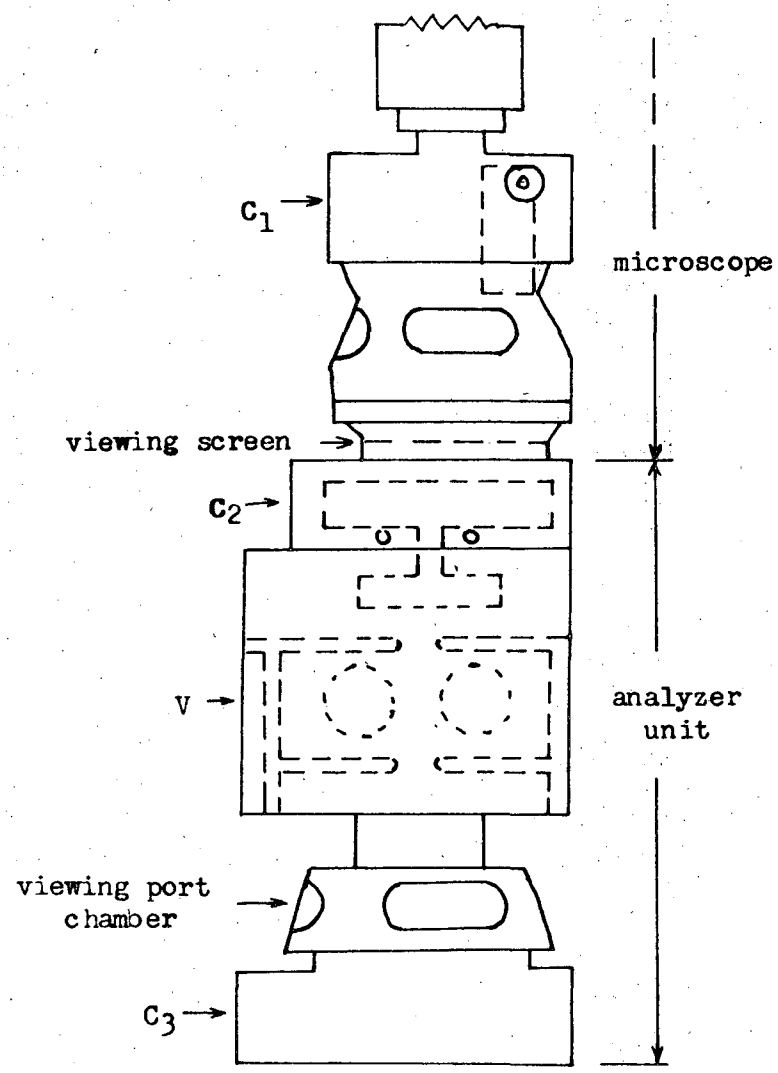

XBL 7111-7687

Fig. III.10 Schematic of the Mollenstedt lens energy analysing electron microscope.

assembly for alignment purpose. The trolley T is housed in the camera chamber C_2 which means that the image cannot be recorded on plates stored in C_2 in the usual manner. Therefore, the projector tube 35 mm camera is used to record all images and diffraction patterns. The length and width of the aperaturing slit of the analyzer can be adjusted by using controls mounted outside the vacuum and coupled to the slit assembly by sliding rods and universal joints. The electrode system of the analyzer is housed in a vacuum chamber V which is attached to the final viewing chamber and lastly the final camera chamber C_3. The Möllenstedt lens system consists of a pair of horizontal earthed plates with large entrance and exit slots (5×2 cm). A pair of parallel cylindrical electrodes at beam potential is supported midway between the plate electrodes by the porcelain insulator of a normal Siemens gun assembly.

The analyzer electrodes were designed following the criteria for dispersion and resolution given in Sec. III.B. Since high resolution is attained only for small separations of the cylindrical electrodes and the reverse is true for high dispersion, the design of the electrode system is therefore a compromise between these two factors. It is found that reasonable performance is obtained if radius of the cylindrical electrodes and the gap between them are in the range of 0.2 to 0.25 and 0.05 to 0.1 times the spacing between the two earthed plate electrodes, respectively. The resolution at maximum dispersion limited by slit width alone should then be about 3×10^{-5} for a slit width of 5 μm.

Slits used in optical spectrometers are unsuitable for electron energy analysis since the slit widths employed in the latter case are of

the order of a few microns and small scale roughness of the edges will then lead to undesirable streaking effects in the recorded spectra. A method which successfully coped with this problem is to use gold coated glass rod slits. Each slit edge piece of a Hilger spectrographic slit unit is milled down and recessed in, as indicated in Fig. III.11. Fine glass rods of diameter of about 0.3 mm are glued to the milled and recessed edges using a conducting glue. After the glue is dried, the slit edges are thoroughly cleaned with suitable solvents and then coated with a layer of evaporated gold about 1000 Å thick. To provide a tenacious layer of gold the evaporation must be carried out as slowly as possible.

The dimensions adopted for the analyzer electrode system are given in Table III.2.

Table III.2

System	1	2	3
Separation of earthed electrodes (in.)	5 11/16	"	"
Diameter of cylindrical electrodes (in.)	15/16	31/32	1
Gap between cylindrical electrodes (in.)	3/16	5/32	1/8
Slit width (μm)	⩽5μm	⩽ 5μm	⩽ 5μm

The high tension cable, which normally carries the filament and cathode lines to the microscope, is fed into an auxiliary H. T. tank (Fig. III.12). This tank is primarily used as a junction box so that the high voltage applied to the electron gun is also applied to the Möllenstedt lenses. The high voltage supplying the Möllenstedt lens is obtained by center tapping the two filament leads so that any small

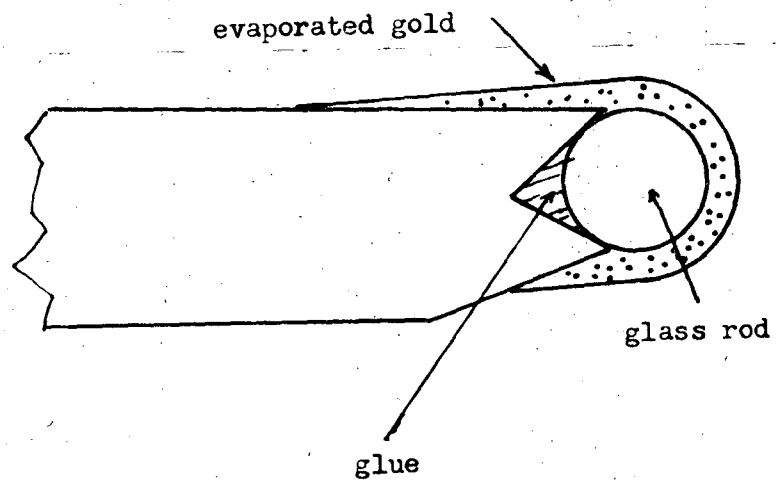

XBL 7111-7688

Fig. III.11 Cross-sectional view of the slit edge piece for the electron energy analyser.

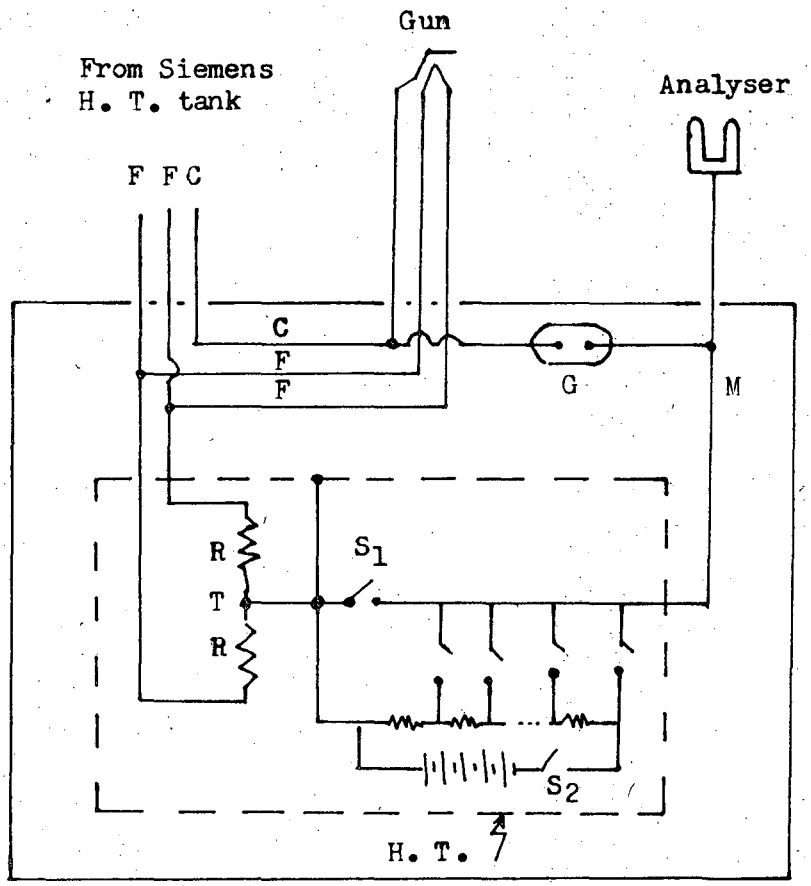

XBL 7111-7689

Fig. III.12 Outline of the auxiliary H. T. tank and calibration unit.

high voltage instability would effect the electron gun and the lenses simultaneously and equally. This is necessary because to the first order approximation there will then be no spatial displacement of the loss spectrum occurring at the recording plane due to small voltage fluctuations. The calibration circuits are designed to operate by light switches to simulate the required energy losses. The safety device G, a discharge tube connecting the cathode line to the Möllenstedt high voltage supply cable, is absolutely necessary for, if otherwise, damage to the high voltage cable and various components in the Siemens high voltage supply unit may occur, should any (high voltage) discharge in the Möllenstedt lens chamber occur.

D. Operations

Because of the limited space available in the Siemens I microscope room an auxiliary pumping system which was planned to be used at the vacuum chamber V which houses the Möllenstedt lens system was finally omitted from the construction. It was found that despite the added large volume under vacuum, the original Siemens pumping system is adequate to maintain a good vacuum with a somewhat slower initial pumping down speed. Nevertheless, under the present condition, experiments can only be performed with ease up to 80 keV. At 100 keV, high voltage discharges occur in the Möllenstedt lens chamber several minutes after the high voltage is switched on. The exact reason for this discharge is unclear, however, it is found that contamination of cylindrical lenses (at high voltage) constitutes the major nuisance. If properly cleaned, a no-discharge condition may last for as long as half an hour at 100 keV.

Proper alignment of the slit mechanism with the lens system may appear difficult, but it is not a formidable task. The slit should at first be completely opened to allow the observation of the caustical pattern, and then combined operations of the slit positioning, rotational, and width controls can be used to obtain the slit image. The image of the slit is observed to give the best performance if it is placed at a position of about 1/5 of the total separation of the first pair of caustic envelopes. Final adjustment has to be made with a specimen in the microscope upon which a loss spectrum of the material could be observed on the final viewing screen. Once the slit is properly aligned, the controls of the slit unit should not be touched during the entire experimental period. Care must be taken so as not to over-close the slit width control mechanism, otherwise the evaporated layers of gold on the two glass rods which constitute the slit mechanism may be chopped off by the slight touching of the two rods. When this happens, the remaining glass surface will become charged locally and the lens system will then produce energy loss spectrum with no spatial stability.

The main obstacle in operating the analyzer lies, however, in the lack of sufficient intensity on the final viewing screen. This is due to the small entrance aperture used (slit width is only about 5 μm). This lack of intensity makes the observation of the loss spectrum on the viewing screen a painstaking effort for the ordinary human eyes. This also necessitates the use of an exposure time of about two to four minutes during which obscuring of the recorded loss spectrum may occur due to excessive high voltage fluctuations or mechanical vibration of the environment.

The range of energy loss spectrum measurable is about 60 ev at an operating potential of 80 keV. Although a calibration circuit is designed and built, at the present stage it has not been put to use. Calibrations are therefore now done by comparison of loss spectrum of a material whose characteristic losses are well known (for example, Al has loss lines at 15.3 ev, 30.6 ev, etc.). In the range of about 0 to 25 ev, the system seems to behave linearly, and hence calibration should not present too serious a problem.

Energy resolutions obtained are of the order of 1 to 1.5 ev. It is doubtful this figure could be significantly improved since this represents a limitation imposed by the thermally emitted electron beam.

E. Possible Applications

The energy analyzing microscope can be operated to record the loss spectrum either of electrons forming a selected area diffraction pattern or of those contributing to the images of a micrograph. Several examples of such loss spectra are shown in Fig. III.13. In Fig. III.13 the loss spectra are respectively that of the bright field images of (a) Al-1% Ag, (b) Si, (c) Cu-10% Al, and (d) selected area diffraction pattern of Si. The lines S_o, S_1, S_2 etc., as indicated are the zero loss, first and second plasmon losses, etc., respectively. The loss lines in Fig. III.13 all appeared to be curved. This curvature is due partly to end caps fitted to the cylindrical lenses, but more importantly due to the fact that the trajectories of the electrons entering the slit at different points along the long dimension of the slit making different angles with the optical axis of the system (Fig. III.14). The analyzer is only sensitive to the component of the electron momentum perpendicular to the plane containing

0 0 0 0 3 7 0 3 0 7 2

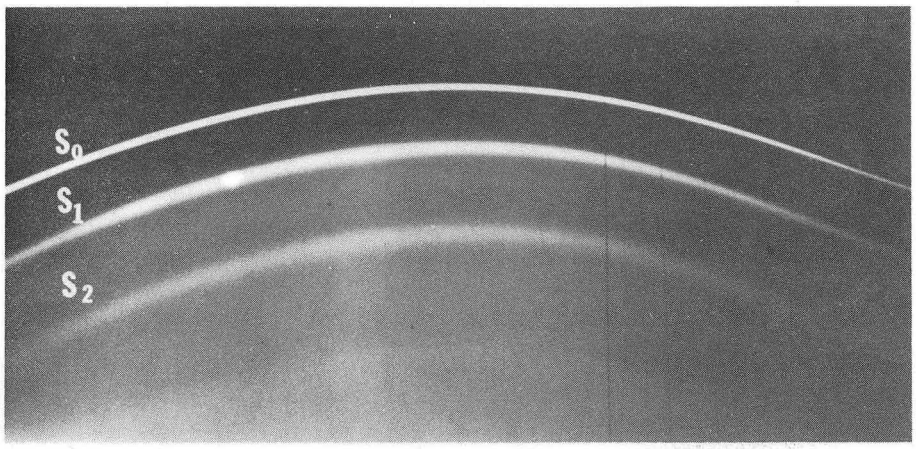

a

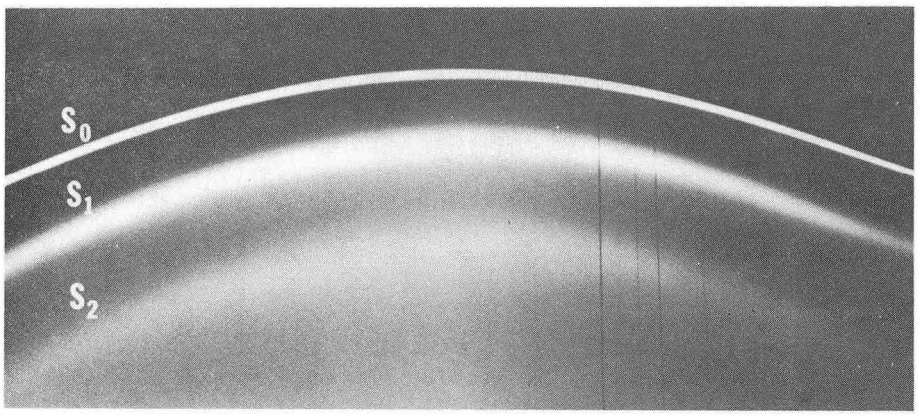

b

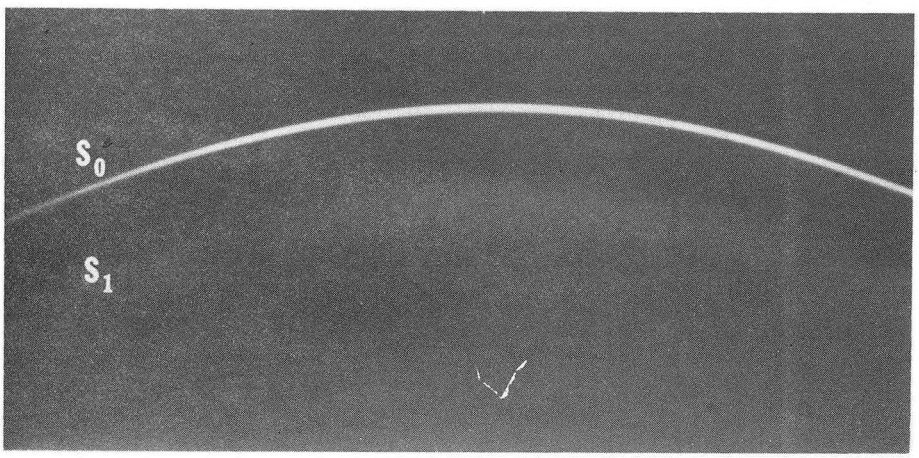

c

XBB 7111-5741

Fig. III.13

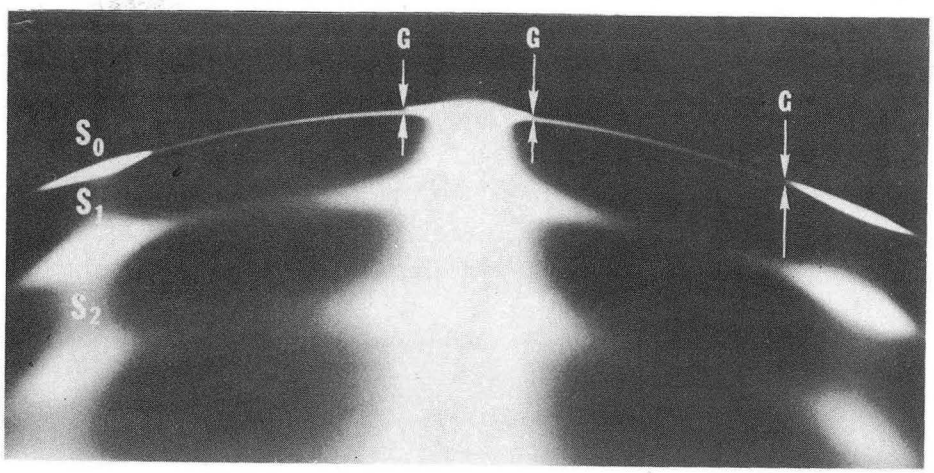

d XBB 7111-5742

Fig. III.13 Con.

Examples of characteristic loss spectra displayed by the energy analyser at 80 keV, where S_o, S_1, etc. are the zero loss, first plasmon loss lines, etc. (a) Al - 1% Ag, S_1 = 15.3 eV, (b) Si, S_1 = 16.8 eV, (c) Cu - 10% Al, S_1 = 20 eV, and (d) from Si SAD, the energy difference (0.5 to 0.9 eV) G displayed by the tails of the diffraction spots and the quasi-zero loss line is thought of due to the Si energy band gap.

0 0 0 0 3 7 0 3 0 7 3

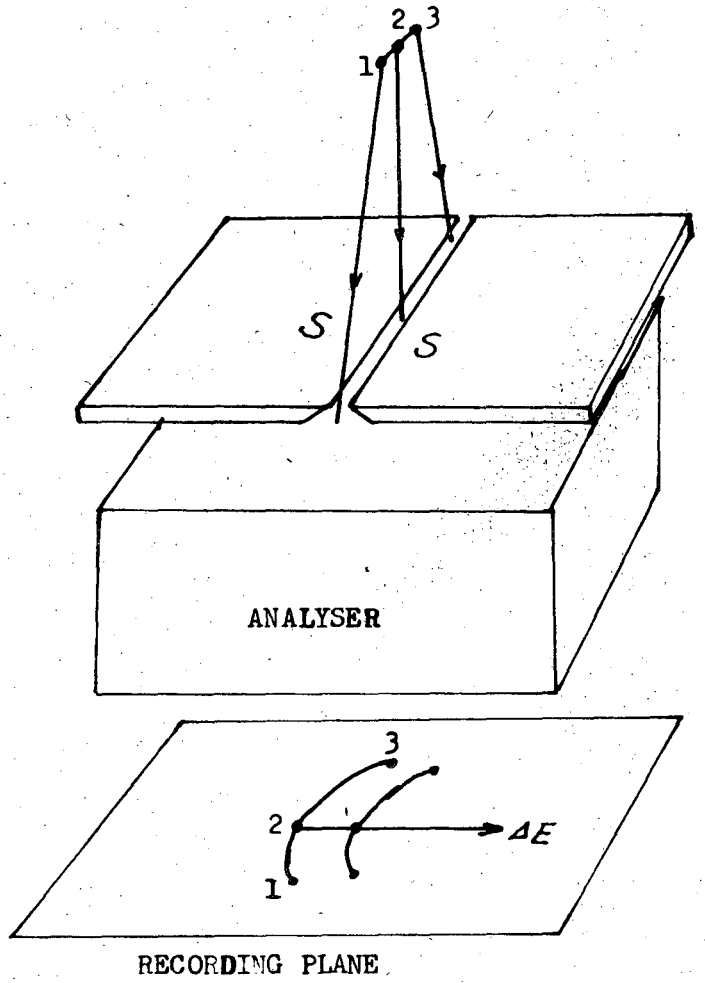

XBL 7111-7690

Fig. III.14 Illustration explaining the reason for the curvature formation of the energy loss lines.

the axes of the cylindrical lens electrodes. Electrons of the same energy arriving at points 1 and 3 (Fig. III.14) on the entrance slit have normal components of momenta less than that of an electron arriving at point 2. The result is that the analyzer registers an apparent energy loss for electrons 1 and 3, and this leads to the curvature of the loss lines shown in Fig. III.13. For the purpose of energy analysis, this curvature is unimportant since the calibration spectrum from a material with known loss lines or from calibration circuitry will bear the same effect.

Most experiments involving the use of an energy analyzing electron microscope have relied upon measurements of the loss spectra of electrons contributing to images rather than diffraction patterns. The reason is that a selected area diffraction pattern contains information averaged out over an area of specimen of the order of several microns across, whereas with an image the spatial resolution, as limited by the width of the analyzer entrance slit, is of the order of several Angstroms. This means the energy analyzing microscope provides a powerful tool for microanalysis, i.e., for measurements of the chemical compositions of microscopic regions of the specimen. Such types of applications of the energy analyzing microscope are found to be useful in determining the compositions of binary alloys, single or multiphase,[40,41] and in determining the influences on concentration gradiants due to structural imperfections, such as a grain boundary, a dislocation, a stacking fault, etc.[13,14,41] All these applications make use of the plasmon losses of the specimen. According to the simple free electron model for plasmon excitation, the energy loss E_p is given by

$$E_p = \hbar (4\pi n e^2/m)^{1/2}, \qquad \text{(III.3)}$$

where n is the number of free electrons per unit volume and the other notations have their usual physical meaning. Consequently, the variation of E_p with changes in local alloying compositions can be expected since this means a variation in n, the number of free electrons available per unit volume, due both to an addition or subtraction of free electrons and a changing in atomic spacing introduced by the presence of a second species of atoms.

We feel that another promising kind of applications of the energy analyzing microscopy is the study of semiconducting materials. In the broad scope, this should include such studies as carrier concentrations due to doping levels, anomalous carrier concentrations at the p-n junctions and the energy band gap measurements. Preliminary considerations have suggested that the probability of accomplishing meaningful measurements on doping levels is not too good, because doping levels in semiconductors are usually not high enough to allow any significant changes in plasmon energy differences to be measured. However, studies of anomalous carrier concentrations at a p-n junction shall remain as a highly promising area, especially when combined with ordinary microscopy. The semiconductor energy gaps are usually of the order of 1 ev and can be well resolved by the analyzer. A possible example of such a case is shown in Fig. III.13d, in which the quasi zero loss line consists of intensity distributions from three diffraction spots as well as that from the background smear intensities. The trailing intensities of the

spots are clearly resolved from that due to the background radiations. Measurements on the spatial separations show that the energy differences ranging from 0.5 to 0.9 ev (the energy gap of Si is known to be 1 ev). The possibility that this energy difference may be due to phonon scatterings is ruled out because (1) the measured energy difference is too large, and (2) phonon scatterings should have a continuous energy distribution, and (3) phonon loss cannot have angular range $\bar{o}$-$\bar{g}$.

IV. SUMMARY AND DISCUSSION

In the first part of this work, a theory for calculating Kikuchi electron intensity distributions is formulated. It should be noticed that this theory is also directly applicable to problems of images produced by Kikuchi electrons as well as inelastic electrons which do not contribute to the Kikuchi pattern, e.g., diffuse background electrons. The theory is formulated in terms of Bloch waves for which absorptions of both the elastic and inelastic electrons are considered. The initially generated inelastic electrons are treated as having spherical wave fronts, and during subsequent Bragg diffractions through the rest of the crystal they are regarded as forming Block waves at different deviations. As a departure from the previous theories of Kikuchi patterns, this theory is not restricted to any particular inelastic scattering mechanism, but rather, the various inelastic scattering amplitudes are treated as parameters. In this formulation we considered the facts that elastic waves belonging to different branches of the dispersion surface do not contribute equally to the generation of the inelastic electrons and that for the initially generated inelastic electrons, only the so-called intraband transitions are allowed. This theory is simpler both in concepts and in mathematics than the previous theories.

Perhaps it should be mentioned that dynamical theories using a complex lattice potential were originally formulated to specifically study the electrons scattered elastically in an "absorbing" crystal. Nevertheless, aside from those "equivalent absorptions", i.e., electrons that scattered out of the aparture or scattered into the weak beams neglected in the calculations, the term "absorption" is precisely a

description of the effects of inelastic scatterings on the elastic electrons. It is therefore not surprising that upon traveling through the crystal, in the company of elastic scatterings, (Bragg diffractions), inelastic electrons in any single energy state should also suffer from further inelastic scatterings. Thus, as it is proper to represent the effect of inelastic scatterings on the elastic electrons by absorption terms, it is also valid to include the effects of further inelastic scatterings of inelastic electrons at any energy state by similar absorption terms. This means, that in the Bloch wave representation of inelastic electrons at a single energy state, properly chosen values of the imaginary parts must also be included in each component of the crystal lattice potential. However, it should be mentioned that at this stage correct values of imaginary part of the lattice potential for inelastic electrons are not yet available from either experimental data or any theoretical estimations.

In applying this theory to calculate the Kikuchi patterns, a two-beam (for inelastic electrons) approximation is adapted. It is also further assumed that only inelastic electrons in the first excited energy state contribute most significantly to the formation of Kikuchi patterns. The imaginary parts of the lattice potentials for the inelastic electrons in this calculation are chosen arbitrarily, in fact, just those for the elastic electrons have been used. All of these approximations involved should by no means be regarded as physically vigorous. Nevertheless, in comparison with previous theories, the success of this formulation is evident in the sense that, contrary to most of the previous theories, which explained only one aspect of the

behavior of the Kikuchi pattern, details of a majority of the most important aspects of the behavior of the Kikuchi intensity distributions are explained. The versatility of this theory is further evidenced by the fact that the method of summing up all rocking curve intensities for computing the Kikuchi pattern of a systematic many-beam case is shown to be a special case of this theory. In deriving this result, the approximations used are specifically: (1) only inelastic electrons in the first excited energy state contribute; (2) the crystal is thick, hence the elastic beams are replaced by a δ-function type of excitations at the top crystal surface; (3) ignorance of interactions between certain waves. It is clearly seen that all these approximations are at best of equal crudeness as those used in the two-beam calculations. According to Thomas and Humphreys[36] and Thomas,[42] however, remarkable agreements with experiments have been achieved by calculations using this method for the many-beam systematic cases. All these facts suggest that in order to explain the various aspects of the behavior of the Kikuchi pattern, contrary to a common belief that inelastic scattering mechanisms play a central role, absorptions of both elastic and inelastic electrons are the more important factors needed to be considered.

In comparing the calculated two-beam results with experimental observations, the following quantitative discrepancies are noticed: (1) In the contrast change of Kikuchi band from an excess to a deficiency of electrons with changes in specimen thickness, the computed results show that the band is dificient only if the crystals are very thick, and the change of contrast takes place through a large range in specimen thickness. It is experimentally observed that the contrast change may

occur within a relatively small range of specimen thickness, also, deficient bands may start to appear for crystals of thicknesses smaller than the values shown by the computed results. (2) Although the computed Kikuchi line spacing variations are in good qualitative agreement with experiments, however, the range of excursion of the computed variations are somewhat smaller than those experimentally observed. (3) According to the computed results, the Kikuchi line pair should have the usual normal (black-and-white) contrast for thicknesses of any old multiples of $\xi g/2$ and reversed contrast (white-and-black) contrast for specimens of thicknesses of any integral multiples of ξg. Thus, the possibility of observing either the normal or the reversed contrasts are equal, however, experimentally it is more difficult to observe the reversed contrast. These discripancies between the caluclated and the experimental results are mainly attributed to the approximations used in the calculations: (1) the calculations is two-beam, (2) only inelastic electrons of the first excited energy state are considered, (3) correct values of the imaginary parts of the lattice potentials are not available. Nevertheless, experimental conditions may also have important influences on the results observed. For instance, in any experiment, effects on the observed results due to small local bending of the specimen, specimen thickness variations and small deviations from any desired Bragg positions, etc., must be considered. Nevertheless, it should be mentioned that, many-beam calculations considering inelastic electrons of more than one energy state with properly chosen imaginary parts of the lattice potentials should lead to better results.

Just as the elastic electrons are capable of producing images of

defects in a crystal, so are the inelastic and Kikuchi electrons. Compared to images produced by elastic electrons, those due to the inelastic electrons are characterized by broader image widths, more spatial frequency components and perhaps also a shifting in image positions. This is so because, on becoming inelastic, the coherencies of these electrons are lost with respect to the elastic electrons and, more important, even with respect to other inelastic electrons in the same energy state but which were generated from a different depth in the crystal. Subject to the same displacement field due to the defect, the final image obtainable from any inelastic electrons consists of information carried by (inelastic) electrons which went through two different image formation processes, depending upon whether the electrons became inelastic before or after traveling through the displacement field of the defect. If the electrons became inelastic before reaching the displacement field, then image informations are obtained by these electrons directly. On the other hand, if the electrons became inelastic only after traveling through the displacement field, then image information is merely passed onto these electrons from their past history (while they were elastic). Since inelastic scatterings involve some random phase shifts to the wave functions of the electrons, it is suggested that this is a major reason for the fuzziness of the images due to the inelastic electrons. In practive, however, there is no way to separate these two processes, especially if the defect imposes a displacement field of infinite spatial extent to the crystal (e.g., that due to a dislocation or a small particle). Images due to inelastic electrons are interesting primarily for the purpose of characteristic noise (image) removal so that images

produced only by elastic electrons can be obtained and enhanced for better resolutions.

In the second part of this thesis, the design and construction schematics of an energy analysing microscope are given. Possible application of energy analysing microscopes are given. In principle, an energy analysing electron microscope should provide a powerful tool for microanalysis. A first kind of its applications is the study of metallurgical problems involve measurements of plasmon loss spectra and their variations with specimen local composition changes. Physics of plasmon excitations tend to limit useful spatial resolutions as well as energy resoltuions the energy analyser can provide under its best performence. First, the plasmon wavelength limits the useful spatial resolution of the analyser to regions on the specimen of a diameter of the order 100 Å or larger. This is so because plasmon oscillations in a solid is a quantized density wave of electrons with a particular wavelength within which all participating electrons oscillate collectively. Thus, in a region of the range of a plasmon wavelength, only the average electron density can be measured. The plasmon wavelengths of metals is of the order of 100 Å or larger. Thus, although the spatial resolution limited by the energy analyser slit can be reduced to a value well below that of the microscope by simply increasing the magnification of the image, meaningful measurements can only be performed over regions separated by a distance sufficiently larger than a plasmon wavelength.

In order to obtain dependable and meaningful results, full advantage of the energy resolution offered by the analyser must be taken. This

restricts the microanalysis studies of the composition problems to materials which posses sharply defined and well separated plasmon loss spectra. There is only one kind of material that meets this requirement: Al basis alloys. Other materials of metallurgical interests (Cu and Fe basis alloys, etc.) do not posses such a sharply defined plasmon loss spectrum. Instead of a sharp line like loss spectrum of Al, the plasmon loss spectra of these materials have an energy distribution in the form of a smeared band (see, for example, Fig. III. 13c, the spectrum of Cu - 10% Al). This wide band type of plasmon loss spectra made it improbable to accurately allocate the peak of the intensity distribution displayed by the analyser, let alone tackle the question of measuring from these spectra any small changes introduced by small composition variations. This phenomenon may be understood qualitatively by considering the electronic structures of the atoms of the various materials. For Al, the n = 2 quantum level is complete. The three electrons at the outermost shell ($3s^2$, $3p^1$) behave closely to that predicted by the free electron model for plasmon excitations. On the other hand, the eight outermost electrons of Fe are distributed as $3d^6$ and $4s^2$, i.e., the 3d level is incomplete. These is a finite probability that these electrons could occupy the unfilled energy levels $3d^7$ to $3d^{10}$ for a short period of time, and thus making it unclear as to how many electrons should participate in the plasmon oscillations. The result is that the excitation of a single mode of plasmon becomes highly improbable and hence the broad band type plasmon loss spectrum appears. In the case of Cu, although now the n = 3 shell is complete ($3d^{10}$ and $4s^1$), the several outermost energy levels are nevertheless very closely spaced and hence

these electrons are tightly coupled. In this case it is again true that there is no clear answer as to how many modes can be excited. It may be concluded at this point that despite the high energy resolution and the extra-ordinarily fine spatial resolution offered by the best performance of the energy analyser, its appliability to microanalysis of composition variation measurements is perhaps limited to only Al basis alloys with a spatial resoltuion of the order of 100 Å.

Perhaps a more promising class of applications, not mentioned in the literature, is the measurements of doping levels, anomalous carrier concentrations at junctions and energy gaps of simiconductors. For example, Si has reasonably well defined plasmon loss spectrum (Fig. III. 13b). Although the prospects for doping elevel measurements are low (since the doping levels are usually too low to induce any significant plasmon energy variations), at the p - n junctions, anomalous carrier concentrations should be high enough to allow the microanalysis technique to be applied. Energy analysing microscopes should also prove to be a useful tool for direct and easy measurement of the energy gaps of semiconductors. Of the order of 1 eV, characteristic loss spectrum due to the presence of the energy gap could be well resolved. One possible such example has been given by Fig. III.13d. It should be noticed, however, that the energy analysing microscope could also be used to study the physical principles involving certain type of the charateristic losses. For example, the dependence of the excitation and dispersion of the surface and volume plamons with specimen thickness.

APPENDIX

FUNDAMENTALS OF THE DYNAMICAL THEORY

A.1. Solution of the Many-Beam Problem--The Dispersion Matrix

The study of the ordinary dynamical theory of electron diffractions forms the necessary background knowledge of this work. For purposes relevant with this thesis, the problem shall be written in the form of a system of linear differential equations so that solutions of the problem can be exclusively derived from the dispersion matrix of the system.

High energy electrons entering the crystal is described by the Schrödinger equation (Eq. (II.7))

$$\left\{ \nabla^2 + 4\pi^2 \left[k_r^2 + \sum_{g \neq 0} U_g e^{2\pi i \bar{g}\cdot\bar{r}} \right] \right\} \psi(\bar{r}) = 0. \qquad \text{(A.1)}$$

Because of the periodic nature of the atomic arrangement in a crystal, in Eq. (A.1) the crystal potential has been written in the form of a Fourier series and then normalized, i.e.,

$$V(\bar{r}) = \sum_{g \neq 0} V_g e^{2\pi i \bar{g}\cdot\bar{r}}, \qquad \text{(A.2a)}$$

$$U_g = \left(\frac{2me}{h^2} \right) V_g, \qquad \text{(A.2b)}$$

where $\bar{g}$ is a reciprocal lattice vector. The quantity $k_r = (2me(E+V_o))^{1/2}/h$ is the mean refracted wave vector of the electrons in the crystal, which has been adjusted to account for the refraction due to the mean

inner potential V_o.

For a centro-symmetric crystal, the relation $V_{-\bar{g}} = V_{\bar{g}}$ holds. In general, V_g must be regarded as a complex quantity. This is necessary because on passing through a crystal, the electrons suffer from an attenuation phenomenon called "absorption." Absorption of electrons is found to be diffraction dependent and are not uniform for all electrons (and hence the terms "anomalous absorption" and "anomalous transmission"). The introduction of an imaginary part into the lattice potential was first suggested by Honjo and Mihama[43] as a phenomenological description of the absorption of electrons and was theoretically justified in part by works of Yoshioka,[20] Hall and Hirsch,[24] Hall[25] and Gjønnes.[44]

Because of the translational invariance of the periodic potential, the wave function of the electrons inside the crystal must also be periodic. Hence, the solution of Eq. (A.1) is given by the Bloch wave function[45]

$$\psi(\bar{r}) = \sum_{h} C_h e^{2\pi i(\bar{k}+\bar{h})\cdot\bar{r}} . \tag{A.3}$$

Following the procedure leading to Eq. (II.18), Eq. (A.1) can be shown to yield

$$\frac{d\psi_h(\bar{r})}{dz} = 2\pi i \left\{ (k_r + S_h)\,\psi_h(\bar{r}) + \sum_{\bar{g}\neq\bar{h}} \frac{1}{2\xi_{\bar{h}-\bar{g}}}\,\psi_g(\bar{r}) \right\}, \tag{A.4}$$

where

$$S_h = |\bar{k}_x + \bar{k}_y + \bar{h}|^2 / 2\,\mathrm{Re}(k_r) , \tag{A.5a}$$

$$\xi_h = Re(k_r)/U_h \quad . \tag{A.5b}$$

In deriving Eq. (A.4) it is assumed that reflections of waves at both the entrant and exit surfaces of the crystal are neglected.[46] This assumption also allows the boundary condition at the entrant surface to be reduced to $\psi_o = 1$ and $\psi_h = 0$, if $h \neq 0$. On writing out explicitly in a matrix form by letting $\bar{h} = 0, \bar{g}_1, \bar{g}_2, \ldots, \bar{g}_n$, Eq. (A.4) yields

$$\frac{d}{dz}\begin{bmatrix} \psi_c(z) \\ \psi_{g_1}(z) \\ \vdots \\ \psi_{g_n}(z) \end{bmatrix} = 2\pi i \begin{bmatrix} k_r + S_c & \frac{1}{2\xi_{-\bar{g}_1}} & \cdots & \frac{1}{2\xi_{-\bar{g}_n}} \\ \frac{1}{2\xi_{\bar{g}_1}} & k_r + S_1 & \cdots & \frac{1}{2\xi_{\bar{g}_1-\bar{g}_n}} \\ \vdots & \vdots & \ddots & \vdots \\ \frac{1}{2\xi_{\bar{g}_n}} & \frac{1}{2\xi_{\bar{g}_n-\bar{g}_1}} & \cdots & k_r + S_{\bar{g}_n} \end{bmatrix} \begin{bmatrix} \psi_c(z) \\ \psi_{g_1}(z) \\ \vdots \\ \psi_{g_n}(z) \end{bmatrix} . \tag{A.6}$$

With the substitutions

$$\phi_{\bar{h}}(z) = \psi_{\bar{h}}(z)\, e^{-2\pi i\, Re(k_r) z} , \tag{A.7a}$$

$$t = \pi i z / Re(\xi_{g_1}) , \tag{A.7b}$$

$$W_h = Re(\xi_{g_1}) \left[S_h + i\, Im(k_r) \right] , \tag{A.7c}$$

$$\xi'_{1(m-\ell)} = \frac{\dfrac{1}{\xi_{\bar{g}_m - \bar{g}_\ell}}}{\mathrm{Re}\left(\dfrac{1}{\xi_{\bar{g}_1}}\right)}, \tag{A.7d}$$

Eq. (A.6) is further simplified into

$$\frac{d}{dt}\begin{bmatrix} \phi_c(t) \\ \phi_{g_1}(t) \\ \vdots \\ \phi_{g_n}(t) \end{bmatrix} = \begin{bmatrix} 2W_0 & \xi'_{1(-1)} & \cdots & \xi'_{1(-n)} \\ \xi'_{11} & 2W_1 & \cdots & \xi'_{1(1-n)} \\ \vdots & \vdots & \ddots & \vdots \\ \xi'_{1n} & \xi'_{1(n-1)} & \cdots & 2W_n \end{bmatrix} \begin{bmatrix} \phi_c(t) \\ \phi_{g_1}(t) \\ \vdots \\ \phi_{g_n}(t) \end{bmatrix}, \tag{A.8a}$$

or, in vectorial form

$$\frac{d}{dt}\,\underset{\sim}{\phi}(t) = \underset{\approx}{A}\;\underset{\sim}{\phi}(t)\,. \tag{A.8b}$$

Subject to the boundary condition that

$$\begin{bmatrix} \phi_c(0) \\ \phi_{g_1}(0) \\ \vdots \\ \phi_{g_n}(0) \end{bmatrix} = \begin{bmatrix} 1 \\ 0 \\ \vdots \\ 0 \end{bmatrix}, \tag{A.9}$$

the solution of Eq. (A.8) is

$$\begin{bmatrix} \phi_c(t) \\ \phi_{g_1}(t) \\ \vdots \\ \phi_{g_n}(t) \end{bmatrix} = \left\{ \exp \begin{bmatrix} 2W_0 & \xi'_{1(-1)} & \cdots & \xi'_{1(-n)} \\ \xi'_{11} & 2W_1 & \cdots & \xi'_{1(1-n)} \\ \vdots & \vdots & \ddots & \vdots \\ \xi'_{1n} & \xi'_{1(n-1)} & \cdots & 2W_n \end{bmatrix} t \right\} \begin{bmatrix} 1 \\ 0 \\ \vdots \\ 0 \end{bmatrix} . \tag{A.10}$$

Define the dispersion matrix as

$$\underset{\approx}{\Phi}(t-t_0) = e^{\underset{\approx}{A}(t-t_0)} = \left\{ \exp \begin{bmatrix} 2W_0 & \xi'_{1(-1)} & \cdots & \xi'_{1(-n)} \\ \xi'_{11} & 2W_1 & \cdots & \xi'_{1(1-n)} \\ \vdots & \vdots & \ddots & \vdots \\ \xi'_{1n} & \xi'_{1(n-1)} & \cdots & 2W_n \end{bmatrix} (t-t_0) \right\} , \tag{A.11}$$

Eq. (A.10) may be written in the vectorial form

$$\underset{\sim}{\phi}(t) = \underset{\approx}{\Phi}(t-t_0)\, \underset{\sim}{\phi}(t_0) . \tag{A.12}$$

Sturkey,[46] Fujimoto[47] and Niers[48] have used the dispersion matrix to solve the electron diffraction problem. However, the properties of this matrix are not fully discussed, reliable methods for calculating this matrix are also not given. It is easily deduced from Eqs. (A.10) and (A.11) that the dispersion matrix has the following properties:

$$\underset{\approx}{\bar{\Phi}}(t_c - t_c) = \underset{\approx}{I} \quad , \tag{A.13a}$$

$$\underset{\approx}{\bar{\Phi}}(t_2 - t_c) = \underset{\approx}{\bar{\Phi}}(t_2 - t_1)\, \underset{\approx}{\bar{\Phi}}(t_1 - t_c), \tag{A.13b}$$

$$\underset{\approx}{\bar{\Phi}}(t_1 - t_c) = \underset{\approx}{\bar{\Phi}}^{-1}(t_c - t_1) . \tag{A.13c}$$

Elements of the first column of the dispersion matrix have the property

$$\bar{\Phi}_{i1}(\Delta t) = \Phi_{\bar{g}(n-1)}(\Delta t). \tag{A.13d}$$

Eq. (A.13d) is also true for elements of the first row of the dispersion matrix if the crystal is centro-symmetric. This important property has been used in Sec. 11.E.4. The Bloch like coefficients Φ_{ij}^{k} of each matrix element obeys

$$\sum_{k=1}^{n+1} \bar{\Phi}^{k}_{ij} = \delta_{ij} , \tag{A.13e}$$

and

$$\sum_{\ell} \bar{\Phi}^{k}_{i\ell} \bar{\Phi}^{m}_{\ell j} = \bar{\Phi}^{k}_{ij} \delta_{km} \tag{A.13f}$$

If the dispersion matrix is calculated, then the problem of many beam diffraction in a perfect crystal can be considered as solved. However, Eq. (A.12) does not yield the solution of Eq. (A.11) so readily, because the exponential function of a matrix is not easily obtainable in general. Although many methods for calculating the dispersion matrix exist, the study of this matrix has nevertheless been largely ignored. Aside from the fact that this matrix is not so easy to calculate, perhaps the main reason for this situation is that the solution of the many beam problem for a perfect crystal is not as interesting as the image problems, and it was thought that the study of the detailed solution of the dispersion matrix offers very little or no help in solving the image problems. It will be shown, however, that the dispersion matrix is of fundamental importance in understanding the nature of electron diffractions, and that it is also of great practical advantage to use the dispersion matrix to solve the image problems. In fact, analytical forms of the dispersion matrix are readily obtainable for the two and three beam cases, and these analytical forms of the dispersion matrix allows the solution of image problems in these cases to be readily

computed. For the many beam problems, the use of the dispersion matrix also enables the computations of the images to be greatly simplified, and the usual problem of electron intensity non-conservation encountered in other methods will simply not arise. For this reason, we will discuss several methods of calculating the dispersion matrix in the next section.

A.2. Methods for Calculating the Dispersion Matrix

A.2.1 Method of Series Expansion

The most straightforward (and the only widely used) method of calculating the dispersion matrix is to use the series expansion

$$\underset{\approx}{\Phi}(\Delta t) = e^{\underset{\approx}{A}\Delta t} = \underset{\approx}{I} + \underset{\approx}{A}\Delta t + \frac{1}{2!}\underset{\approx}{A}^2\Delta t^2 + \cdots \tag{A.14a}$$

Eq. (A.14a) is useful only when Δt is very small and hence the approximation

$$e^{\underset{\approx}{A}\Delta t} = \underset{\approx}{I} + \underset{\approx}{A}\Delta t \tag{A.14b}$$

can be used. For large values of Δt, the series in Eq. (A.14a) converges slowly and the calculation becomes tedious. In comparison with other methods, however, it will soon be clear that the most serious shortcoming this method suffers from is the lack of an intermediate representation of the results obtained and hence little or no correlation can be deduced for purpose of extending the result at one specimen thickness to another.

Despite of this difficulty, this method is the most widely used one, because in the study of image problems where $\underset{\approx}{A}$ is not a constant

matrix, it is thought that this is the only simple method.

A.2.2. The Method of Laplace Transforms

Following the method of Laplace transforms given in any standard text, the transform of Eq. (A.12) is, by letting $t' = t - t_o$,

$$s\hat{\underset{\approx}{\Phi}}(s) - \underset{\sim}{\phi}(0) = \underset{\approx}{A}\,\hat{\underset{\approx}{\Phi}}(s) \tag{A.15a}$$

or

$$\hat{\underset{\approx}{\Phi}}(s) = (s\underset{\approx}{I} - \underset{\approx}{A})^{-1}\underset{\sim}{\phi}(0) = \mathcal{L}\,\underset{\sim}{\phi}(t') \tag{A.15b}$$

i.e.,

$$\underset{\sim}{\phi}(t - t_o) = \mathcal{L}^{-1}\left[(s\underset{\approx}{I} - \underset{\approx}{A})^{-1}\right]\underset{\sim}{\phi}(0) \tag{A.15c}$$

where

$$\hat{\underset{\approx}{\Phi}}(s) = \left[(s\underset{\approx}{I} - \underset{\approx}{A})^{-1}\right] = \frac{\mathrm{adj}\,(s\underset{\approx}{I} - \underset{\approx}{A})}{|s\underset{\approx}{I} - \underset{\approx}{A}|}, \tag{A.16a}$$

and

$$\underset{\approx}{\Phi}(t') = e^{\underset{\approx}{A}t'} = e^{\underset{\approx}{A}(t - t_o)} = \mathcal{L}^{-1}\,\hat{\underset{\approx}{\Phi}}(s). \tag{A.16b}$$

In Eq. (A.16a),

$\mathrm{adj}\,(s\underset{\approx}{I} - \underset{\approx}{A}) =$ adjoint matrix of $(s\underset{\approx}{I} - \underset{\approx}{A}) = [\,|(s\underset{\approx}{I} - \underset{\approx}{A})|^{ji}\,]$,

$|s\underset{\approx}{I} - \underset{\approx}{A}|^{ji} =$ cofactor of the jith element of $(s\underset{\approx}{I} - \underset{\approx}{A})$,

$|s\underset{\approx}{I} - \underset{\approx}{A}| =$ determinant of $(s\underset{\approx}{I} - \underset{\approx}{A})$.

In a system of n+1 beams, $\underset{\approx}{A}$ is a (n+1) x (n+1) matrix, hence the determinant is a (n+1) th degree polynominal which may be written as

$$|s\underset{\approx}{I} - \underset{\approx}{A}| = s^{n+1} + a_1 s^n + \cdots + a_{n+1}$$

$$= (s-\alpha_1)^{m_1}(s-\alpha_2)^{m_2} \cdots (s-\alpha_k)^{m_k}. \qquad \text{(A.17)}$$

Eq. (A.17) is the characteristic polynominal of the system and $\alpha_1, \cdots, \alpha_n$ are the eigenvalues, note that

$a_i = (-1)^i \, tr_i \, \underset{\approx}{A}$, $i = 1, 2 \cdots n+1$, where

n+1 = order of system, and $tr_i A$ denotes the sum of the principal minors of order i of the characteristic matrix $\underset{\approx}{A}$. In particular

$$tr_1 A = \text{trace } \underset{\approx}{A}, \text{ and } tr_{n+1}\underset{\approx}{A} = |A|.$$

Each element of the adjoint matrix in the numerator of Eq. (A.16a) is a polynominal of degree n; consequently

$$\hat{\underset{\approx}{\Phi}}(s) = \frac{\operatorname{adj}(s\underset{\approx}{I} - \underset{\approx}{A})}{|s\underset{\approx}{I} - \underset{\approx}{A}|} = \frac{\underset{\approx}{B}_1 s^n + \underset{\approx}{B}_2 s^{n-1} + \cdots + \underset{\approx}{B}_n}{s^{n+1} + a_1 s^n + \cdots + a_{n+1}}, \tag{A.18}$$

where $\underset{\approx}{B}_1, \underset{\approx}{B}_2, \ldots, \underset{\approx}{B}_n$ are (n+1) x (n+1) matrices. By inspection of the matrix $(s\underset{\approx}{I} - \underset{\approx}{A})$ for any typical A, it is evidently

$$\underset{\approx}{B}_1 = \underset{\approx}{I}$$

The task of computing the cofactors of $(s\underset{\approx}{I} - \underset{\approx}{A})$ is quite laborious when n>2; it may be avoided by computing instead the matrices $\underset{\approx}{B}_k$ of the numerator and the coefficients a_k of the denominator of $\hat{\underset{\approx}{\Phi}}(s)$ by means of the algorithm

$$a_k = \frac{-1}{k} \operatorname{trace}(\underset{\approx}{A}\,\underset{\approx}{B}_k), \quad k = 1, 2, \cdots n+1 \tag{A.19a}$$

and

$$\underset{\approx}{B}_{k+1} = \underset{\approx}{A}\,\underset{\approx}{B}_k + a_k \underset{\approx}{I}, \quad k = 1, 2, \cdots n. \tag{A.19b}$$

The dispersion matrix $\underset{\approx}{\Phi}(t') = e^{\underset{\approx}{A}t'}$ is the inverse Laplace transform of $\hat{\underset{\approx}{\Phi}}(s) = (s\underset{\approx}{I} - \underset{\approx}{A})^{-1}$. In order to find the general form of $\underset{\approx}{\Phi}(t)$, we expand $\hat{\underset{\approx}{\Phi}}(s)$ in partial fractions and obtain

$$\hat{\underset{\approx}{\Phi}}(s) = (s\underset{\approx}{I} - \underset{\approx}{A})^{-1} = \sum_{p=1}^{k} \sum_{r=1}^{m_k} \underset{\approx}{A}_{rp} \frac{1}{(s - \alpha_p)^r}, \tag{A.20}$$

where $\alpha_p \; (p = 1, 2, \cdots k \leq n+1)$ are the roots of the characteristic equation, Eq. (A.17), and m_p are their respective multiplicities. After $\hat{\underset{\approx}{\Phi}}(s)$ has been found by Eq. (A.16a) or Eq. (A.18), the matrices $\underset{\approx}{A}_{rp}$ may be found by the technique for scalar coefficients. The inverse Laplace transform of Eq. (A.20) gives the required dispersion matrix,

$$\bar{\underset{\approx}{\Phi}}(t') = e^{\underset{\approx}{A} t'} = \sum_{p=1}^{k} e^{\alpha_p t'} \sum_{r=1}^{m_p} \underset{\approx}{A}_{rp} \frac{t'^{\,r-1}}{(r-1)!} \tag{A.21}$$

It is thus seen that each term in the dispersion matrix generally consists of a sum of products of exponentials and polynominals in t' of degrees one less than the multiplicity of the corresponding characteristic root. However, the existence of multiple roots and its multiplicity m_p indicate the coincidence of m_p tie-points on the dispersion surface of the diffraction problem, a situation which seldom arises. Therefore, the case of distinct characteristic roots is of special interest and in this case Eq. (A.20) reduces to

$$\hat{\underset{\approx}{\Phi}}(s) = \sum_{p=1}^{n+1} \frac{\underset{\approx}{A}_p}{s - \alpha_p} , \tag{A.22a}$$

Where the matrices $\underset{\approx}{A}_p$ are given by

$$\underset{\approx}{A}_p = \lim_{s \to \alpha_p} \frac{\operatorname{adj}(s\underset{\approx}{I} - \underset{\approx}{A})}{|s\underset{\approx}{I} - \underset{\approx}{A}|}(s - \alpha_p) = \frac{\operatorname{adj}(\alpha_p \underset{\approx}{I} - \underset{\approx}{A})}{\prod_{i \neq p} (\alpha_p - \alpha_i)} , \tag{A.22b}$$

and Eq. (A.21) then gives

$$\underset{\approx}{\Phi}(t') = \sum_{p=1}^{n+1} e^{\alpha_p t'} \frac{\mathrm{adj}\,(\alpha_p \underset{\approx}{I} - \underset{\approx}{A})}{\prod_{i \neq p} (\alpha_p - \alpha_i)} \tag{A.23}$$

A.2.3. Method of Eigen-solutions

It is well known from linear algebra that any square matrix A whose elements are real or complex numbers and having distinct eigen-values (which is the case of electron diffraction), there exists a similarity transformation matrix $\underset{\approx}{P}$, called the eigen-vector matrix, which will diagonalize the matrix $\underset{\approx}{A}$ according to

$$\underset{\approx}{\Lambda} = \underset{\approx}{P}^{-1} \underset{\approx}{A} \underset{\approx}{P} , \tag{A.24a}$$

or

$$\underset{\approx}{A} = \underset{\approx}{P} \underset{\approx}{\Lambda} \underset{\approx}{P}^{-1} , \tag{A.24b}$$

where $\underset{\approx}{\Lambda}$ is a diagonal matrix of the form

$$\underset{\approx}{\Lambda} = [\lambda_{ij} \delta_{ij}] . \tag{A.24c}$$

Once the eigenvalue matrix $\underset{\approx}{\Lambda}$ and the eigenvector matrix $\underset{\approx}{P}$ and its inverse $\underset{\approx}{P}^{-1}$ are found, the dispersion matrix is simply given by

$$\underset{\approx}{\Phi}(t - t_0) = e^{\underset{\approx}{A}(t - t_0)} = \underset{\approx}{P}\, e^{\underset{\approx}{\Lambda}(t - t_0)} \underset{\approx}{P}^{-1} , \tag{A.25a}$$

where

$$e^{\underset{\approx}{\Lambda}(t-t_0)} = [\, e^{\lambda_{ii}(t-t_0)}\, \delta_{ij} \,]. \tag{A.25b}$$

It is more convenient to represent the dispersion matrix in the Bloch like wave form

$$\begin{aligned}
\underset{\approx}{\bar{\Phi}}(t) &= e^{\underset{\approx}{A}t} = \underset{\approx}{P}\, e^{\underset{\approx}{\Lambda}t}\, \underset{\approx}{P}^{-1} \\
&= [\, P_{ik} \,]\, [\, e^{\lambda_{kk}t}\, \delta_{k\ell} \,]\, [\, P^{-1}_{\ell j} \,] \\
&= [\, \sum_{\ell} \sum_{k} P_{ik}\, e^{\lambda_{kk}t}\, \delta_{k\ell}\, P^{-1}_{\ell j} \,] \\
&= [\, \sum_{k} P_{ik}\, e^{\lambda_{kk}t}\, P^{-1}_{kj} \,] \\
&= \sum_{k} [\, P_{ik}\, P^{-1}_{kj} \,]\, e^{\lambda_{kk}t}
\end{aligned} \tag{A.26a}$$

For $\underset{\approx}{A}$ symmetric, as is the case for a centro-symmetric crystal, then $\underset{\approx}{P}^{-1} = \underset{\approx}{P}^{T}$, and Eq. (A.26a) becomes

$$\underset{\approx}{\bar{\Phi}}(t) = \sum_{k} [\, P_{ik}\, P_{jk} \,]\, e^{\lambda_{kk}t}, \tag{A.26b}$$

where $\sum_{k} P_{ik} P_{jk}\, e^{\lambda_{kk}t} = \bar{\Phi}_{ij}$ is the ij<u>th</u> element of the dispersion matrix and in which $\Phi^{k}_{ij} = P_{ik} P_{jk}$ is the Bloch like coefficient of

the kth type of wave of the ij th matrix element.

For computing the eigenvalues and the eigenvector matrix of a symmetric matrix $\underset{\approx}{A}$, the Jacobi method is a nature choice for its simplicity and efficiency. The Jacobi method utilizes a series of two dimensional rotations to diagonalize the matrix $\underset{\approx}{A}$. A matrix of the form

$$\underset{\approx}{P}_1 = \begin{array}{c} \begin{bmatrix} 1 & 0 & \cdots & 0 & \cdots & 0 \\ 0 & 1 & \cdots & 0 & \cdots & 0 \\ \vdots & \vdots & \cos\phi_1 & -\sin\phi_1 & \cdots & 0 \\ \vdots & \vdots & \vdots & 1 & \vdots & \vdots \\ \vdots & \vdots & \sin\phi_1 & \cos\phi_1 & \cdots & 0 \\ 0 & 0 & \cdots 0 & \cdots 0 & \cdots & 1 \end{bmatrix} \begin{array}{l} \\ \\ \leftarrow i^{th} \text{ row} \\ \\ \leftarrow j^{th} \text{ row} \\ \\ \end{array} \\ \begin{array}{cccccc} & & i^{th} \text{ column} & j^{th} \text{ column} & & \end{array} \end{array} \tag{A.27a}$$

is used to transform $\underset{\approx}{A}$ into

$$[\lambda_{ij}]' = \underset{\approx}{P}_1^{-1} [a_{ij}] \underset{\approx}{P}_1 \quad . \tag{A.27b}$$

It is easily shown in Eq. (A.27b) that

$$\lambda'_{ii} = \cos^2\phi_1\, a_{ii} + \sin^2\phi_1\, a_{jj} + 2\sin\phi_1 \cos\phi_1\, a_{ij}\,, \tag{A.28a}$$

$$\lambda'_{jj} = \sin^2\phi_1\, a_{ii} + \cos^2\phi_1\, a_{jj} - 2\sin\phi_1\, \cos\phi_1\, a_{ij}\,, \tag{A.28b}$$

$$\lambda'_{ij} = \lambda'_{ji} = -\sin\phi_1 \cos\phi_1 (a_{ii} - a_{jj}) + (\cos^2\phi_1 - \sin^2\phi_1)\, a_{ij}\,; \tag{A.28c}$$

and for other elements in the ith and j th row or column but $k \neq i,j$

$$\lambda'_{ki} = \lambda'_{ik} = \cos\phi_1\, a_{ik} + \sin\phi_1\, a_{jk}\,, \tag{A.28d}$$

$$\lambda'_{kj} = \lambda'_{jk} = \cos\phi_1\, a_{jk} - \sin\phi_1\, a_{ik}\,; \tag{A.28e}$$

and elements not belonging to the i,j th row and column are not effected by this operation. We can put $\lambda'_{ij} = \lambda'_{ji} = 0$ by choosing

$$\tan 2\phi = \frac{2a_{ij}}{a_{ii} - a_{jj}} \tag{A.29}$$

This procedure may be repeated for many times and eventually we may get the diagonalized matrix as the limit of the product of these operations:

$$\underset{\approx}{\Lambda} = \lim_{n \to \infty} \underset{\approx}{P}_n^T \cdots \underset{\approx}{P}_1^T \underset{\approx}{A} \underset{\approx}{P}_1 \cdots \underset{\approx}{P}_n = \underset{\approx}{P}^T \underset{\approx}{A} \underset{\approx}{P} \tag{A.30}$$

In practice, a sufficiently low threshold number may be set for the off-diagonal elements to limit the number of operations necessary for obtaining a good approximation for $\underset{\approx}{\Lambda}$, and then the simultaneously yielded $\underset{\approx}{\Lambda}$ and $\underset{\approx}{P}$ is substituted into Eq. (A.26) to compute the dispersion matrix.

Since the case of a non centro-symmetric crystal is not of much practical interest, methods for diagonalizing a general matrix, such as that of Housholder and that of Given's, are not discussed here.

A.2.4. Comparison of the Methods for Calculating the Dispersion Matrix

Of the three methods for calculating the dispersion matrix, only the series expansion method is so far widely used. It is simple in concept and easy to use but suffering from the lacking of any intermediate step to represent the Bloch wavelike terms and is thus tedious in practice. On the other hand, both the method of Laplace transforms and the method of Eigen-solutions enable the elements of the dispersion matrix to be represented as sums of Bloch like waves. This allows one to calculate any number of desired solutions of different specimen thickness by essentially computing a single set of coefficients for the Bloch like waves (Eq. (A.26)).

The Laplace transform method requires the use of other means to find all the eigenvalues of matrix $\underset{\approx}{A}$, and is hence not the proper method for solving the many beam problems of a centro-symmetric cyrstal. On the other hand, the Jacobi method yields the eigenvalues, the eigenvector matrix and the inverse eigenvector matrix simultaneously. For simple cases (two and three beam cases), the Laplace transform method provides analytical solutions readily.

A.3. The Two-Beam Theory

As an example of application of the methods of solutions (Sec. A.2) and also for use in Chapter II, we develop the two-beam theory in this section. For the two-beam case it is customary to set the origin of the reciprocal space at the first Brillouin zone boundary, g/2. Absorption shall not be considered at this moment. We need $k_{rz} = k_r \cos\theta_B$, $s = g\Delta\theta$, $w = s\,\xi_g$, $k_{ox}^2 = k_r^2 \sin^2(\theta_B + \Delta\theta) \approx g^2/4 + k_r g \Delta\theta = g^2/4 + k_r s$, $k_{gx}^2 = k_r^2 \sin^2(\theta_B + \Delta\theta - 2\theta_B) = g^2/4 - k_r s$,
and hence

$$k_r^2 - k_c^2 = 2k_{rz}(k_{rz} - k_z) + g^2/4 - k_{ox}^2$$
$$= 2k_{rz}(k_{rz} - k_z) - k_r s, \qquad \text{(A.31a)}$$

$$k_r^2 - k_g^2 = 2k_{rz}(k_{rz} - k_z) + g^2/4 - k_{gx}^2$$
$$= 2k_{rz}(k_{rz} - k_z) + k_r s. \qquad \text{(A.31b)}$$

The geometrical relations of the various parameters are shown in Fig. A.1, the dispersion surface (a plot of k_z VS k_x) of the two-beam

0 0 0 0 3 7 0 0 3 8 8

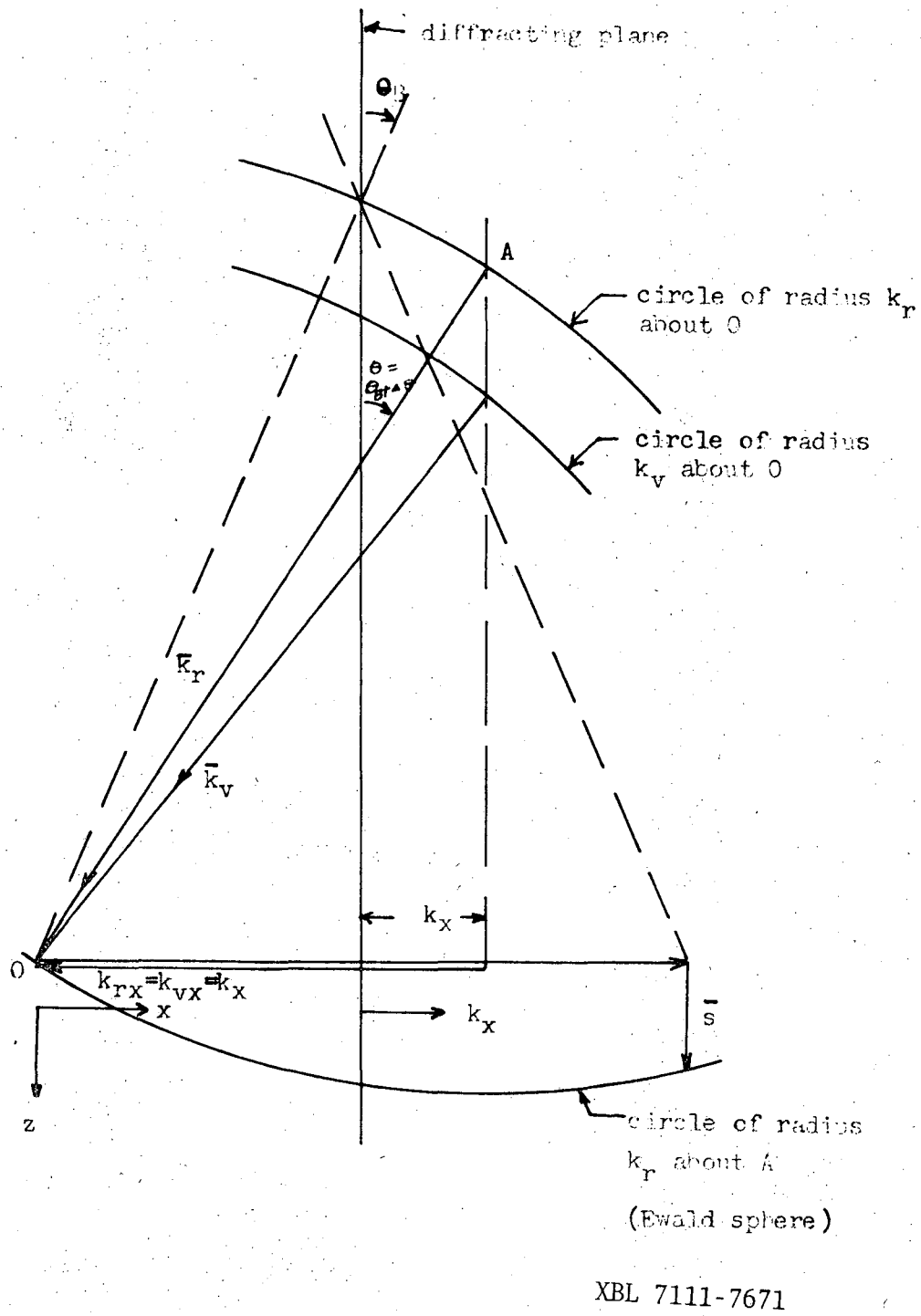

XBL 7111-7671

Fig. A. 1 Geometrical relations between $\bar{k}_v$, $\bar{k}_r$, θ_B, $\Delta\theta$, and s.

case is shown in Fig. A.2. With the use of Eq. (A.31), Eq. (A.6) becomes

$$\frac{d}{dz}\begin{bmatrix}\psi_c(z)\\ \psi_g(z)\end{bmatrix} = 2\pi i\begin{bmatrix}k_{rz}-s/2 & \frac{1}{2\xi_g}\\ \frac{1}{2\xi_g} & k_{rz}+s/2\end{bmatrix}\begin{bmatrix}\psi_c(z)\\ \psi_g(z)\end{bmatrix} \tag{A.32}$$

By letting $t = \pi i z/\xi_g$, $\underset{\sim}{\Phi}(t) = \underset{\sim}{\psi}(t)e^{-2\xi_g k_{rz} t}$, Eq. (A.32) is transformed into

$$\frac{d}{dt}\begin{bmatrix}\phi_c(t)\\ \phi_g(t)\end{bmatrix} = \begin{bmatrix}-w & 1\\ 1 & w\end{bmatrix}\begin{bmatrix}\phi_c(t)\\ \phi_g(t)\end{bmatrix}. \tag{A.33}$$

The Laplace transform of the dispersion matrix reads now

$$\hat{\underset{\approx}{\Phi}}(s) = (s\underset{\approx}{I} - \underset{\approx}{A})^{-1} = \begin{bmatrix}s+w & -1\\ -1 & s-w\end{bmatrix}^{-1}$$

$$= \begin{bmatrix} c_c^1\frac{1}{s+\sqrt{1+w^2}} + c_c^2\frac{1}{s-\sqrt{w^2+1}} & c_g^1\frac{1}{s+\sqrt{1+w^2}} + c_g^2\frac{1}{s-\sqrt{1+w^2}} \\ c_g^1\frac{1}{s+\sqrt{1+w^2}} + c_g^2\frac{1}{s-\sqrt{1+w^2}} & c_c^2\frac{1}{s+\sqrt{1+w^2}} + c_c^1\frac{1}{s-\sqrt{1+w^2}}\end{bmatrix} \tag{A.34a}$$

where

0 0 0 0 3 7 0 0 0 8 9

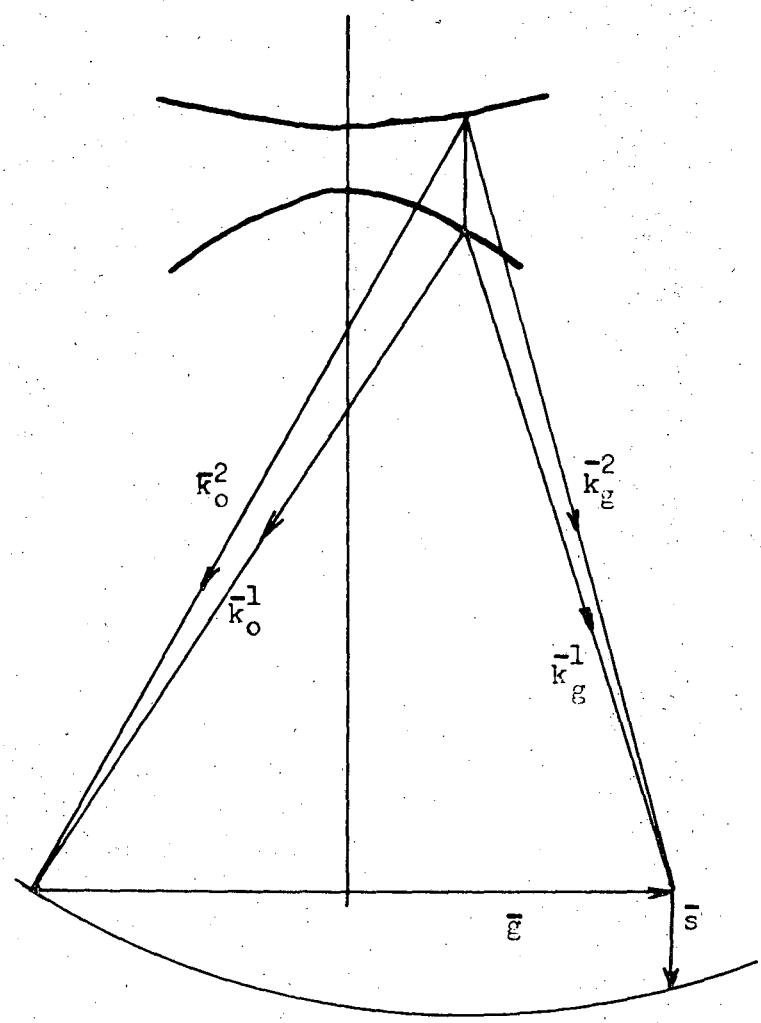

XBL 7111-7672

Fig. A. 2 The two-beam dispersion surface and the wave vectors of the four excited waves in the crystal.

$$c_c^1 = \frac{1}{2}\left(1 + \frac{\omega}{\sqrt{1+\omega^2}}\right), \quad c_c^2 = \frac{1}{2}\left(1 - \frac{\omega}{\sqrt{1+\omega^2}}\right),$$

$$-c_g^1 = c_g^2 = \frac{1}{2}\frac{1}{\sqrt{1+\omega^2}} \tag{A.34b}$$

The dispersion matrix is then

$$\underset{\approx}{\bar{\Phi}}(t - t_c) = \begin{bmatrix} c_c^1 \phi^1(t-t_c) + c_c^2 \phi^2(t-t_c) & c_g^1 \phi^1(t-t_c) + c_g^2 \phi^2(t-t_c) \\ c_g^1 \phi^1(t-t_c) + c_g^2 \phi^2(t-t_c) & c_c^2 \phi^1(t-t_c) + c_c^1 \phi^2(t-t_c) \end{bmatrix} \tag{A.35a}$$

where $\phi^1(t-t_c) = \exp\left[-\sqrt{1+\omega^2}(t-t_c)\right]$,

$$\phi^2(t-t_c) = \exp\left[\sqrt{1+\omega^2}(t-t_c)\right]. \tag{A.35b}$$

Upon transforming back to the $\underset{\sim}{\psi}$ representation, the dispersion matrix becomes

$$\underset{\approx}{\bar{\Psi}}(z-z_c) = \begin{bmatrix} c_c^1 \psi^1(z-z_c) + c_c^2 \psi^2(z-z_c) & c_g^1 \psi^1(z-z_c) + c_g^2 \psi^2(z-z_c) \\ c_g^1 \psi^1(z-z_c) + c_g^2 \psi^2(z-z_c) & c_c^2 \psi^1(z-z_c) + c_c^1 \psi^2(z-z_c) \end{bmatrix}, \tag{A.36}$$

where

$$\psi^1(z-z_0) = \exp\left[k_z^1 \cdot (z-z_0)\right], \tag{A.37a}$$

$$\psi^2(z-z_0) = \exp\left[k_z^2 \cdot (z-z_0)\right]. \tag{A.37b}$$

In Eq. (A.37), the quantities

$$k_z^1 = k_{rz} - \sqrt{1+w^2}/2\xi_g, \tag{A.38a}$$

$$k_z^2 = k_{rz} + \sqrt{1+w^2}/2\xi_g, \tag{A.38b}$$

are the wave vectors of the type I and type II waves respectively. The wave functions of the transmitted and the diffracted beams are simply given by

$$\psi_0(z) = C_0^1\,\psi^1(z) + C_0^2\,\psi^2(z), \tag{A.39a}$$

$$\psi_g(z) = C_g^1\,\psi^1(z) + C_g^2\,\psi^2(z), \tag{A.39b}$$

respectively. The so-called type I and type II waves are respectively defined as

$$\psi_I(\bar{r}) = \left[c_0^1 e^{2\pi i k_x x} + c_g^1 e^{2\pi i (k_x + g) x} \right] \psi^1(z) \tag{A.40a}$$

$$\psi_{II}(\bar{r}) = \left[c_0^2 e^{2\pi i k_x x} + c_g^2 e^{2\pi i (k_x + g) x} \right] \psi^2(z). \tag{A.40b}$$

When Bragg condition is exactly satisfied, i.e., W = 0 and $\bar{k}_x = -\bar{g}/2$, Eq. (A.40) is reduced to

$$\psi_I(\bar{r}) = \sin \pi g x \; e^{2\pi i (k_z^1 z - 1/4)} \tag{A.41a}$$

$$\psi_{II}(\bar{r}) = \cos \pi g x \; e^{2\pi i k_z^2 z} \; . \tag{A.41b}$$

Eq. (A.41) shows that the two types of waves are waves progating in the z-direction with different kinetic energy and, along x-direction, they form standing pattern with type II waves centered at each lattice plane and type I waves in between the lattice planes, as illustrated in Fig. A.3 for the quantities $\psi_I \psi_I^*$ and $\psi_{II} \psi_{II}^*$. Identical to that of the energy gaps in band theory, the origin of the energy difference is Bragg reflection. In the band theory of bound electrons, initially all electrons must have same kinetic energy so that Bragg condition may be

0 0 0 0 3 7 0 3 0 9 1

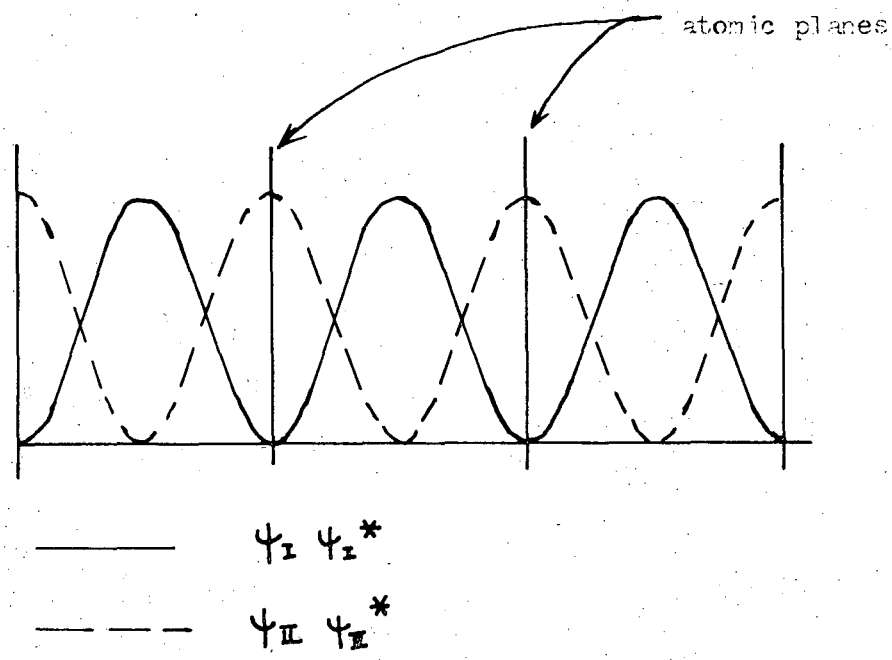

XBL 7111-7673

Fig. A. 3 Intensity distributions of the two types of waves: that of the type II waves are centered at the atomic planes whereas that of the type I waves are centered in between the atomic planes.

satisfied, and because of the two resulting standing waves are centered either at or in between the reflecting planes, the potential energy and hence the total energy of the two types of electrons are different. In the case of electron diffraction, however, all electrons entering the crystal from vacuum with same energy. Since the total energy must be conserved, thus, bcause the type II electrons are centered at the lattice planes and hence having a lower potential energy, their kinetic energy is consequently larger than that of the type I electrons. Notice that all electrons in the crystal possess a somewhat higher kinetic energy than in the vacuum, because the crystal potential is negative.

Absorption can be included in the two-beam case by replacing the potential V_g by $V_g + iV_g'$, and hence

$$k_r \rightarrow k_r + \frac{i U_0'}{2 k_r} , \tag{A.42a}$$

$$k_z^1 = k_{rz} - \frac{1}{2\xi_g}\sqrt{1+w^2} + i\left(\frac{1}{2\xi_0'} - \frac{1}{2\xi_g\sqrt{1+w^2}}\right), \tag{A.42b}$$

$$k_z^2 = k_{rz} + \frac{1}{2\xi_g}\sqrt{1+w^2} + i\left(\frac{1}{2\xi_0'} + \frac{1}{2\xi_g\sqrt{1+w^2}}\right). \tag{A.42c}$$

In Eq. (A.42), the quantities

$$\xi_c' = k_{rz} / U_c' , \tag{A.43a}$$

$$\xi_g' = k_{rz} / U_g' , \tag{A.43b}$$

are respectively the "mean" and "anomalous" absorption lengths. The absorption coefficients associated with the type I and type II waves are in turn defined as

$$\mu^1 = \frac{1}{\xi_c'} - \frac{1}{\xi_g' \sqrt{1+w^2}} , \tag{A.43c}$$

$$\mu^2 = \frac{1}{\xi_c'} + \frac{1}{\xi_g' \sqrt{1+w^2}} . \tag{A.43d}$$

The physical meaning of the absorption lengths are straight-forward: the inverse of ξ_c' is the measure of the average absorption power, and the inverse of ξ_g' is the measure of the Fourier coefficient of the absorption power associated with $\bar{g}$. It is obvious from Eqs. (A.43c) and (A.43d) that as w increases, the difference between the absorption coefficients μ^1 and μ^2 decreases. This is so because as w increases, more of the type II waves would be channeled between the atomic planes and more of the type I waves would be moved to the atomatic planes where the absorption power is by far the largest. To be physically realizable, the

relation $\xi_g > \xi_0'$ must hold.

A.4. Dynamical Multiple Rescattering Process of Electron Diffractions-- An Interpretation from the Dispersion Matrix

The Bloch wave type of solutions of the diffraction problem implies that the electrons in the crystal are actually undergoing a dynamical rescattering process in the sense that the electrons propagating in one direction are constantly rescattered into other directions and vise versa. This rescattering is accomplished by the process of having the electrons of a tie-point on any one particular branch of the dispersion surface constantly rescattered into all other branches of the dispersion surface in all directions (including the direction these electrons originally were propagating) and vice versa. This process of multiple rescattering represents a possible way of interpreting the diffraction problem, which can best be understood with the use of the dispersion matrix. In fact, the various terms in the dispersion matrix describes specifically the amplitude, direction, and branch of the dispersion surface of the rescattering of one particular wave.

To illustrate this process, consider the two-beam case. The solution of the diffraction problem at any thickness $z + \Delta z$ may be expressed as the product of the dispersion matrix of argument Δz with the solution at z, i.e.,

$$\begin{bmatrix} \psi_0(z+\Delta z) \\ \psi_g(z+\Delta z) \end{bmatrix} = \begin{bmatrix} \psi_0(\Delta z) & \psi_g(\Delta z) \\ \psi_g(\Delta z) & \psi_0^{+}(\Delta z) \end{bmatrix} \begin{bmatrix} \psi_0(z) \\ \psi_g(z) \end{bmatrix} . \qquad (A.44)$$

When writing out in explicit form , Eq. (A.44) becomes

$$\begin{aligned}\psi_c(z+\Delta z) = {} & (C_c^1)^2\,\psi^1(z+\Delta z) + C_c^1\,C_c^2\,\psi^2(z)\,\psi^1(\Delta z) \\ & + C_c^1\,C_c^2\,\psi^1(z)\,\psi^2(\Delta z) + (C_c^2)^2\,\psi^2(z+\Delta z) \\ & + (C_g^1)^2\,\psi^1(z+\Delta z) + C_g^1\,C_g^2\,\psi^2(z)\,\psi^1(\Delta z) \\ & + C_g^1\,C_g^2\,\psi^1(z)\,\psi^2(\Delta z) + (C_g^2)^2\,\psi^2(z+\Delta z)\,,\end{aligned} \tag{A.45a}$$

and a similar expression for $\psi_g(z + \Delta z)$. The physical meaning of Eq. (A.45a) is that ψ_o at a thickness $z + \Delta z$ is due to the multiple rescattering of both types of waves of ψ_o and ψ_g at z: on the right hand side of Eq. (A.45a), the first term is due to the type I wave of $\psi_o(z)$ scattered into type I wave of $\psi_o(z + \Delta z)$, the second term is due to type II wave of $\psi_o(z)$ scattered into type I wave of $\psi_o(z + \Delta z)$, etc., and the 5th to 8 th terms are due to $\psi_g(z)$. A similar situation holds true for $\psi_g(z + \Delta z)$. Notice that for the case of a perfect crystal, Eq. (A .45a) is simply

$$\psi_c(z+\Delta z) = C_c^1\,\psi^1(\Delta z+z) + C_c^2\,\psi^2(z+\Delta z)\,, \tag{A.45b}$$

i.e., the rescattering process is as if the different types of waves are propagating independently. Nevertheless, this does not mean that there is no mutual scattering among the different types of waves, but rather that the effect of mutual scatteing is merely balanced out, i.e., the

amount of electrons scattered from type I waves into type II waves is exactly equal to the amount of electrons scattered into type I waves from type II waves, thus there is no net transfer of electrons between the two types of waves. In this sense, the so-called intra-band transition is forbidden. If the crystal is deformed, however, then this situation is not true anymore, and images of the deformation will be produced.

A second important characteristic of the dispersion matrix is, as shown in Chapter II, that it is the Green's function in problems where inelastic scatterings are involved.

A.5. Image Problems

A more important area of the diffraction problem lies in the study of images produced by defects in the crystals. All crystalline matters contain certain kinds of defects, e.g., dislocations, stacking faults, twins, small precipitates, grain boundaries, etc. These defects are important in determining the properties of the materials.

In a distorted crystal the electron wave function must still satisfy the Schrödinger equation; however, the crystal potential in this case is no longer that of the perfect crystal. Suppose the defect is produced by a deformation of the lattice of a perfect crystal which moves the atom at lattice point point $\bar{d}$ to $\bar{d} + \bar{R}(\bar{d})$, then the potential at an arbitrary point $\bar{d}'$ is changed since it now depends on $\bar{d}' - \bar{d}$. If the crystal deforms smoothly, the potential at $\bar{d}'$ will then in fact change from $V(\bar{r})$ to $V(\bar{r}-\bar{R}(\bar{r}))$. The potential in the deformed crystal can be written formally as a Fourier series:[49]

0 0 0 0 3 7 0 0 0 9 4

$$V(\bar{r}) = \frac{h^2}{2me} \sum_g U_g \exp(-2\pi i \bar{g}\cdot\bar{R}(\bar{r})) \exp(2\pi i \bar{g}\cdot\bar{r}). \qquad (A.46)$$

It is seen in Eq. (A.46) that the crystal distortion has the effect of modifying (the Fourier coefficients of) the crystal potential by multiplying the original constant U_g by a phase factor $\exp(-2\,\bar{g}.\bar{R}(\bar{r}))$. It can be shown, provided $\bar{R}(\bar{r})$ varies only slowly with $\bar{r}$ (in fact, provided $\bar{R}(\bar{r})$ does not change significantly in a lattice distance), the Bloch wave type of solutions of the diffraction problem still hold. Except for certain particular cases, the problem will have to be solved numerically, the methods discussed so far may be directly applied to crystals containing defects, provided the modified crystal potential is used.

The differential equations for the case of a deformed crystal may be easily derived by using the modified lattice potential, Eq. (A.46), in Eq. (A.1) and assuming a set of modified Bloch wave solutions:

$$\psi_h(\bar{r}) = \sum_h C_h(\bar{r})\, e^{2\pi i \bar{k}_h\cdot\bar{r}} . \qquad (A.47)$$

We then have

$$k_z C_h - \frac{i}{2\pi}\frac{\partial C_h}{\partial z} = (k_r + S_h) + \sum_{\bar{g}\neq\bar{h}} \frac{e^{-2\pi i(\bar{g}\cdot\bar{r}-\bar{h}\cdot\bar{r})}}{2\,\xi_{\bar{h}-\bar{g}}} C_g$$

$$+ \frac{i}{2\pi k_r}\left(k_x\frac{\partial C_h}{\partial x} + k_y\frac{\partial C_h}{\partial y}\right) + \frac{\nabla^2 C_h}{8\pi^2 k_r} . \qquad (A.48)$$

If the last terms involving $\frac{\partial}{\partial x}$, $\frac{\partial}{\partial y}$, ∇^2 of $C_h(\bar{r})$ are neglected (the column approximation), then Eq. (A.48) becomes

$$\frac{\partial \psi_h}{\partial z} = 2\pi i \left\{ (k_r + S_h)\psi_h + \sum_{\bar{g} \neq \bar{h}} \frac{e^{2\pi i(\bar{h}-\bar{g})\cdot\bar{r}}}{2\xi_{\bar{h}-\bar{g}}} \psi_g \right\}. \tag{A.49}$$

An equivalent but more general formulation of the image problems has been given by Howie and Basinski,[50] in which they included the non-column approximations. On writing out in the matrix form, and adapting the transformations given in Eq. (A.7), Eq.(A.59) becomes

$$\frac{d}{dt}\begin{bmatrix} \phi_0(t) \\ \phi_{g_1}(t) \\ \vdots \\ \phi_{g_n}(t) \end{bmatrix} = \begin{bmatrix} 2W_0 & \xi'_{1(-1)} e^{2\pi i \bar{g}_1\cdot\bar{R}} & \cdots & \xi'_{1(-n)} e^{2\pi i \bar{g}_n\cdot\bar{r}} \\ \xi'_{11} e^{-2\pi i \bar{g}_1\cdot\bar{R}} & 2W_1 & \cdots & \\ \vdots & & & \\ \xi'_{1n} e^{-2\pi i \bar{g}_n\cdot\bar{R}} & & \cdots & 2W_n \end{bmatrix} \begin{bmatrix} \phi_0(t) \\ \phi_{g_1}(t) \\ \vdots \\ \phi_{g_n}(t) \end{bmatrix}, \tag{A.50a}$$

or, in vectorial form

$$\frac{d}{dt} \underset{\sim}{\phi}(t) = \underset{\approx}{A}_R \underset{\sim}{\phi}(t) \tag{A.50b}$$

0 0 0 0 3 7 0 0 0 9 5

The solution of the many beam problem of a deformed crystal may again, in principle, be written as

$$\underset{\sim}{\phi}(t) = \underset{\approx}{\Phi}_R(t-t_c)\,\underset{\sim}{\phi}(t_c), \tag{A.51}$$

where $\underset{\approx}{\Phi}_R(t-t_o)$ is the dispersion matrix and is a function of $\bar{R}(\bar{r})$. In contrary to the case of a perfect crystal, there is now no known method for calculating $\underset{\approx}{\Phi}_R(\Delta t)$ in general. The type of expression

$$\underset{\approx}{\Phi}_R(\Delta t) = e^{\underset{\approx}{A}_R \Delta t} \tag{A.52}$$

is valid only if $\bar{R}$ is constant throughout the interval, Δt, considered. Thus, the image problems can best be solved for each slice of the crystal within which $\bar{R}(t)$ can be approximated as a constant. To have any accuracy at all, however, this procedure then requires an unwarranted large amount of computing time. For this reason, it is a usual practice that Eq. (A.52) is approximated as

$$\underset{\approx}{\Phi}_R(\Delta t) = e^{\underset{\approx}{A}_R \Delta t} = \underset{\approx}{I} + \underset{\approx}{A}_R \Delta t. \tag{A.53}$$

It is also usually thought that the matrix $\underset{\approx}{A}_R$ is cumbersome, (since there is an exponential term $\exp(2\pi i\bar{g}.\bar{R})$ associated with each off-diagonal term of the matrix) and it is therefore transformed into

$$\underset{\approx}{A}'_R = \begin{bmatrix} 2\omega_c & \xi'_{1(-1)} & \cdots & \xi'_{1(-n)} \\ \xi'_{11} & 2\omega_1 + \frac{d}{dt}\bar{g}_1 \cdot \bar{R} & \cdots & \\ \vdots & | & & \\ \xi'_{1n} & \cdots & \cdots & 2\omega_n + \frac{d}{dt}\bar{g}_1 \cdot \bar{R} \end{bmatrix}, \tag{A.54a}$$

by substitution of

$$\Phi'_h(\bar{r}) = \Phi_h(\bar{r})\, e^{-2\pi i \bar{h}\, \bar{R}}, \tag{A.54b}$$

in Eq. (A.50b), to find[51]

$$\frac{d}{dt}\underset{\sim}{\Phi}' = \underset{\approx}{A}'_R\, \underset{\sim}{\Phi}'. \tag{A.54c}$$

The approximate dispersion matrix of the type of Eq. (A.53) may now be used to obtain an incremental solution

$$\begin{aligned} \underset{\sim}{\Phi}'(t+\Delta t) &= (\underset{\approx}{I} + \underset{\approx}{A}'_R \Delta t)\, \underset{\sim}{\Phi}'(t) \\ &= \underset{\sim}{\Phi}'(t) + \Delta \underset{\sim}{\Phi}'(\Delta t) \\ &= \Phi'(t) + \left[\underset{\approx}{A}'_R \cdot \underset{\sim}{\Phi}\, \Delta t\right]_{\text{corrected}}. \end{aligned} \tag{A.55}$$

By applying various numerical integration methods, the incremental wave function, $\Delta \underset{\sim}{\phi}'(\Delta t)$, may be corrected for the sake of accuracy (the last term on the right hand side of Eq. (A.55) indicates this operation). We shall refer this method as the direct-integration method. Upon iterating through the crystal, this method either yields results with low accuracy or requires a large amount of computing time. Independent of the numerical integration method chosen, this method suffers from an inherent difficulty which limits the usable integration interval, Δt, to extremely small values, if any reasonable accuracy is desired. For a many beam problem, the deviation parameters W_h can be a very large number, this causes the introduction of a non-negligible amount of integration error in each step. Depending upon the value of Δt chosen this will usually lead to an electron intensity non-conservation phenomenon in the results (aside from those due to absorption). This difficulty can be overcome by using smaller values of Δt (but the computing time needed is then necessarily lengthened, especially for problems involving a large number of beams). Another difficulty associated with the use of Eq. (A.54) is that the term $\frac{d}{dt}\bar{g}\cdot\bar{R}$ becomes a δ-function on crossing slices with an abrupt change in $\bar{R}$ (e.g., stacking faults, anti-phase boundaries, etc.). This second difficulty can be avoided by using Eq. (A.50) instead of Eq. (A.54).

We shall now derive a method which retains the full mathematical rigor of the method of eigen-solutions and which completely eliminates the intensity non-conservation problem. This approach utilizes a special property of the matrix $\underset{\approx}{A}_R$: that the eigenvalues of $\underset{\approx}{A}_R$ are independent of $\bar{R}$ and are just those of the $\underset{\approx}{A}$ matrix of the perfect crystal. Based

on this property, we can calculate the dispersion matrix of each slice from that of the perfect crystal, which in turn is readily obtained by the eigen-solution method given in section A.2.3. The dispersion matrix thus obtained is identical to that calculated directly from the matrix $\underset{\approx}{A}_R(t)$.

Notice that the matrix $\underset{\approx}{A}_{\bar{R}}$ in Eq. (A.50) may be written as

$$\underset{\approx}{A}_R = \underset{\approx}{Q}_R^{-1} \, \underset{\approx}{A}_{R=0} \, \underset{\approx}{Q}_R \, . \tag{A.56}$$

where $\underset{\approx}{Q}_R$ is a similarity transformation matrix given by

$$\underset{\approx}{Q}_R = \left[e^{2\pi i \, \bar{g}_{p-1} \cdot \bar{R}} \, \delta_{pr} \right] , \tag{A.57a}$$

and it follows that $Q_{\bar{R}}^{-1}$ is given by

$$\underset{\approx}{Q}_R^{-1} = \left[e^{-2\pi i \, \bar{g}_{p-1} \cdot \bar{R}} \, \delta_{pr} \right] . \tag{A.57b}$$

In Eq. (A.56) $\underset{\approx}{A}_{R=0}$ is simply the $\underset{\approx}{A}$ matrix of the perfect crystal. It is immediately seen from Eq. (A.56) that

$$\begin{aligned} \det. \left(\underset{\approx}{A}_R - \lambda \underset{\approx}{I} \right) &= \det. \left(\underset{\approx}{Q}_R^{-1} \underset{\approx}{A}_{R=0} \underset{\approx}{Q}_R - \lambda \underset{\approx}{I} \right) \\ &= \det. \left\{ \underset{\approx}{Q}_R^{-1} \left[\underset{\approx}{A}_{R=0} - \lambda \underset{\approx}{I} \right] \underset{\approx}{Q}_R \right\} \\ &= \det. \left(\underset{\approx}{A}_{R=0} - \lambda \underset{\approx}{I} \right) . \end{aligned} \tag{A.58}$$

Eq. (A.58) means that the eigenvalues of the system are independent of $\bar{R}$ and are just those of the perfect crystal. However, when $\bar{R}$ changes, the corresponding eigenvectors must be changed according to $\underset{\approx}{Q}_{\bar{R}}$. The physical interpretation of this property is straight-forward: since the deformable ion approximation amounts only to a shifting of the lattice planes by an amount $\bar{R}$, but not any other physical properties, thus the characteristic modes of excitation (correspond to the eigenvalues of $\underset{\approx}{A}_{\bar{R}}$) are not effected by this shifting. However, the excitation strength of the modes (corresponds to the eigenvectors) is changed as described by $\underset{\approx}{Q}_{\bar{R}}$.

Although Eqs. (A.50) and (A.54) are mathematically equivalent, however, if the two equations are interpreted from the point of view of an incremental solution, there is an apparently different physical meaning associated with each equation. Equation (A.50) describes the influences of changing $\bar{R}$ as simple shifting of lattice planes and thereby changing only the excitation strength of each mode from slice to slice, but not any other physical properties. On the other hand, Eq. (A.54) describes the situation as a twisting as well as a shifting of lattice planes, therefore, the operational reciprocal lattice vectors will vary their directions, magnitudes, and hence the modes of excitation as well as the excitation strength of each mode. This situation is illustrated in Fig. A.5 in the dispersion surface representation of a two-beam case.

The dispersion matrix of a slice in which $\bar{R} = \bar{R}_m$, a constant, is given by

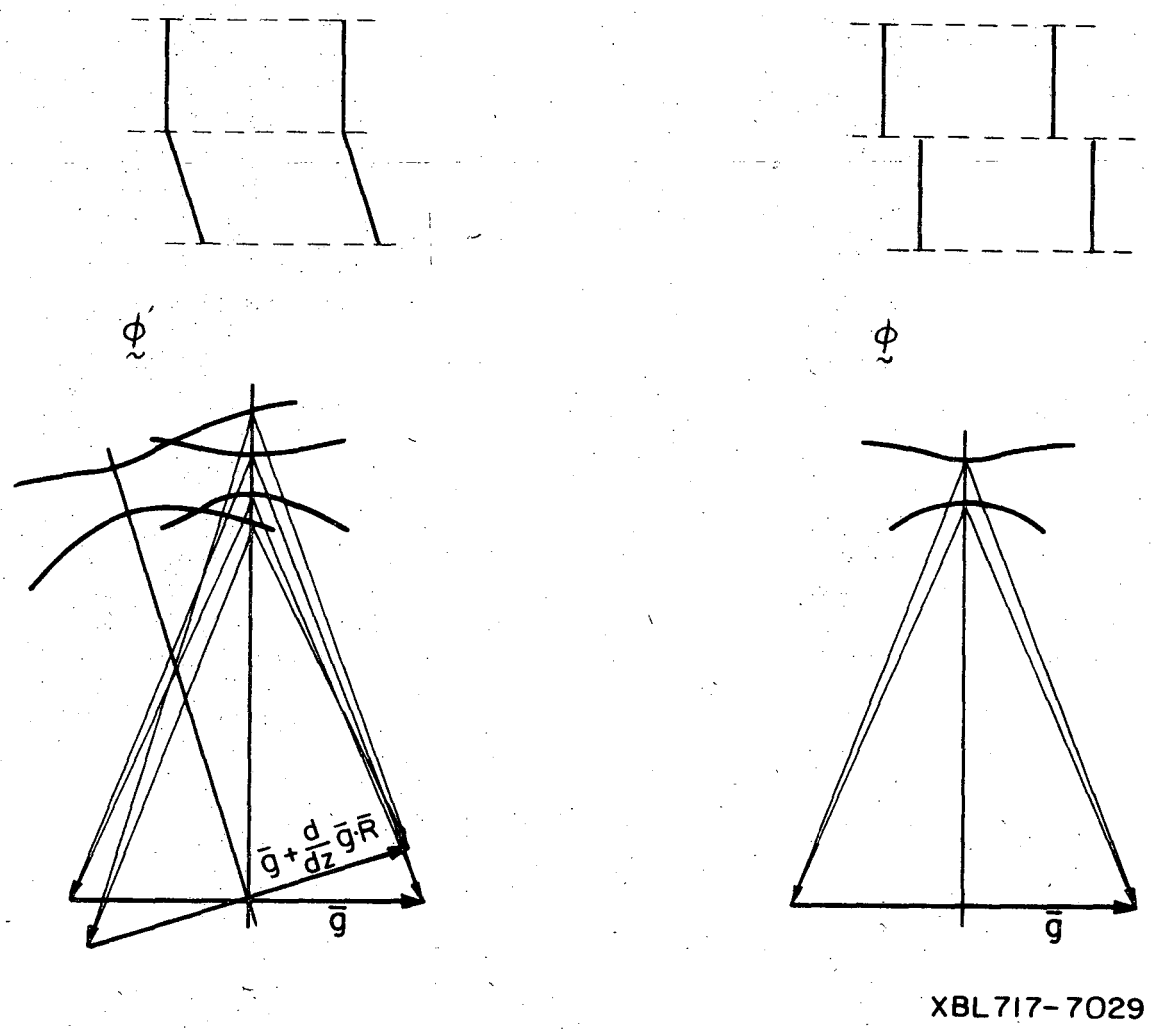

Fig. A. 4 Physical interpretations of the two mathematically equivalent representations of the image problems: (a) in $\underset{\sim}{\Phi}'$ representation (Eq. (A.54)), the lattice planes are twisting and shifting through the crystal, $\bar{g}$ changes direction and magnitude and hence the dispersion surface and all Bloch amplitudes; (b) in $\underset{\sim}{\Phi}$ representation (Eq. (A.50)), the lattice planes were only shifted, nothing but the Bloch amplitudes are changed.

$$\bar{\underset{\approx}{\Phi}}_{R_m}(\Delta t) = \underset{\approx}{Q}_{R_m}^{-1} \, e^{A_{R=0}\Delta t} \, \underset{\approx}{Q}_{R_m}$$

$$= \underset{\approx}{Q}_{R_m}^{-1} \, \bar{\underset{\approx}{\Phi}}_{R=0}(\Delta t) \, \underset{\approx}{Q}_{R_m} . \qquad \text{(A.59)}$$

The waves leaving one slice of thickness Δt with displacement $\bar{R}_m$ is obtained by multiplying the dispersion matrix by the waves entering this slice. Upon iterating through the crystal, this procedure results in

$$\underset{\sim}{\Phi}(t) = \left\{ \prod_{\ell=1}^{n} \left[\underset{\approx}{Q}_{R_\ell}^{-1} \bar{\underset{\approx}{\Phi}}(\Delta t) \, \underset{\approx}{Q}_{R_\ell} \right] \right\} \underset{\sim}{\phi}(0) . \qquad \text{(A.60)}$$

The dispersion matrix of the whole crystal is readily identified from Eq. (A.60) as

$$\bar{\underset{\approx}{\Phi}}_{R}(t) = \prod_{\ell=1}^{n} \left[\underset{\approx}{Q}_{R_\ell}^{-1} \, \bar{\underset{\approx}{\Phi}}_{R=0} \, \underset{\approx}{Q}_{R_\ell} \right] . \qquad \text{(A.61)}$$

The right hand side of Eq. (A.61) is called the Product Integral of Volterra. For problems with a discrete type of boundary (stacking faults, anti-phase boundaries, etc.), Eq. (A.61) is readily computed by a few matrix multiplications.

For problems with continuous displacements, e.g., that of a dislocation, the product integral cannot be so readily computed. It is unfortunate at this stage that numerical methods for computing this integral is not well developed, thus if $\underset{\sim}{\Phi}$ is calculated according to Eq. (A.60), either large amount of computing time is required or accuracy of the results must be sacrificed. Nevertheless, this procedure may be

modified slightly so that the dispersion matrix may be used in conjunction with ordinary integration methods to obtain the final results. Since all numerical integration methods are designed to compute an incremental solution of the type

$$\underset{\sim}{\phi}(t+\Delta t) = \underset{\sim}{\phi}(\Delta t) + \left[\Delta \underset{\sim}{\phi}(\Delta t)\right]_{\text{corrected}} \tag{A.62}$$

we shall try to find an $\Delta \underset{\sim}{\phi}_h(\Delta t)$ in which the dispersion matrix is fully utilized, and this is simply

$$\Delta \underset{\sim}{\phi}(\Delta t) = \left[\underset{\approx}{\bar{\Phi}}_R(\Delta t) - \underset{\approx}{I}\right] \underset{\sim}{\phi}(t). \tag{A.63}$$

where $\underset{\approx}{\bar{\Phi}}_R(\Delta t)$ is given by Eq. (A.59). The computational step given by Eq. (A.63) is necessary since numerical intergation methods amount only to correct the incremental quantity $\Delta \underset{\sim}{\phi}(\Delta t)$ at each step, and after the correction is accomplished numerically according to the method chosen, the wave functions leaving for the next step is then simply given by that of Eq. (A.62).

An example of a screw dislocation is given in Fig. A.5, where the eigen-integration method refers to the method just discussed. For Δt fixed, both the eigen-integration and the direct integration method require about the same amoutn of computing time if many columns are involved. The integration routine used is the 4 th order Runge-Kutta method. Over the wide range of slice thicknesses chosen, it is clearly seen that the eigen-integration method yields a result far more stable and accurate than the direct integration method. No noticable intensity

0 0 0 0 3 7 0 0 0 9 9

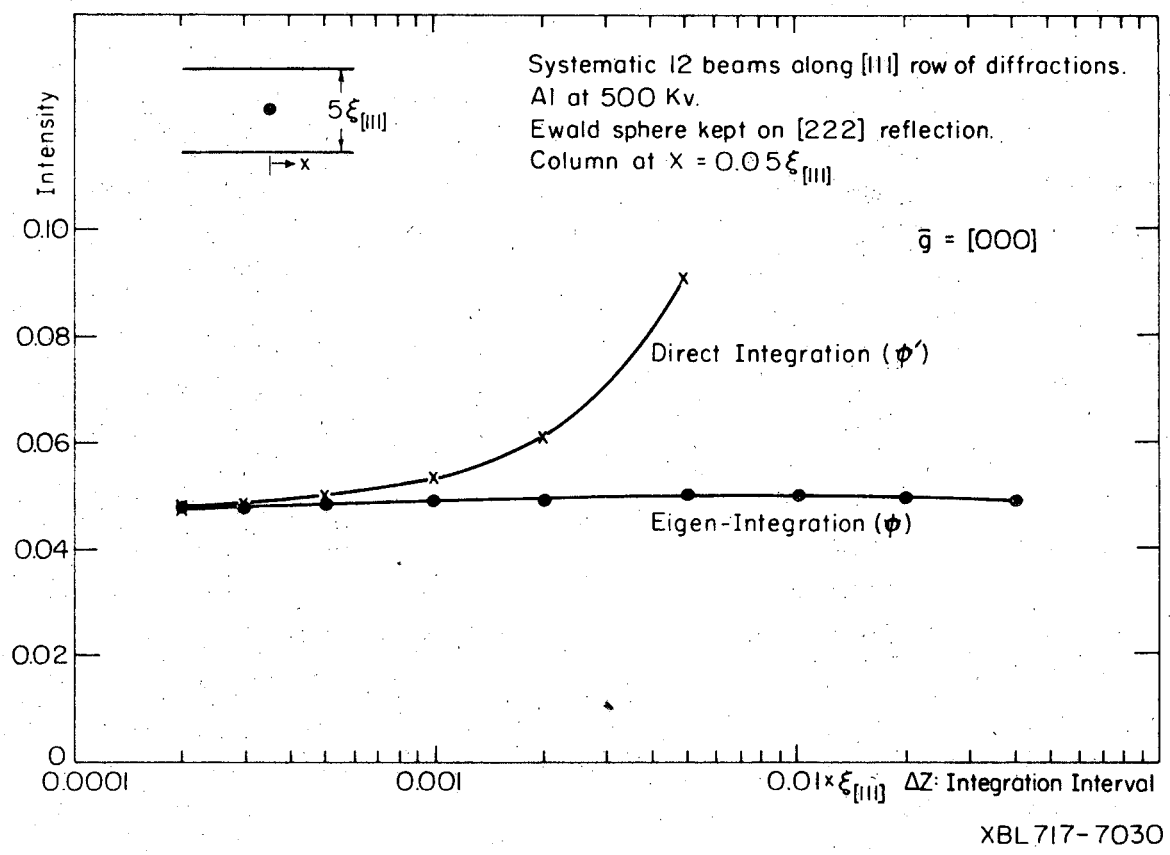

Fig. A. 5a

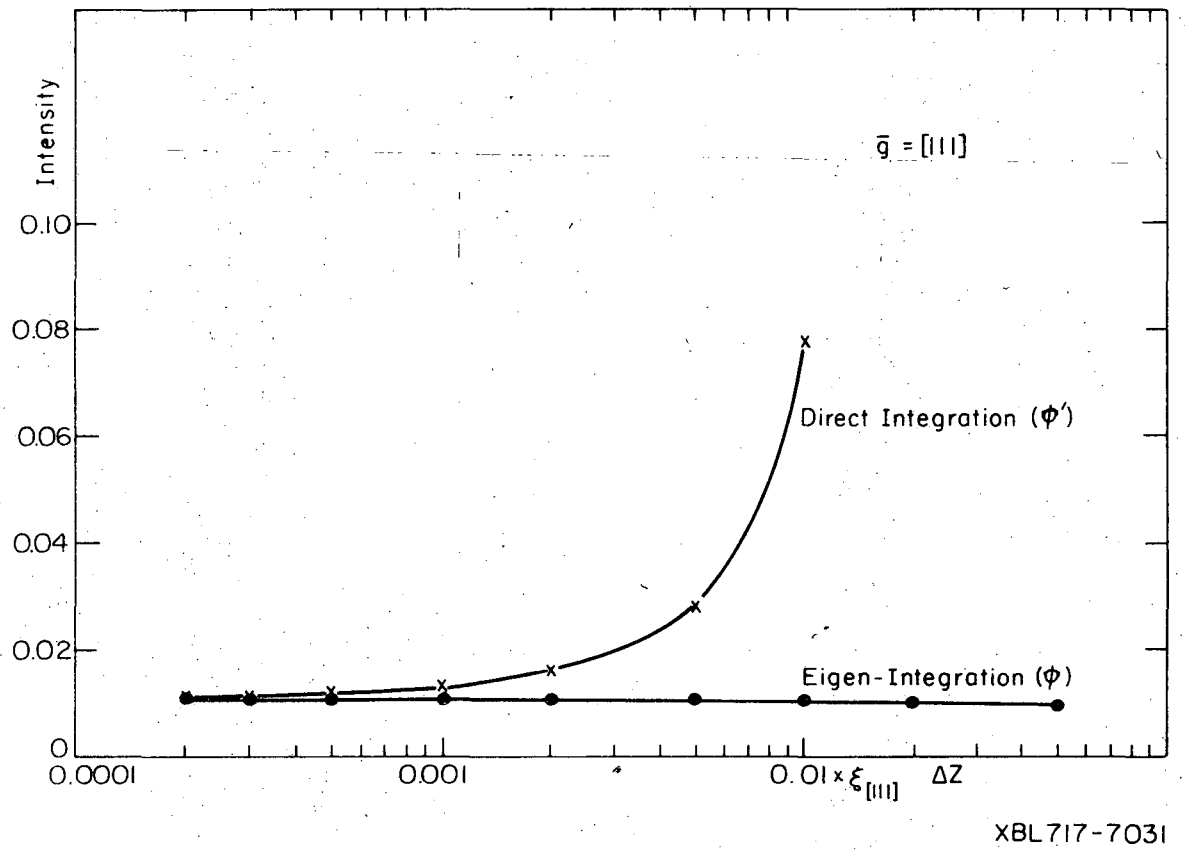
Intensity
0.10
0.08
0.06
0.04
0.02
0
0.0001
0.001
0.01 × ξ[111]
ΔZ
ḡ = [111]
Direct Integration (Φ′)
Eigen-Integration (Φ)
XBL717-7031

Fig. A. 5b

0 0 0 0 3 7 0 0 1 0 0

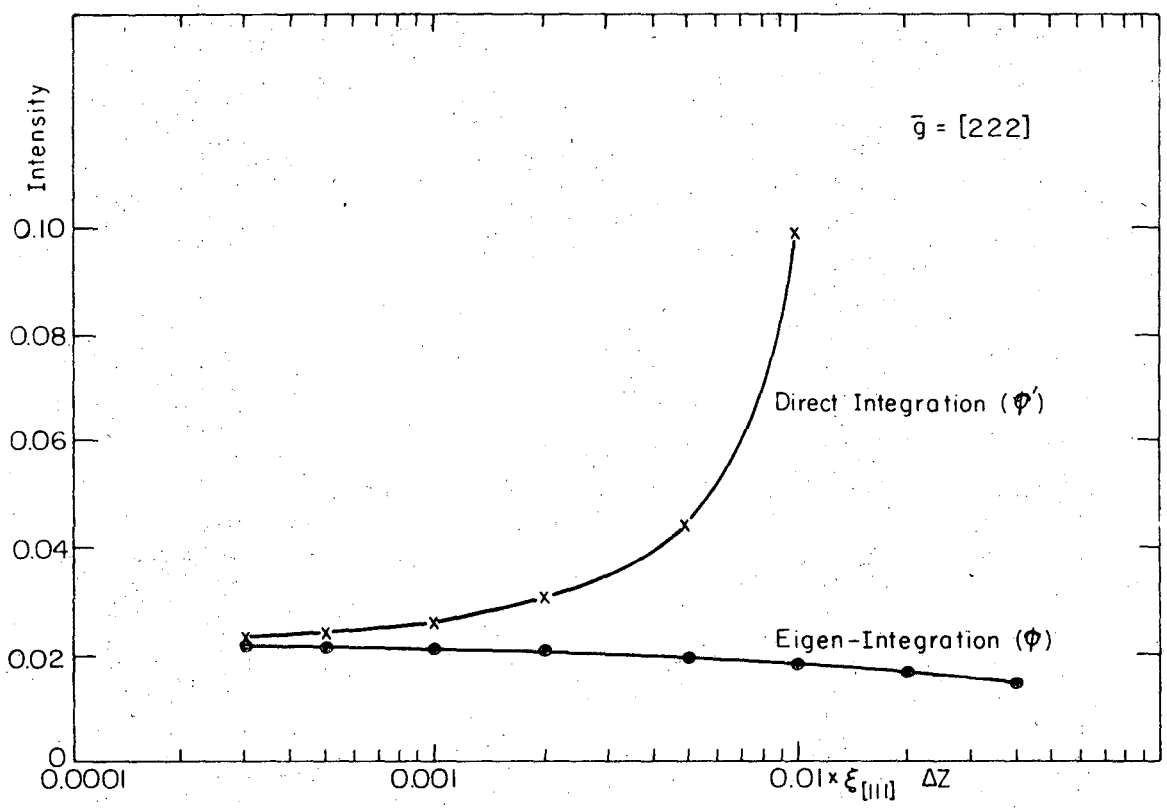

XBL717-7032

Fig. A. 5c

Comparison of computed intensities of the three strongest beams of one column of a screw dislocation image using two different methods. The eigen-integration method (applied to $\underset{\sim}{\Phi}$, Eq. (A.50)) yields more accurate result than the direct integration method (applied to $\underset{\sim}{\Phi}'$, Eq. (A.54)). When integration interval becomes large, results obtained by using eigen-integration method do not show serious intensity non-conservation problem, whereas that by direct integration do. Integration routine used is fourth order Runge-Kutta.

non-conservation is introduced by the former method while the latter method suffers from this problem severely when Δt is large. This is so, because the eigen-integration method uses the dispersion matrix fully while the direct integration method uses only a first order approximation of the dispersion matrix. This means that the eigen-integration method should yield highly accurate results even when the Δt is large, because for this method, errors introduced in the integration process can only come from one variable: $\bar{R}$.

0 0 0 0 3 7 0 0 1 0 1

ACKNOWLEDGMENT

The author wishes to express his gratitude to Professor Gareth Thomas for his guidance and encouragement, and to Professor Walter L. Bell for his many helpful discussions and suggestions during the course of this work. A special thanks is due to Dr. A. J. F. Metherell of the Cavendish Laboratory, Cambridge, England, for providing most of the design details of the energy analyzer.

This work was done under the auspices of the United States Atomic Energy Commission through the Inorganic Materials Research Division of the Lawrence Berkeley Laboratory.

REFERENCES

1. Kikuchi, S., Jap. J. Phys. 5, 83 (1928).
2. Boersch, H., Phys. Z. 38, 1000 (1937).
3. Pfister, H., Ann Phys., Lpz. 11, 239 (1953).
4. Uyeda, R., Y. Fukano and T. Ichinokawa, Acta. Cryst. 7, 217 (1954).
5. Thomas, G. and W. L. Bell, 4th European Regional Conference on Electron Microscopy, Proc., p283 (Rome, 1968).
6. Tan, T. Y., W. L. Bell and G. Thomas, Phil. Mag. 24, 417 (1971).
7. von Laue, M., Ann. Phys., Lpz. 23, 705 (1935).
8. Lamla, E., ibid, 32, 178 (1938); also: ibid. 33, 225 (1938).
9. Artman, K., Z. Phys. 124, 80 (1947); ibid. 124, 154 (1947); ibid. 125, 27 (1948); ibid. 125, 225 (1948); ibid. 125, 298 (1948); also: ibid. 126, 533 (1949).
10. Fuse, E., Ann. Phys., Lpz. 36, 209 (1939); also: Fuse, E. and H. Riedel, Ann. Phys., Lpz. 6, 105 (1949).
11. von Laue, M., Materiewellen und Ihre Interenzen, p335 (1948).
12. Kainuma, Y., Acta. Cryst. 8 247 (1955).
13. Cundy, S. L., A. J. F. Metherell, M. J. Whelan, P. T. Unwin and R. B. Nicholson, Proc. Roy. Soc. London, A307, 263 (1968).
14. Spalding, D. R., J. W. Edington and R. E. Villagrana, Phil. Mag. Ser. 8, 20, 1203 (1968).
15. Klemperer, O., Report on Progress on Physics 28, 77 (1965).
16. Watanabe, H., J. Electron Microscopy 4, 24 (1956).
17. Watanabe, H. and R. Uyeda, J. Phys. Soc. Japan 17, 569 (1962).
18. Castaing, R. and L. Henry, J. Microscopie 3, 133 (1964).

19. Tompsett, M. F., M. B. Heritage and C. W. B. Grigson, Nature, 215, 499 (1967).

20. Yoshioka, H., J. Phys. Sco. Japan 12, 618 (1957).

21. Pines, D. and D. Bohm, Phys. Rev. 85, 338 (1952); also: ibid. 92, 609 (1953).

22. Ferrell, R. A., Phys. Rev. 101, 554 (1956).

23. Kamiya, Y. and R. Uyeda, J. Phys. Soc. Japan 16, 1361 (1961).

24. Hall, C. R. and P. B. Hirsch, Proc. Roy. Soc. 286A, 158 (1965).

25. Hall, C.R., Phil. Mag. 12, 815 (1965).

26. Yoshioka, H. and Y. Kainumu, J. Phys. Soc. Japan 17, Supp. B11, 134 (1962).

27. Kainuma, Y. and H. Yoshioka, ibid. 21, 1352 (1966).

28. Fukahara, A., ibid. 18, 496, (1963).

29. Kainumu, Y., ibid. 20, 2263 (1965).

30. Takagi, S., ibid. 13, 278 (1958); also: ibid. 13, 287 (1958).

31. Fujimoto, F. and Y. Kainumu, ibid. 18, 1792 (1963).

32. Gjonnes, J., Acta. Cryst. 20, 240 (1966).

33. Cowley, J. M. and A. P. Pogany, ibid. A24, 109 (1968).

34. Doyle, P. A., ibid. A25, 569 (1969).

35. Hall, R. C., Phil. Mag. 22, 63 (1970).

36. Thomas, L. E. and C. J. Humphreys, Phys. Stat. Sol. A3, 599 (1970).

37. Nathan, R., Proc. 28th Annual Meeting, EMSA, 28 (1970).

38. Metherell, A. J. F. and M. J. Whelan, J. Appl. Phys. 37, 1737 (1966).

39. Metherell, A. J. F., Optik 25, 250 (1967).

40. Spalding, D. R. and A. J. F. Metherell, Phil. Mag. 18, 41 (1968).

41. Spalding, D. R., R. E. Villagrana and G. A. Chadwaick, Phil. Mag. 20 471 (1969).

42. Thomas, L. E. Proc. 29th Annual Meeting, EMSA, 174 (1971).

43. Honjo, K. and K. Mihama, J. Phys. Soc. Japan 9, 184, (1954).

44. Gjønnes, J., Acta Cryst. 15, 703 (1962).

45. Bloch, F., Z. phys. 52, 555 (1928).

46. Sturkey, L., Acta Cryst. 10, 858 (1957).

47. Fujimoto, F., J. Phys.Soc. Japan 14, 1558 (1959).

48. Niers, H., Z. Nature 14a, 504 (1959); also: Z. Phys. 156, 446 (1959).

49. Takagi, S., Acta. Cryst. 15, 1311 (1962).

50. Howie, A. and Z. S. Basinski, Phil. Mag., 17, 1039 (1968).

51. Howie, A. and M. J. Whelan, Proc. Roy. Soc. A263, 217 (1961).

LEGAL NOTICE

This report was prepared as an account of work sponsored by the United States Government. Neither the United States nor the United States Atomic Energy Commission, nor any of their employees, nor any of their contractors, subcontractors, or their employees, makes any warranty, express or implied, or assumes any legal liability or responsibility for the accuracy, completeness or usefulness of any information, apparatus, product or process disclosed, or represents that its use would not infringe privately owned rights.

TECHNICAL INFORMATION DIVISION
LAWRENCE BERKELEY LABORATORY
UNIVERSITY OF CALIFORNIA
BERKELEY, CALIFORNIA 94720